D-meson production by muons in the COMPASS experiment at CERN

Alexander Zvyagin

München, November 2010

D-meson production by muons in the COMPASS experiment at CERN

Alexander Zvyagin

Dissertation
an der Fakultät für Physik
der Ludwig–Maximilians–Universität
München

vorgelegt von
Alexander Zvyagin
aus Moskau, Russland

München, November 2010

Erstgutachter: Prof. Dr. Martin Faessler
Zweitgutachter: Prof. Dr. Dorothee Schaile
Tag der mündlichen Prüfung: 21 Januar 2011

Abstract

One of the physics goals of the COMPASS experiment at CERN was to measure the contribution of gluons to the nucleon spin. To achieve this, it was proposed to scatter polarized 160 GeV/c muons on a polarized deuteron target and to detect D mesons in the final state. The underlying process in this D meson production is supposed to be the Photon-Gluon Fusion (PGF), where a virtual photon emitted by the muon interacts with a gluon from the target nucleon, producing a charm-anticharm quark pair. Fragmentation of a charm (anticharm) quark leads with high probability to the creation of a D^0 or D^* meson, which COMPASS detects via the $D^0 \to K\pi$ and $D^* \to D^0\pi \to K\pi\pi$ decay modes. From the longitudinal cross section spin asymmetries of the D meson production and theoretical predictions for the PGF cross section, the gluon contribution to the nucleon spin has been measured by the COMPASS experiment.

The results presented in the thesis are the following. Based on data from the year 2004 a total visible cross section of 1.8 ± 0.4 nb, for the D^* meson production, has been measured, with the error being dominated by systematic effects. It is validated that the D mesons are indeed produced through the PGF process, by comparison of measured D meson kinematic distributions to the ones predicted by a theory (AROMA generator). A good agreement was found for the distribution shapes, which confirms that PGF plays a major role. However, a 20% difference was found in the number of produced D^0 and $\overline{D^0}$ mesons (and for the D^{*+} and D^{*-} mesons as well) which is significantly larger than predicted by AROMA. Kinematic distributions of D^0 and D^* mesons were compared with the background and also with the nearby $K_2^*(1430)^0$ resonance, using all longitudinal data taken in 2002-2006. The particle-antiparticle asymmetry has been studied as a function of several kinematic variables. The 20% excess of mesons decaying into $K^+\pi^-$ over mesons decaying into $K^-\pi^+$ was observed for all three mesons. The behavior of the $D^0/\overline{D^0}$ (and D^{*+}/D^{*-}) asymmetries as a function of virtual photon energy suggests that associated production of $D^{*-}\Lambda_c^+$ or $\overline{D^0}\Lambda_c^+$ may be responsible for the observed effect.

The longitudinal double spin asymmetries have been studied for the D^0, D^* and $K_2^*(1430)^0$ mesons separately for particle, antiparticle and for the sum of particle and antiparticle. It was found that the asymmetries extracted for D^0 and D^* mesons are compatible with zero. A 3-sigma deviation from zero asymmetry was observed for the $K_2^*(1430)^0$ meson. An investigation of the $K_2^*(1430)^0$ double spin asymmetry reveals a dependence as function of the Bjorken x_{Bj} variable.

Zusammenfassung

Eines der Ziele des COMPASS-Experimentes am CERN war, den Beitrag der Gluonen zum Spin des Nukeons zu bestimmen. Der vorgeschlagene Weg war, polarisierte Myonen mit Impulsen von 160 GeV/c auf ein polarisiertes Deuteron-Target zu schießen, um D-Mesonen zu erzeugen. Die theoretische Annahme ist, dass die Photon-Gluon-Fusion der wichtigste zugrundeliegende Prozess ist, der zur D-Meson- Produktion führt. Das virtuelle, vom Myon emittierte Photon wechselwirkt mit einem Gluon im Nukleon und dabei wird ein Charm-Anticharm-Quarkpaar erzeugt. Charm- (oder Anticharm-) Quark fragmentieren mit großer Wahrscheinlichkeit in ein D^0 - oder D^{*+} - Meson (bzw $\overline{D^0}$ oder D^{*-}). COMPASS weist diese Mesonen nach über die Zerfälle $D^0 \to K\pi$ und $D^* \to D^0\pi \to K\pi\pi$. Aus der gemessenen Asymmetrie der D-Meson-Produktions-Wirkungsquerschnitte von longitudinal parallel oder antiparallel polarisierten Myonen und Deuteronen und theoretischen Vorhersagen für die entsprechende Asymmetrie des Photon-Gluon-Fusionsprozesses wurde der Beitrag des Gluons zum Nukeonspin gemessen.

Folgende Resultate werden in der vorliegenden Arbeit gezeigt: Auf der Basis der im Jahr 2004 aufgenommenen Daten wurde ein Gesamtwirkungsquerschnitt von $1.8 \pm 0.4\, nb$ für die D^*-Meson-Produktion, innerhalb der COMPASS-Akzeptanz (D^*-Meson-Energien von 22 bis 86 GeV) gemessen. Der Messfehler wird dominiert von systematischen Effekten. Es wurde nachgewiesen, dass die D-Meson-Produktion in ihren wesentlichen Eigenschaften übereinstimmt mit den Erwartungen auf der Basis der Photon-Gluon-Fusion. Die detaillierten Rechnungen werden im verwendeten AROMA- Ereignisgenerator durchgeführt. Eine gute Übereinstimmung wurde mit der Form der theoretischen Verteilungen gefunden. Dies unterstützt die Annahme, dass die Photon- Gluon- Fusion in der Tat eine dominante Rolle spielt. Der gemessene Unterschied von 20% in der Zahl sowohl der D^0- und $\overline{D^0}$- Mesonen als auch der D^{*+} - und D^{*-} -Mesonen ist allerdings signifikant größer als von AROMA vorhergesagt. Die kinematischen Verteilungen der D^0 - und D^* - Mesonen wurden auch verglichen mit denen des Untergrundes und der benachbarten $K_2^*(1430)^0$ - Resonanz unter Verwendung aller longitudinaler Daten aus den Jahren 2002-2006. Auch die Teilchen-Antiteilchen- Asymmetrie wurde studiert als Funktion dieser Variablen. Der Überschuss von 20% der $K^+\pi^-$ - relativ zur $K^-\pi^+$ -Kombination wurde für alle 3 Mesonen beobachtet. Das Verhalten der $D^0/\overline{D^0}$ - (und D^{*+}/D^{*-} -) Asymmetrien als Funktion der Energy des virtuellen (Austausch-) Photons legt nahe, dass dieser Unterschied von der assoziierten Produktion von $\overline{D^0}$ bzw D^{*-} mit einem Charm- Baryon Λ_c^+ verursacht wird.

Die longitudinalen (Doppel-) Spinasymmetrien wurden untersucht für D^0 -, D^* - und $K_2^*(1430)^0$ -Mesonen getrennt für die Mesonen und Antimesonen und für beide zusammen. Es wurde gefunden, dass alle Asymmetrien verträglich sind mit 0, innerhalb der statistischen Fehler, außer in einem Fall: Für das $K_2^*(1430)^0$ -Meson wurde eine 3-Sigma-Abweichung von 0 beobachtet. Die Daten legen eine Abhängigkeit dieser (Doppelspin-) Asymmetrie von Bjorken x_{Bj} nahe.

Contents

Chapter 1

Introduction

The COmmon Muon and Proton Apparatus for Structure and Spectroscopy (COMPASS) experiment at the European Organization for Nuclear Research (CERN) was build to investigate the structure of nucleons and mesons. By scattering of 160 GeV polarized muons on a polarized deuteron target the COMPASS *muon program* touches various questions of the nucleon structure. Among the problems where the COMPASS experiment may contribute with some answers, the question of the nucleon spin composition is of a special importance. Since the nucleon is not a pointlike particle, the nucleon spin must be formed by its constituents - the quarks and the gluons. The COMPASS predecessor experiments (like European Muon Collaboration (EMC)) have shown that the quark spins contribute only little ($\approx$ 25%, see [1]) to the proton spin. The contribution of gluon spin or/and orbital momentum between quarks and gluons is expected to compensate the missing part. This schematically can be represented by the formula for the proton spin projection [1]:

$$\frac{1}{2}\hbar = \left(\frac{1}{2}\cdot\Delta\Sigma + \Delta G + L_z\right)\hbar \tag{1.1}$$

where $\Delta\Sigma$ is the contribution of quarks, ΔG that of the gluons and L_z symbolizes contributions from orbital angular momenta of quarks and/or gluons. By using the longitudinally polarized target (parallel or antiparallel to the beam polarization) the COMPASS experiment has measured the gluon contribution ΔG to the nucleon spin, [2].

The parton polarization depends on its momentum. It is relatively well known in the longitudinal case, when spin projection and momentum axes for a parton coincide, see [3]. For the transverse case, our present knowledge is much worse. To learn more about it, COMPASS uses transversely polarized target and measures the Sivers, Collins, two-hadron asymmetries and studies the Λ polarization, see [4].

With a beam of positive or negative pions the *hadron program* of the COMPASS experiment has a big potential in hadron spectroscopy. A search for gluball and hybrid states is a challenging experimental task in high energy physics since decades. Not being forbidden by the theory, the gluballs and hybrids were not yet found with enough confidence.

[1] The proton spin projection to an axis is $\pm 1/2\hbar$, the positive value is taken for the equation.

The pion and kaon polarizabilities studied with the Primakoff reaction are also part of the COMPASS *hadron program*.

The thesis is about the *open charm muoproduction*, which is a a part of *muon program* of the COMPASS experiment, so the main emphasis is put on this program.

Open charm production in inelastic scattering of 160 GeV muons (or electrons) from nucleons is assumed to be dominated by a process where the exchanged virtual photon fuses with a gluon into a charm-anticharm quark pair $\gamma g \to c\bar{c}$, see Figure 3.1. The cross section of the PGF process and its dependence on the relative polarisation of photon and gluon can be calculated in perturbative Cuantum ChromoDynamics (QCD) [5, 6, 7, 8, 9, 10, 11, 12].

Thus, using polarized muons and nucleons, a measurement of the cross section asymmetry $\Delta\sigma^{\mu N\to c\bar{c}}/\sigma^{\mu N\to c\bar{c}}$ allows to determine the gluon polarisation $\Delta G/G$ in the nucleon. With this goal, open charm production has been studied in the COMPASS experiment at CERN for longitudinally polarized muons interacting with longitudinally polarized deuterons. The muon beam energy of 160 GeV has been chosen, since the cross section difference $\Delta\sigma^{\gamma N\to c\bar{c}}$ for parallel and antiparallel spins of photon and nucleon reaches a maximum for photon energies around 80 GeV according to most models, and the polarization transfer (depolarization factor) is large in the relevant photon range.

Final states where the decay $D^0 \to K^-\pi^+$ or the charge conjugate (c.c.) decay is detected or events, where an additional pion and the decay chain $D^{*+} \to D^0\pi^+ \to K^-\pi^+\pi+$ or c.c. is observed, have been chosen in order to achieve the best possible combination of mass resolution, signal over background ratio and signal statistics. Based on event samples with these final states extracted from data taken during the years 2002-2006, COMPASS has published results for $\Delta G/G$ from open charm muoproduction [2].

The relevant muon - gluon cross section asymmetry a_{LL} for extracting $\Delta G/G$ has been estimated for each event, assuming only PGF contributes as calculated in leading order QCD and assuming charm and anticharm quarks fragment (almost) independently. The parton kinematics are estimated on the basis of the observed 3- momentum of the D^0 meson and the momentum difference of the incoming and outgoing muon, event by event.

Yet, other production mechanisms than PGF with independent charm quark fragmentation may contribute to the observed events with charmed mesons. The interaction of the virtual photon with intrinsic charm is one possible competing mechanism [13, 14, 15]. The associated production of $\Lambda_c + \overline{D^0}$ [16] or, more generally, an asymmetric fragmentation of D^0 and $\overline{D^0}$ like in the Dual Parton model with a meson and a baryon string [17, 18] may play an important role in some regions of phase space. A study of the phase space distributions of the D^0 and $D^{*\pm}$ mesons within the acceptance of the COMPASS spectrometer may provide a clue to which production mechanisms contribute.

At the Hadron-Electron Ring Accelerator (HERA), i.e. much larger c.m. energy, the charm electroproduction has been studied in detail by the H1 collaboration (H1) and ZEUS collaboration (ZEUS), see references [19, 20, 21] and references therein. At these energies, other production mechanisms contribute, like gluon-gluon fusion to $c\bar{c}$ from a resolved photon, and the fragmentations of c and $\bar{c}$ can more safely be assumed to be independent than at COMPASS, which covers the range from threshold up to 140 GeV photon energies in the laboratory. Prior to COMPASS, this energy region range has been covered only by

one experiment, EMC [22], which collected about 90 D^0 meson events produced by deep inelastic scattering of 240 and 280 GeV muons on hydrogen and deuterium targets for a study of the production mechanism.

The section 4.1 of the present thesis shows details of the phase space distributions of open charm production. The chosen kinematical variables are the squared transverse momentum p_T^2, energy E_D, and energy fraction z_D, of the produced neutral D mesons, and the inclusive muon variables ν, Q^2 and x_{Bj}. The distribution of signal events are compared to those of background events, and theoretical predictions for the production of D mesons by PGF and NLO processes. The large number of events allows a comparison of the distributions of D^0 and $\overline{D^0}$ mesons and to investigate, in particular, the dependence of the semi-inclusive differential cross section on the photon energy E_γ from threshold (around 30 GeV) up to 140 GeV.

Scattering a polarized beam off a polarized target, the cross section (double) spin asymmetries can be studied as a function of different kinematic variables. In terms of observed variables, the asymmetry of PGF is (theoretically) expected to depend on energy E and transverse momentum p_T of the detected D mesons. If D-mesons would be produced through the absorption of the virtual photon by a charm quark (intrinsic in the nucleon), than the cross section spin asymmetry would be expected to depend on the x_{Bj} variable. Therefore, traditionally in Deep Inelastic Scattering (DIS) experiments these asymmetries are measured for identified mesons $\pi^\pm$ and $K^\pm$, because they are assumed to be produced by the leading order process (absorption of the virtual photon by one of the constituent quarks of the nucleon which than fragmens to the meson). COMPASS has published results on asymmetries measured for the identified mesons $\pi^\pm$ and $K^\pm$, see [23]. The thesis shows the cross section double spin asymmetries calculated for the D^*, D^0 and $K_2^*(1430)^0$ mesons as a function of x_{bj} and (E, p_T) of the corresponding meson.

Chapter 2

The COMPASS experiment

2.1 Apparatus Overview

The COMPASS spectrometer should detect both the incoming and scattered muon before and after its interaction in the target. In addition, other particles (with momenta up to the beam momentum of 160 GeV/c) produced from the interaction in the target also need to be reconstructed. The spectrometer acceptance should cover the angular range of ± 250 $mrad$. To achieve this COMPASS uses two magnets and tracking detectors covering small (small angular spectrometer (SAS)) and large angles (large angular spectrometer (LAS)). The COMPASS spectrometer also has calorimeters, a Ring Imaging CHerenkov light (RICH) detector and hodoscopes.

The present section of the thesis briefly explains the COMPASS spectrometer components relevant for physics with a muon beam. The COMPASS experiment setup is shown in Figure 2.1. The article [24] contains a detailed spectrometer description.

Figure 2.1: The COMPASS spectrometer in 2004. The detector names are explained in the text and the glossary.

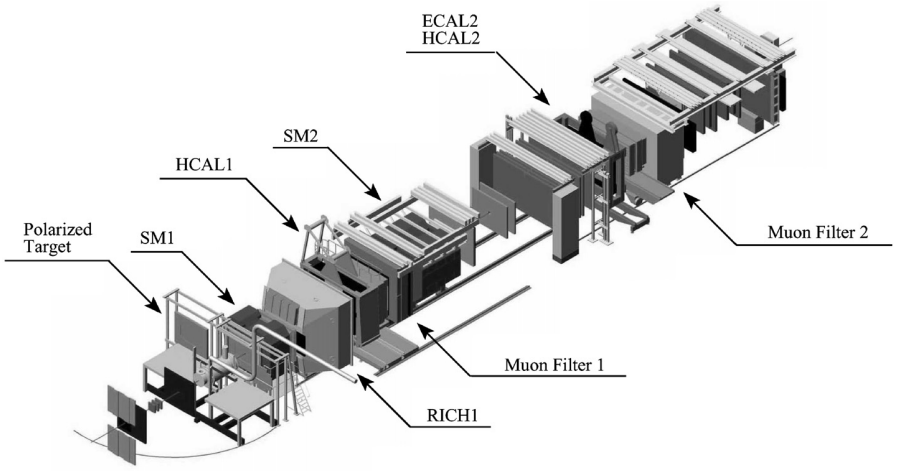

(a) 3D view of the COMPASS spectrometer. The size of the spectrometer is about $4 \times 4 \times 50$ meters.

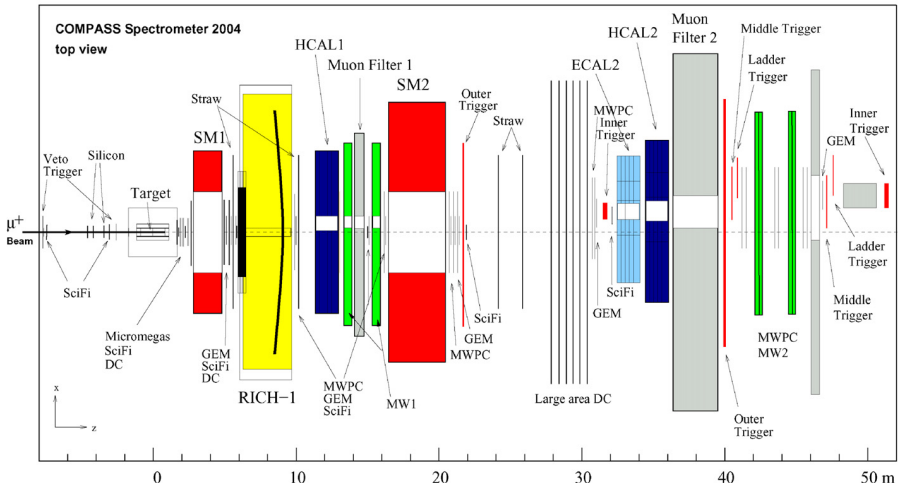

(b) Schematic view of the COMPASS spectrometer.

2.1.1 Beam Line

Protons with 400 GeV/c momentum and an intensity of $1.1 \cdot 10^{13}$ protons per spill (the typical spill length may vary from 5 to 40 seconds) are provided by the Super Proton Synchrotron (SPS) accelerator at CERN. The beam of protons hits a primary target (made from Beryllium, 500 mm in length) and produces different particles with various momenta. The beam line with magnetic optics of dipole and quadrupole magnets selects positive or negative particles with momenta around 180 GeV/c. These particles are mainly pions with a few percent of kaons as well. The approximate intensity of this hadron beam is about $3.5 \cdot 10^{10}$ particles per spill.

In a 600 m long decay channel about 5% of pions and kaons weakly decay to muons and muon neutrinos: $\pi^+, K^+ \to \mu^+\nu_\mu$ or for a negative beam $\pi^-, K^- \to \mu^-\bar{\nu_\mu}$ (see Appendix A). Because neutrinos are always lefthanded (negative helicity) the muon's helicity is also fixed (in the π, K rest frame). Going from a π, K center of mass system to the laboratory system, the polar angle of $\mu^\pm$ will affect the polarization of muons in the laboratory system, decreasing it from 100% to a value which depends on the muon momentum. At momenta ≈ 160 GeV/c a polarization of $-75 \pm 4\%$ is reached, see Figure 2.2. The intensity of the muon beam is $2 \cdot 10^8$ muons per spill. By using absorbers in the beam tunnel the hadrons present in the beam can be removed (and this is done to get the muon beam), and only muons reach the COMPASS polarized target. For the hadron program of COMPASS absorbers are not used, and the beam of hadrons (mainly pions) which have not decayed will reach the COMPASS spectrometer.

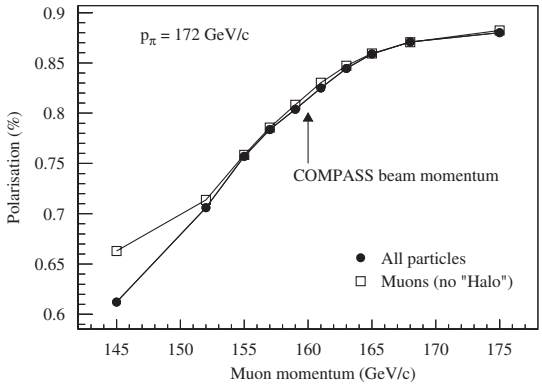

Figure 2.2: Muon beam polarization (absolute value) as a function of beam momentum.

2.1.2 Polarized Target

The muon program of COMPASS requires a polarized target. For the target material, ^6LiD has been chosen, because it has a large fraction of polarizable nucleons (≈ 0.4) and high polarization ($\approx 50\%$).

The COMPASS experiment used 2 target cells of equal length and opposite polarisation during the years 2002-2004, see [25]. In the year 2006 the 2-cell polarized target was changed to a new 3-cell target. The outer two cells, having together equal length as the single inner target cell, had the same polarisation, opposite to that of the inner cell.

The COMPASS target polarization system allows to reach 30% of polarization in one day and it takes about 5 days to go to the maximum polarization of 50%, see Figure 2.4. To maintain the polarization a superconducting solenoid magnet of homogeneous magnetic

Figure 2.3: Schematic view of the COMPASS polarized target in 2004: (1),(2) upstream and downstream target cells. (3) microwave cavity, (4) target holder, (5) still (^3He evaporator), (6) ^4He evaporator, (7) ^4He liquid/gas phase separator, (8) ^3He pumping port, (9) solenoid coil, (10) correction coils, (11) end compensation coil, (12) dipole coil. The muon beam enters the target from the left.

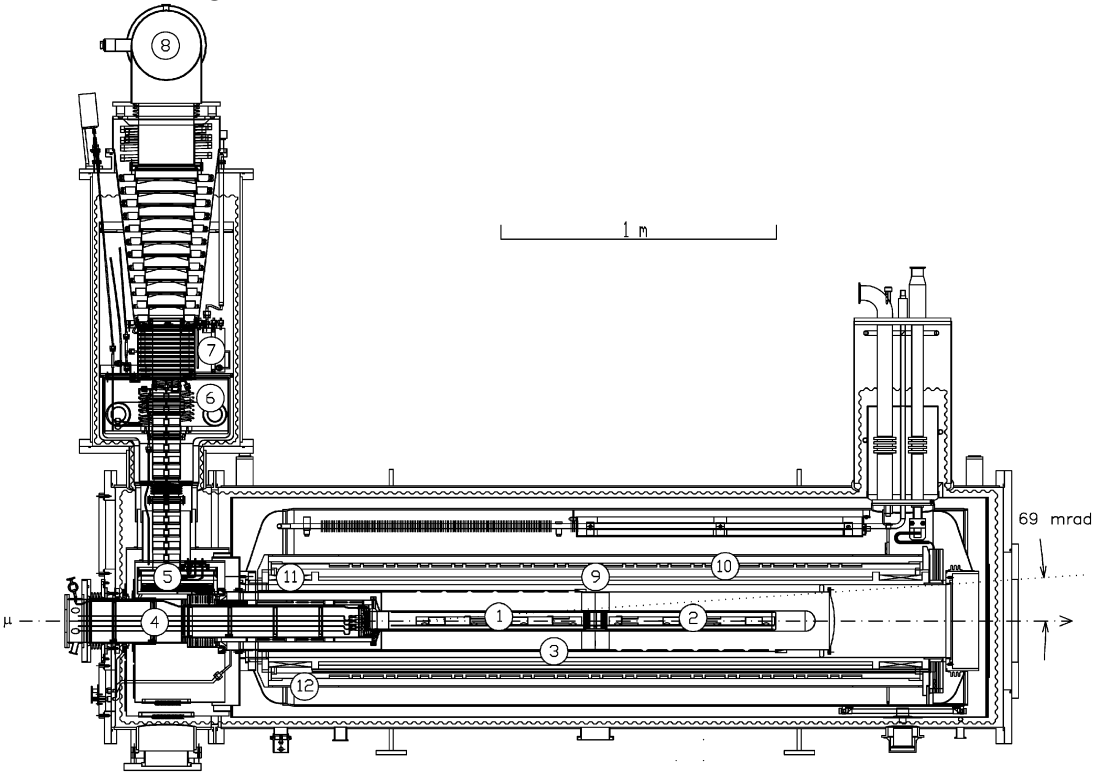

Figure 2.4: Polarization of upstream (crosses) and downstream (circles) target cells during the run in 2003. The maximum polarization was +57% and −51% for the upstream cell and +54% and −49% for the downstream cell, see [25].

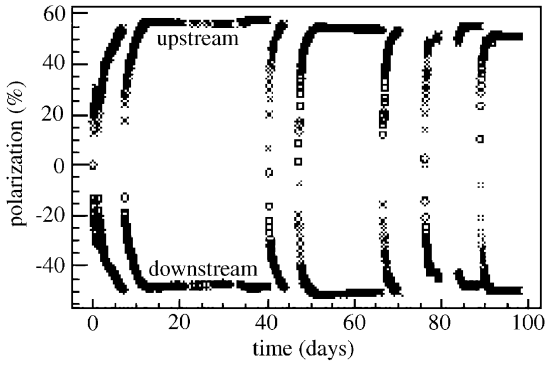

field of 2.5 T is used. Having a temperature of ≈ 0.1 K the target nucleon spin relaxation time is greater than 1000 h. With this temperature and this magnetic field the ^6LiD electrons have polarization of 96 %, while the nucleons < 1 %. By applying a microwave irradiation of a suitable freqency the electron polarization is transfered to the nucleons. This is the way how the target polarization is build up.

With the help of a dipole magnet integrated to the target, the cells polarization can be rotated without being destroyed. It takes about 40 minutes to rotate the target cell polarization by 180^o.

2.1.3 Charged Particle Tracking

The COMPASS spectrometer is equipped with different types of tracking detectors. They vary in size (from 25 cm^2 for Scintillating Fibre Detector (SciFi) to 10 m^2 for Drift Chambers (DCs) and Straw Drift Chambers (SDCs)), space resolution (from 10 μm for silicon detectors to 1.6 mm for Multiwire Proportional Chambers (MWPCs)) and time resolution (from 0.3 ns for Beam momentum station (BMS) to 10 ns for Gas Electron Multipliers (GEMs) and Micromega Detectors (MMs)).

To reconstruct tracks with momenta in the range from a few to 160 GeV/c the COMPASS spectrometer uses two magnets. The first magnet SM1 (part of LAS) with a magnetic field integral of 1.0 $T \cdot m$ bends low energetic charged tracks (a 1 GeV/c particle would be bent by 300 $mrad$), while the second SM2 (part of SAS, the field integral is 4.4 $T \cdot m$) affects high momentum charged tracks. The tracking detectors are installed before and after the SM1 and SM2 magnets to measure the bending angle of charged tracks, which allows to reconstruct the charged track momentum by the COMPASS reconstruction program, see section 2.3.

The incoming muon beam track momentum is measured mainly by silicon detectors and the BMS. Several detectors of the BMS are located in the beam line (see subsection 2.1.1) and use the beam line magnetic optics.

2.1.4 Calorimetry

The COMPASS spectrometer uses two hadron calorimeters HCAL1, HCAL2 and two electromagnetic calorimeters ECAL1, ECAL2. The ECAL1 [1] and HCAL1 are placed behind tracking detectors installed after the SM1 magnet and just before tracking detectors in front of the SM2 magnet. The physical hole made at the center of calorimeters allows for beam and high momenta particles (which are bent by SM1 magnet only slightly) to reach the second part of the spectrometer. Here the SM2 magnet is placed (together with tracking stations in front and behind it) and downstream of it the calorimeters ECAL2 and HCAL2 are installed (again with a physical hole in the center).

Information from calorimeters is not used directly in the analysis presented in the section 4.1. But being a part of the COMPASS trigger system (see section 2.2) the HCAL2

[1] The ECAL1 calorimeter was not installed in 2004 data, that is why it is not shown on the Figure 2.1.

is used indirectly.

2.1.5 Particle Identification Detectors

RICH Detector

Particle identification (mainly for pions and kaons) is performed by a Ring Imaging CHerenkov light (RICH) detector. The detector is located after the SM1 magnet (part of LAS) and covers the angular acceptance of ± 250 *mrad*.

Muon Wall Detector

The scattered muon identification (muon filter) is performed with the help of two Muon Wall (MW) detectors. A MW detector consists of two tracking planes separated by an absorber (60 *cm* iron). Muons passing through the MW detector would be detected before and after the absorber, while other tracks (hadrons,gammas) most probably will be stopped by it, if they have not already been stopped by the calorimeters.

2.2 The Trigger System

Figure 2.5: Main elements of the trigger system (top view): hodoscopes H3,H4,H5 and calorimeter HCAL2. Muon walls (μ Filter) are used as hadron aborbers, they improve the trigger purity. The magnetic field of SM1 and SM2 deflects positive muons in the horizontal direction (from bottom to top on the scheme). The hodoscopes are installed to suppress the beam halo, they are indicated as *vetos*.

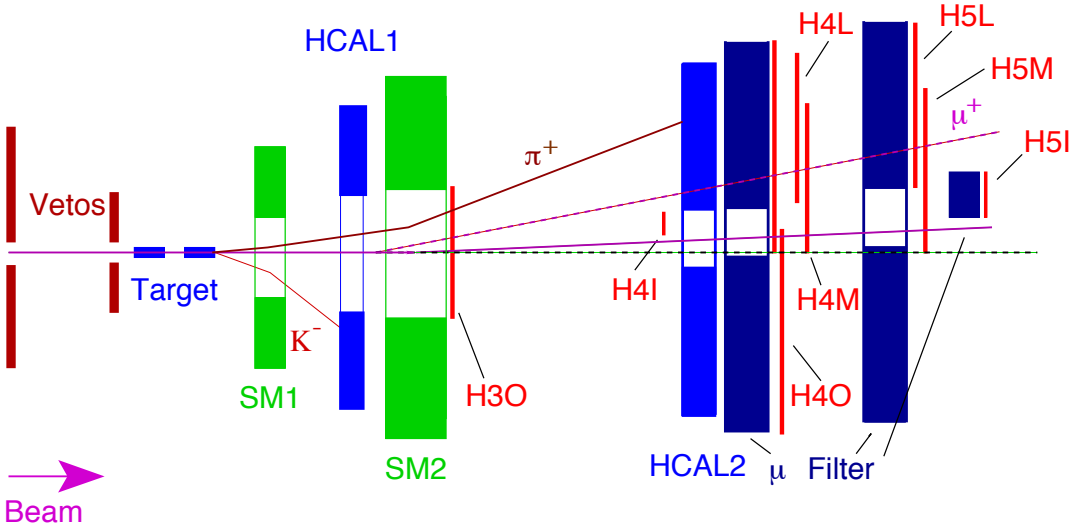

The physics program with muon beam requires that the kinematical acceptance of the

COMPASS spectrometer covers a wide range of Q^2 values - starting from quasi-real photons with $Q^2 \approx 0$ and reaching the muon beam energy of 160 GeV.

To achieve this the COMPASS trigger system uses several techniques based on horizontal/vertical muon scattering angles θ_x/θ_y and energy deposit in calorimeter(s). The COMPASS magnets SM1 and SM2 deflect charged particles in the horizontal direction, so horizontal $x-z$ is a *bending* and vertical $y-z$ is a *non-bending* plane. A set of hodoscopes is used in the trigger system. The hodoscopes with vertical and horizontal strips are located both before and after different absorbers (like calorimeters and MW detector) and calorimeter HCAL2. The COMPASS trigger system used in 2004 year is detailed in [26].

Vertical Target Pointing

For large Q^2, the muon scattering angle is large enough to be detected directly by hodoscopes. By using two hodoscopes with horizontal strips located at different z positions along the beam, the vertical component θ_y of the scattered muon angle can be measured. The event is triggered if θ_y is compatible with the target position.

Energy Loss

For quasi-real ($Q^2 \approx 0$) photons, the scattering angle θ_y is too small. But the muon energy loss ν is translated into a deflection by the magnetic dipole field. The trigger system is sensitive to values $\nu > 45$ GeV.

Triggering on Calorimetry

Even without observing a scattered muon but by just seeing (a) large energy deposit(s) in calorimeter(s) one can conclude that an inelastic interaction has happened and it is worth to record such an event. In addition to the scattered muon, the calorimeter information can be used to improve the trigger purity.

A combination of *vertical target pointing, energy loss, triggering on calorimetry* techniques leads to several different triggers which were used in the COMPASS experiment with the muon beam, see Table 2.1. The *inner*, *ladder* and *middle* triggers are based on energy loss measurements. The *inclusive middle* and *outer* triggers check the vertical target pointing. The *middle* trigger is formed from the inclusive middle trigger and some energy deposit in the calorimeter. Finally, the *calorimeter* trigger uses only HCAL2 information, without any knowledge on the scattered muon.

All these triggers are described in the Monte Carlo (MC) simulation of the COMPASS spectrometer. The data distributions and acceptances for different triggers are presented in the Appendix D, Figure D.3-Figure D.8.

Table 2.1: COMPASS triggers with the muon beam in 2004. The location of COMPASS trigger components is shown in Figure 2.5.

trigger name	technique	components
inner	energy loss	H4I,H5I
ladder	energy loss	H4L,H5L
inclusive middle	energy loss, target pointing	H4M, H5M
middle	energy loss, target pointing, calorimeter	H4M, H5M, HCAL2
outer	target pointing	H3O, H4O
calorimeter	calorimeter	HCAL2

2.3 Reconstruction Program

The COMPASS reconstruction program is named CORAL. Having many different tracking detectors, several calorimeters and hodoscopes the COMPASS experiment needs powerful algorithms for event reconstruction. By using raw event (or MC event) information, detector calibration constants, detector alignment information CORAL is able to:

- reconstruct the incoming beam track momentum;
- reconstruct tracks of charged particles through the fields of SM1 and SM2 magnets;
- perform particle identification of the charged tracks passing through the RICH detector;
- find track vertices (both primary and secondary);
- reconstruct the energy of particles hitting the calorimeters.

The present analysis relies mostly on the track reconstruction and particle identification of pions and kaons performed by the RICH detector. As it was mentioned earlier, the COMPASS spectrometer has one RICH detector for particle identifcation. For every track (for which momentum and hit position in RICH was reconstructed by tracking detectors) which passes the RICH volume, one can predict the ring radius

Figure 2.6: The two-dimensional distribution of Cherenkov angle versus particle momentum demonstrates the quality of the particle identification with the RICH detector. The pion band is suppressed by a factor 3 and the proton band is enhanced by a factor 4.

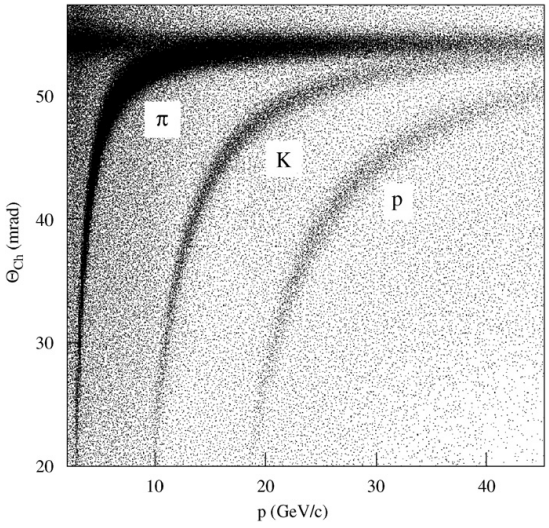

of Cherenkov photons corresponding to particles
with different masses or rather velocities.

For a particle $i = e, \pi, K, p$ (electron,pion,kaon,proton) the number of photons found at the radius r_i is compared to the expected number of Cherenkov photons for a particle i. This number depends on such parameters as hit position in RICH, ring radius r_i, RICH gas refraction index. Based on this comparision the likelihoods $LK(i)$ of the hypothesis that the track is coming from a particle $i = e, \pi, K, p$ are assigned to every reconstructed track . In addition, a background ($i = bkg$) hypothesis is calculated as well. The effective identification range of the RICH detector is $2.9 - 50\ GeV$ for pions and $8.9 - 50\ GeV$ for kaons, see Figure 2.6.

2.4 Straw Drift Chambers

The large area Straw Drift Chamber (SDC) detectors with in total ≈ 12000 channels play an important role in charged track reconstruction of the COMPASS spectrometer. The author worked on the installation of the SDC detectors in the COMPASS spectrometer, on the maintenance of the detector during data taking periods and on the detector calibration.

The present section of the thesis explains the time calibration procedure of SDC detector. This work has been done in collaboration with Jean-Francois Rajotte.

2.4.1 Structure

Figure 2.7: A schematic view of a Straw Drift Chamber detector of X-type.

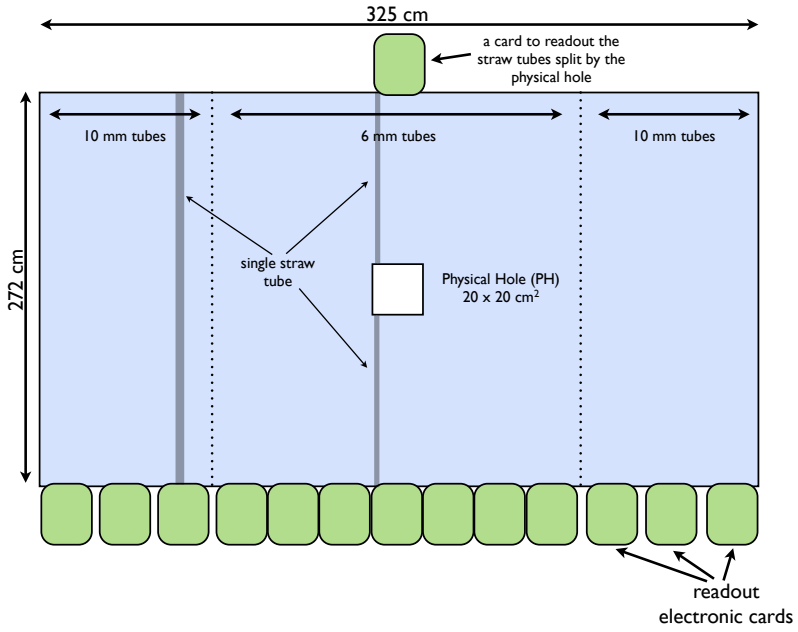

Design, construction and basic properties of SDC detector are explained in the articles [27, 28]. The present section of the thesis only explains the detector structure components relevant to its time calibration procedure.

A sketch of the SDC detector is shown in Figure 2.7 and Figure 2.8. A single SDC detector consists of two layers of tubes (one detector is often called *double layer (DL)*) glued together and connected to an aluminium frame. There are two types of frames: X-type with vertical location of tubes (to measure the horizontal (X) coordinate of tracks) and Y-type with horizontally placed tubes (to measure the vertical (Y) coordinate of tracks). The incoming beam is directed to the detector center, and would cause a very high event rate from the detector central region. To avoid this, the region should be either inactivated or contain no material at all. For the SDC it was decided to have a physical hole (PH) in the detector center, see Figure 2.7.

To stand the high particle rates at the region close to the beam, the inner part of detector is made from 6 *mm* tubes, while the outer one is build up from 10 *mm* tubes. The signal amplifiers are integrated into the frame and the readout cards, to digitize and send data to the Data Acquisition (DAQ) system, are attached to the frame. The signal readout is done on one side of the tubes, for the X-chambers at the bottom side. Because the tubes at the detector center are split by the PH, a special readout card is needed for the tubes on the top of the PH. The readout of Y-chambers is done similar, with the exception that the cards are located on the left and right sides.

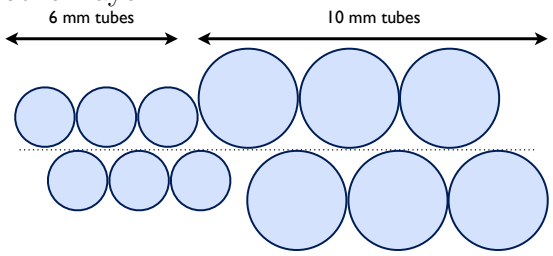

Figure 2.8: The double layer structure of the detector. One layer of tube is shifted by the tubes radius with respect to another layer.

Naming convention

A single SDC detector (DL) is described by 6 *subsections*: 2 layers of upstream and downstream straws (Figure 2.8) times three regions of straw tubes (central part with 6 *mm* straws and two outer parts with 10 *mm* straws, see Figure 2.7).

Having this complicated inner structure, a special naming convention was introduced to refer to different *subsections* of a single SDC. A typical subsection name is **ST05X1db**. The first two letters always are **ST** - they indicate that this is an SDC detector. The next number **05** is an SDC station number along the Z (beam) direction. The subsequent letter **X** indicates the orientation of the tubes in the XY plane of the DL. There are four possible orientations: Y (tubes are horizontal), X (tubes are vertical), and U,V (tubes are rotated $\pm 10^o$ with respect to the X orientation). After the projection letter the number **1** shows the number of DL with the same tube orientation in a given station. This number is usually 1, and in a few cases it goes to 2. The letter **d** identifies one of the two layers - it stands for an **u**pstream or a **d**ownstream layer. The very last letter **b** says that the section consists of 6 *mm* straw tubes. For the 10 *mm* straw tubes the letter would have been **a** or **c**.

Three *DLs* with projections X,Y and U or V form a *submodule*. In 2004, the COMPASS spectrometer used two ST03 submodules (combined in one module) and three submodules ST04,ST05,ST06. So in total there were five submodules. Every submodule consists of three detectors (double layers): one Y-type and two X-types. To read out a Y-type detector 11 cards and for a X-type detector 14 cards are needed. So in total, to read out all SDC detectors $195 = 5 \times (11 + 2 \times 14)$ cards are required.

2.4.2 Time Calibration

Motivation

A single straw drift tube measures time. Later (in the CORAL reconstruction program) this time is converted into a drift time by subtracting the drift start time T_0 for this straw. Then with the help of RT-relation relations that drift time is converted into drift distance. Finally hits in 3D space are created which are used by the track reconstruction algorithm. The drift start time T_0 depends on many parameters, such as cable lengths, the way wiring is done, etc. In principle every single channel (straw) has its own T_0 value. If a wrong T_0' value is applied for a channel, it will lead to a shift of a predicted hit coordinate by

$$\Delta h \approx \pm v \times (T_0' - T_0),$$

where Δh is the shift in the hit position, v is the drift velocity and $\pm$ indicates the left-right ambiguity (it is not known on which side of the wire the track crossed the straw).

With the drift velocity of $v \approx 60\ \mu m/ns$ and a desired spatial resolution $\sigma = 300\ \mu m$[2] T_0 should be measured with a precision not worse than $\sigma/v = \frac{300\mu m}{60\mu m/ns} = 5\ ns$.

A single card of SDC detector can read out up to 64 channels in total. **It is assumed that all 64 channels of the same card should have nearly identical T_0 values**. Every card has its own cable which connects it to the COMPASS DAQ system, and all 64 channels share the same cable. [3]. The cable lengths for different cards are not necessarily equal. And in principle, every card may have a T_0 which differs from the others and in total all cards may have different T_0 values. In this section the method and results of a T_0 calibration per card are described.

Analysis and calibration procedure

With the necessity of using individual T_0 for every card, the procedure of T_0 determination should be established. In short, one needs to find the smallest time measurement recorded for a physical track associated with an acceptable event. Figure 2.9 shows the time distribution for the hits recorded by one card. The SDC gives only the time of the hit relative to the experiment trigger time, the only independant information available. If a hit has an associated track, which is assumed throughout this section, the track hit position can be predicted, with a precision determined by the properties of the associated track, in the detector plane. Then, using alignment, the distance from the wire can be determined. The plot of *hit time* versus *track distance to the fired straw wire* is very informative about the drift detector properties. It is called **V-plot** and is shown in Figure 2.10.

From a V-plot one can obtain parameters which are very important for track reconstruction: T_0, the smallest possible drift time; RT-relation; detector resolution estimation (to be discussed later).

[2] This value is close to the optimal resolution which can be achieved for the chosen track parameters

[3] Signal digitization is done on the frontend cards, so cable length can not affect it. But the clock synchronization signal is sent via cables, so clocks of frontend cards may have different shifts. And this can be a cause of T_0 dependency versus card.

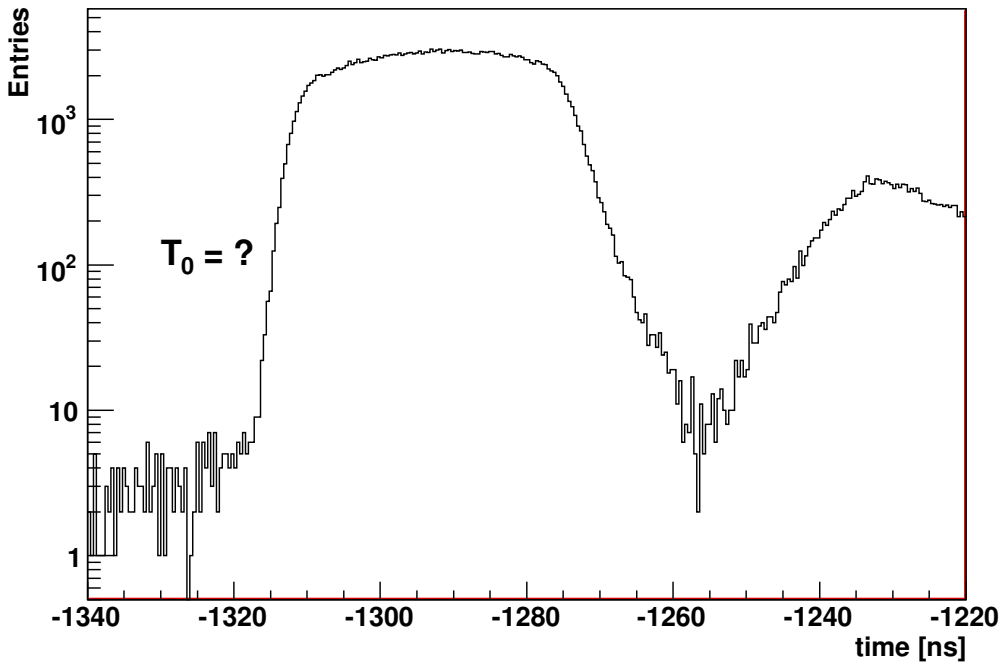

Figure 2.9: Typical time distribution of the hits recorded by one card

The question is : how precise T_0 can be determined? The answer depends on the quality of the data. Figure 2.11 shows a problematic case of detector data when two sets of V-plots with different T_0 values are present. If the data from Figure 2.11(a) are used (i.e from all the detector) to determine the T_0, some hits will be given a T_0 about $10ns$ too early. With a drift time of about 60 $\mu m/ns$, such an offset corrupts the hits to a point that they become useless. There were few cases[4] where the T_0 from a card deviates by even more than $10ns$ from its given T_0. This offset alone is a sufficient justification to implement the time calibration for every card.

To determine the T_0 from a data sample, the dependence of a track hit position and the corresponding detector drift time is used. The function which connects drift distances and drift time is known as the RT-relation. This function can be fitted on the V-plot in order to get the T_0 as in Figure 2.10. Once the T_0 is found, the distance between the "real" (extrapolated from the associated track) and the "predicted" hit position (obtained from the RT-relation) can be calculated. This value is called the **residual** and an example (somewhat extreme) is shown in Figure 2.10. A precise (thin) V-plot and a good RT-relation lead to a small residual.

The drift time t is converted into a drift distance d. If the fired straw coordinate is w (position of the wire) then the *predicted* hit coordinate is $w \pm d$. The $\pm$ sign indicates the left-right ambiguity: it is not known on which side from the wire the track crossed the

[4] Six cases to be precise, they will be detailed later, when the T_0 determination will be explained.

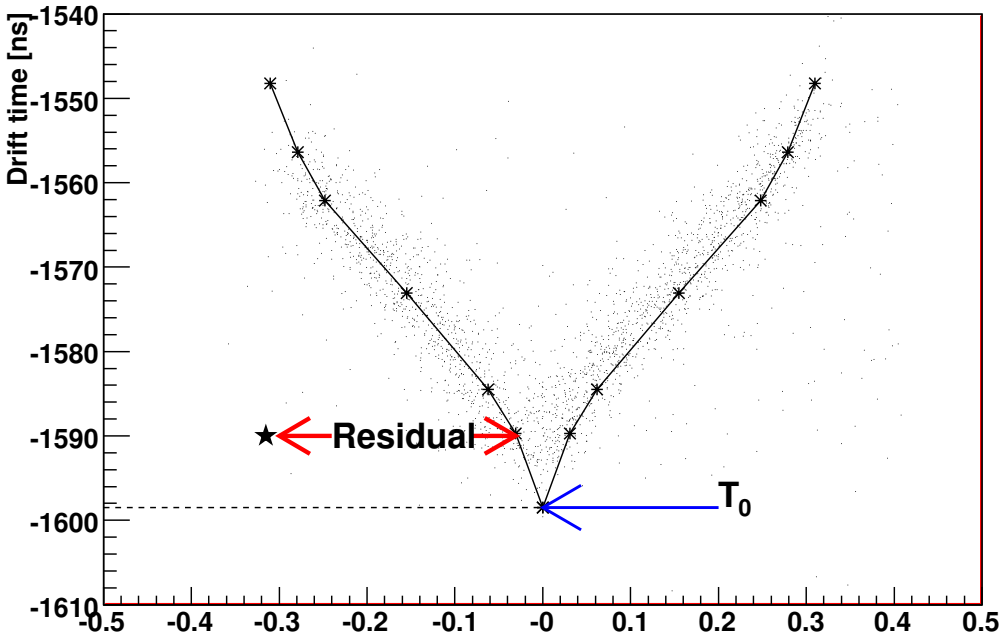

Figure 2.10: Typical V-plot (points) : drift-time recorded by the SDC versus distance obtained from the track information provided by the spectrometer (i.e. a large set of tracking detectors including high resolution trackers like GEMS and Micromegas, at small track angles). RT-relation (solid line) fitted on the V-plot and the resulting T_0. Also shown is a description of the residual : the horizontal distance between a given point (the star) and the nearest *leg* of the RT-relation. One can also see our definition of the drift start time T_0.

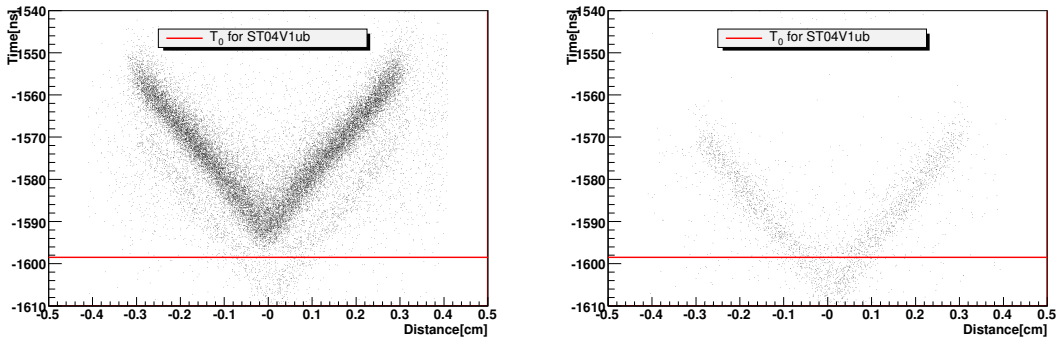

(a) V-plot from one detector

(b) V-plot from one card

Figure 2.11: Extreme, but real case where the V-plot from one card disagrees with the V-plot from the rest of the detector.

straw. If reconstructed track coordinate is denoted as ξ, than:

$$residual = \begin{cases} \xi - (w+d) & \text{if } |\xi - (w+d)| < |\xi - (w-d))| \\ \xi - (w-d) & \text{if } |\xi - (w+d)| \geq |\xi - (w-d))| \end{cases} .$$

Briefly speaking, residual is the shortest distance between track and wire $\pm$ drift distance.

The spread of all residuals from a detector or a card, as in the upper plots of Figure 2.12 and Figure 2.13, gives a good hint of the resolution. Therefore the **resolution** σ estimate is done as the RMS of the residuals distribution within a window of 750 μm[5].

The value σ can be decomposed as:

$$\sigma^2 = \sigma^2_{track} + \sigma^2_{T_0} + \sigma^2_{geom} + \sigma^2_{det}$$

where:

σ_{track} - track reconstruction precision;

σ_{T_0} - precision of T_0 determination converted to a drift distance ($\sigma_{T_0} \approx \Delta T_0 \cdot v$, where v is the drift velocity);

σ_{geom} - geometrical detector precision (i.e. deviation from an ideal detector with parallel, equidistant wires), it is equal $\approx$ 100 μm for a full detector, for half a card (32 channels) it is much smaller;

σ_{det} - the number which is refered as *detector resolution*. It combines all other contributions to the detector resolution (fluctuations of the number of created primary electron-ion pair, drift velocity fluctuation, flucatuations in amplified amplitude signal, etc).

The residual itself is very helpful to give an idea of a detector/card resolution, but it is possible to extract more information from the V-plots. As it can be seen from the lower plots of Figure 2.12 and Figure 2.13, the residuals, if plotted separately for the left and right leg of the V-plot are shifted in the opposite direction when there is a vertical offset of the RT-relation function (i.e. a wrong T_0). The closer the mean of the separated *leg residuals* are to 0, the better is the T_0. This could not have been seen from the overall residuals since the shift of the residuals from one leg compensate for the shift on the other leg. Later, the mean of the leg residuals will show the improvement of the T_0. These quantities will be used regularly in the following text so the symbols η_{left} and η_{right} are introduced for them: the mean value of the residuals associated to the left (right) leg of the V-plot.

The distance between η_{left} and η_{right}, $\Delta\eta$ is also an informative value since a wrong T_0 should shift the means further appart.

‘

[5]This window is to exclude some background far away from the V-plot

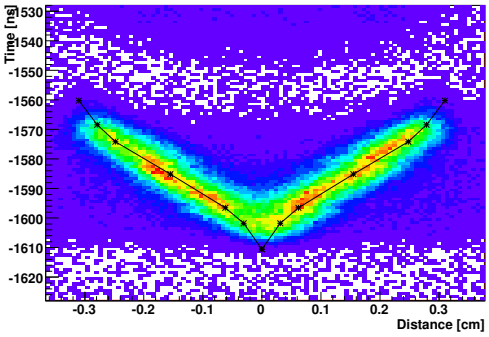

(a) V-plot and fitted RT-relation for the case of a successful fit.

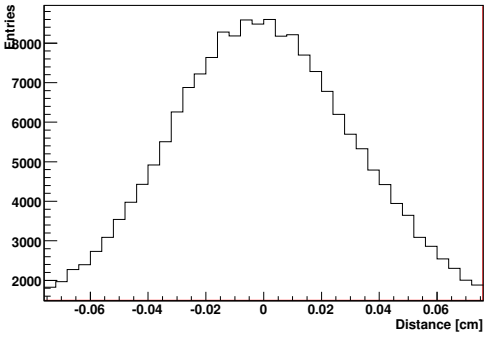

(b) Whole residual distribution

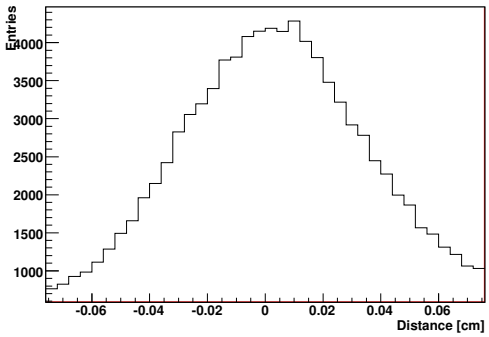

(c) Distribution of the residual from the left leg

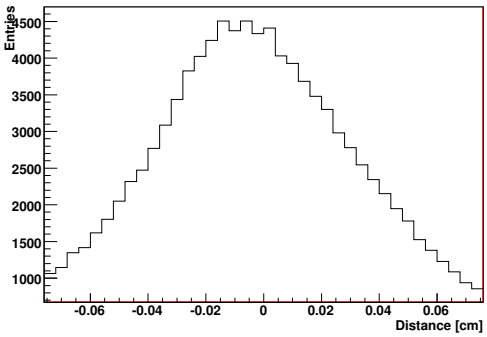

(d) Distribution of the residual from the right leg

Figure 2.12: Good RT-fit and its residuals.

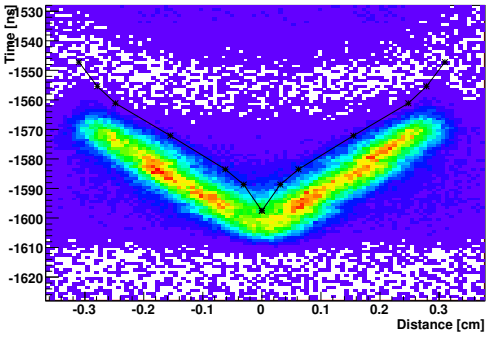

(a) V-plot and fitted RT-relation for the case of an unsuccessful fit.

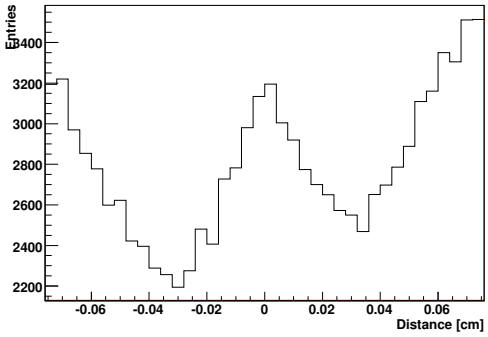

(b) Whole residual distribution

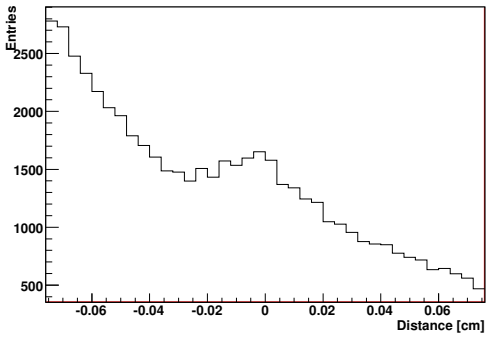

(c) Distribution of the residual from the left leg

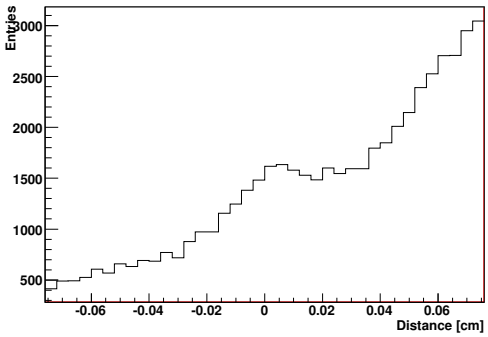

(d) Distribution of the residual from the right leg

Figure 2.13: Bad RT-fit and its residuals.

Defining the parameters of the RT-relation

First of all, the shape of the RT-relation is determined. The RT-relation function is calculated by fitting a V-plot of a reasonable quality[6]. The RT-relation used by the SDC is given by a tabulated function, see Table 2.2 and Table 2.3. The drift distance d for a drift time τ is calculated by linear interpolation between points $[t_i; t_{i+1}]$ of the table, with $t_i \leq \tau < t_{i+1}$.

Table 2.2: RT for 6-mm straw tubes

Point number i	1	2	3	4	5	6	7
Drift time τ $[ns]$	0	10.4	15.2	27.4	40.4	49.3	58.4
Drift distance d $[cm]$	0	0.033	0.066	0.165	0.264	0.297	0.33

Table 2.3: RT for 10-mm straw tubes

Point number i	1	2	3	4	5	6	7
Drift time τ $[ns]$	0	13.0	19.8	36.4	57.0	65.9	83.4
Drift distance d $[cm]$	0	0.048	0.096	0.240	0.384	0.432	0.48

[6] A V-plot for the RT-relation fit procedure does not need to be perfect. V-plots may be fat (due to a bad resolution), the V-plot background may be big, but as long as the plot has enough entries, the determination of the RT-relation is not a problem.

Fitting the V-plots with the RT-relation

A V-plot is fitted by one of the two fixed RT functions presented in Table 2.2 and Table 2.3, depending on the straw diameter size. The fit has two free parameters: the wire position w_0 and the zero drift time T_0 which determine the origin of the V. Subject of the present section is only the T_0 variation.

To remind, a single X- or Y- type detector has an internal structure such that an *upstream* and *downstream* layer together form a double layer (DL). A single electronic card reads both of them. One half of a card (32 channels) reads a part of an upstream layer and another half reads a downstream layer[7]. For every card the two V-plots are created: one for the upstream and another for the downstream layers. So after a V-plot fit, two T_0s are available: T_0^u and T_0^d. Because it is assumed that possible T_0 variations among cards are due to different cable lengths and every card has a single readout cable, these T_0^u and T_0^d values should be identical. In reality they are different, because of the statistical fluctuations and some systematic effects. The distribution of the difference $T_0^u - T_0^d$ plotted for all cards gives a very good hint about the precision σ_{T_0} of the T_0 determination[8]. The distribution of $T_0^u - T_0^d$ difference plotted for all analyzed cards is shown on the Figure 2.14(a) and Figure 2.14(b). From the σ value of the gaussian fit one can estimate the precision of the T_0 extraction:

$$\sigma_{T_0} = \frac{\sigma_{fit}}{\sqrt{2}}.$$

It is approximately equal to $\sigma_{T_0} = \frac{0.31ns}{\sqrt{2}} = 0.22\ ns$

[7] With exception to the cards next to the physical hole in X-type chambers where only 2x31 channels are used

[8] One has to assume that σ_{T_0} is the same for all cards. In principle this is not correct. The method of T_0 calculation is sensitive to the number of V-plot entries, but the amount of data coming from different cards is very different (by a factor $1 \ldots 10^5$). Apparently this is not a problem - the distribution $T_0^u - T_0^d$ has a nice gaussian shape (see 2.14(b)), so the hypothesis about stable σ_{T_0} is safe.

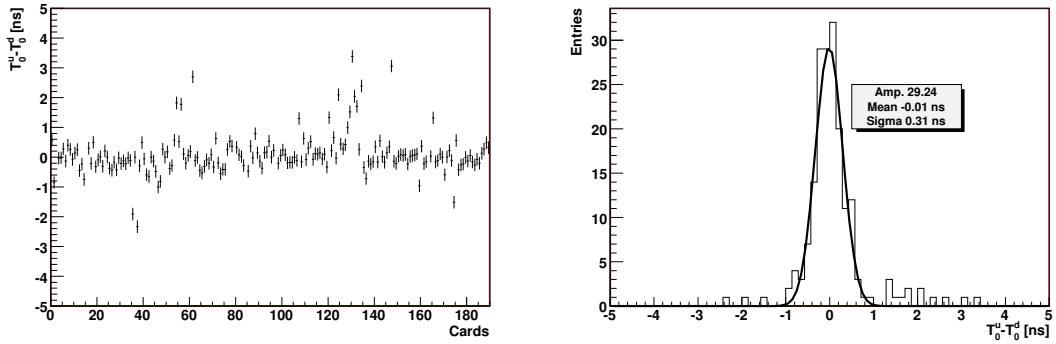

(a) $T_0^u - T_0^d$ for each card

(b) Distribution of $T_0^u - T_0^d$

Figure 2.14: Difference between the T_0 fitted on the upstream straws, T_0^u, and downstream straws, T_0^u. They are assumed to be equal, so the distribution of the difference (right plot) is used to get the error of the T_0 fitting.

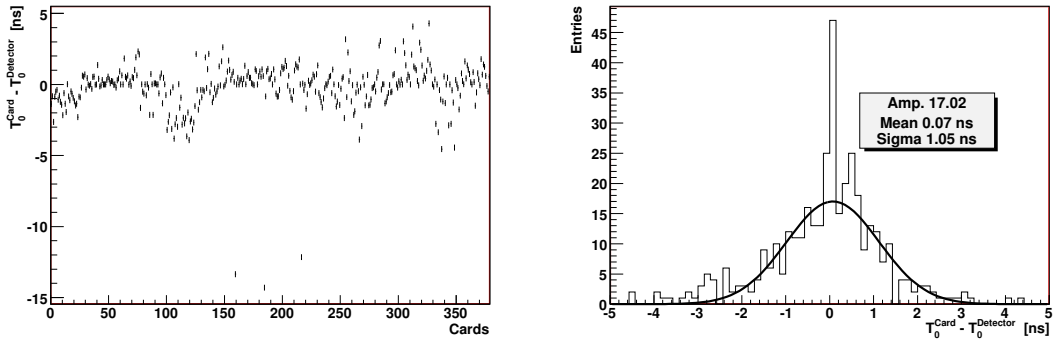

(a) $T_0^{Card} - T_0^{Detector}$ for each card. The error bars are the sigma from the fit in 2.14(b). The three cards in the middle are the obvious case described in Figure 2.11.

(b) Distribution of ΔT_0^{C-D}

Figure 2.15: ΔT_0^{C-D}: Difference between the T_0 given by the fit, T_0^{Card}, and the T_0 used for the whole detector, $T_0^{Detector}$. The bin $T_0^u - T_0^d = 0$ is over-populated compared to the fitted gaussian. This is probably a sign of the fit's dependance on the starting position which is favored over the neighboring T_0.

Study of the fit output

Once the fit has been performed, one needs some way to check whether the fit actually did what is expected. First of all, the fit itself is checked, if it converged to a reasonable value. The only safe way to do this is by looking at all the fitted RT relation over the data like in the upper left plot from Figure 2.12 and Figure 2.13. This may seem like an tedious task, but the eye is very efficient to know if the T_0 and w_0 are reasonable. Table 2.4 and Table 2.5 show statistics of fit problems and their fix, respectively, used for our analysis. In the case of fit problems, the following (ordered) fix procedure is applied :

1. A card shares two detectors, take up(down) stream T_0 from the same card.
2. Take the average of neighbouring cards (excluding the card above the physical hole).
3. Take the old calibration value (the T_0 used for the whole detector).

Table 2.4: Statistics about the cases where the fit results provided a wrong T_0

Problem description	Number of cards affected	Fraction of all cards
Bad data	13	3.3%
No data	8	2.1%
Bad fit	11	2.8%
All	32	8.2%

Table 2.5: Fixed T0 statistics for the cases where the V-plot fitting did not work

Fix	Number of corrected T_0	Fraction of corrected T_0
up/down	11	34.4%
average	13	40.6%
reference	8	25.0%

2.4.3 T_0 calibration results

In this section, the results of providing each cards with its fitted T_0 are shown. To see the effect, two sets of data are looked at: one produced by CORAL with the standard calibration, one T_0 per detector, and a second sample where the same CORAL is using one T_0 per card. These samples will be referd as *calibrated per detector* and *calibrated per card*, respectively. The two values defined previously will be checked: the mean residual from the left (right) leg of the V-plot, η_{left} (η_{right}) and the resolution. The sample studied is taken from 2004, run 37059.

The new T_0 constants

As defined in the previous section, the mean residual from the left and right leg is used to check the improvement of the T_0s. Figure 2.16(a) and Figure 2.16(c) show the mean leg residual for every cards before and after T_0 calibration, respectively. A clear improvement of the spread is observed. It is also seen that when the calibration is applied per card, the mean residual is systematically positive for the left leg and negative for the right leg. This means that there are more hits between the leg of the V-plot than outside, which is understandable since the hits from left and right leg combine between the legs and their residuals add up there.

The distribution of distance between the leg mean residual can also be compared as shown in Figure 2.16(b) and Figure 2.16(d). The mean of the distribution reduces by a factor about 0.5 indicating again an improvement of the V-plot description by the RT function with the fitted T_0.

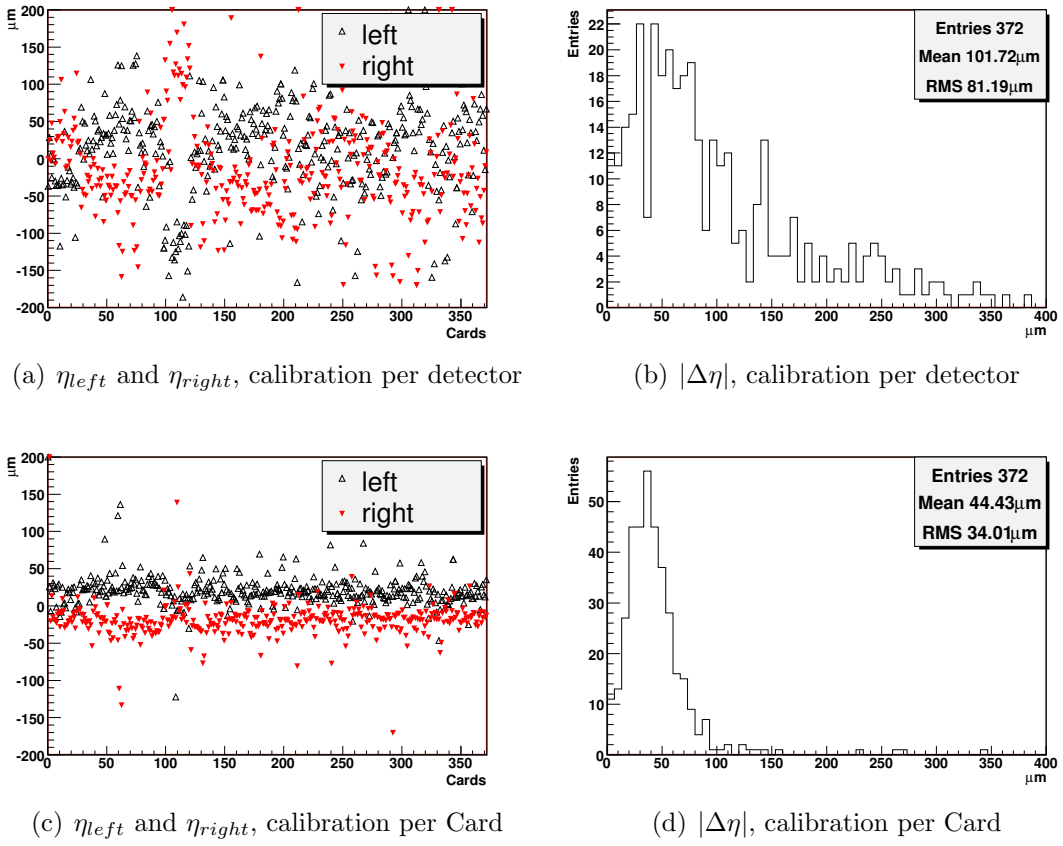

(a) η_{left} and η_{right}, calibration per detector

(b) $|\Delta\eta|$, calibration per detector

(c) η_{left} and η_{right}, calibration per Card

(d) $|\Delta\eta|$, calibration per Card

Figure 2.16: LEFT : Mean leg residual, η_{left} and η_{right} for every cards. RIGHT : Distance between mean leg residual, $\Delta\eta = \eta_{left} - \eta_{right}$ for every cards. UP : Calibration per detector. DOWN : Calibration per cards.

Effect on the resolution

After having demonstrated that the new T_0 values describe more accurately the data from the V-plots of the readout cards, one can look at the resolution. 2.17(a) and 2.17(c) show the resolution for every card before and after T_0 calibration, respectively. The 2.17(b) and 2.17(d) are the projections of the previous plots. The mean resolution for all the cards is reduced by less that $10\mu m$, which is less than expected considering that the new T_0 values are separated by a sigma of $1.15ns$ from the old T_0 (see 2.15(b)). The problem is that the entries in 2.15(b) do not really follow a gaussian distribution. Indeed, it must be noted that the $T_0^{Detector}$ was taken from the cards in the center of the detector. The number of tracks is distributed exponentially around the beam such that T_0 was already fitted for the central cards. No improvements are expected of the resolution for those cases, so they *dilute* the resolution improvement. Therefore, the analysis is done on subsamples of cards where the new calibration, T_0^{Card} is not too close from the old one, $T_0^{Detector}$. Going back to the extreme cases, where $\Delta T_0^{C-D} \equiv T_0^{Card} - T_0^{Detector}$ is more than $10\mu m$, there is an obvious improvement as can be seen from Table 2.6. As shown in Figure 2.18, there is a clear improvement of the resolution distribution for different card selections on their ΔT_0^{C-D}.

Table 2.6: Resolution for cards above the physical hole where $|\Delta T_0^{C-D}| = |T_0^{card} - T_0^{detector}| > 10ns$. One can see that per card the T_0 calibration significantly improves the resolution for the selected cards.

Detector	$\lvert\Delta T_0^{C-D}\rvert$ $[ns]$	Resolution $[\mu m]$ obtained after T_0 calibration	
		per detector	per card
ST04X1ub	12.15	398	297
ST04X1db	12.15	441	291
ST04Y1ub	14.30	410	315
ST04Y1db	14.30	387	312
ST04V1ub	13.35	435	274
ST04V1db	13.35	360	274

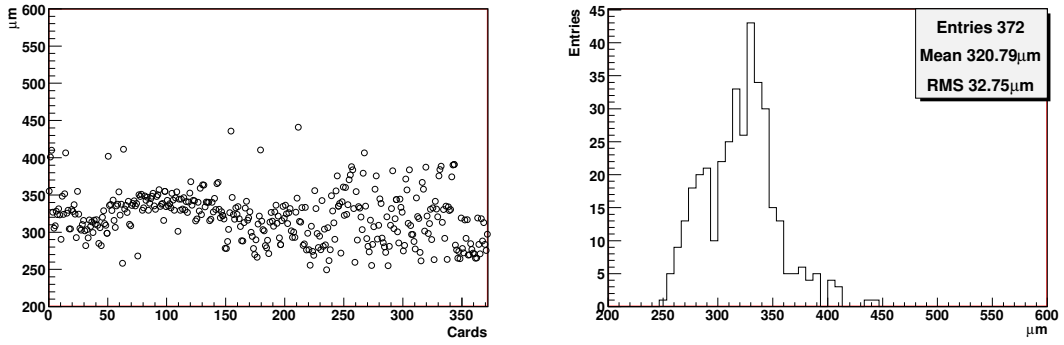

(a) Resolution for every card, calibration per detector

(b) Resolution distribution, calibration per detector

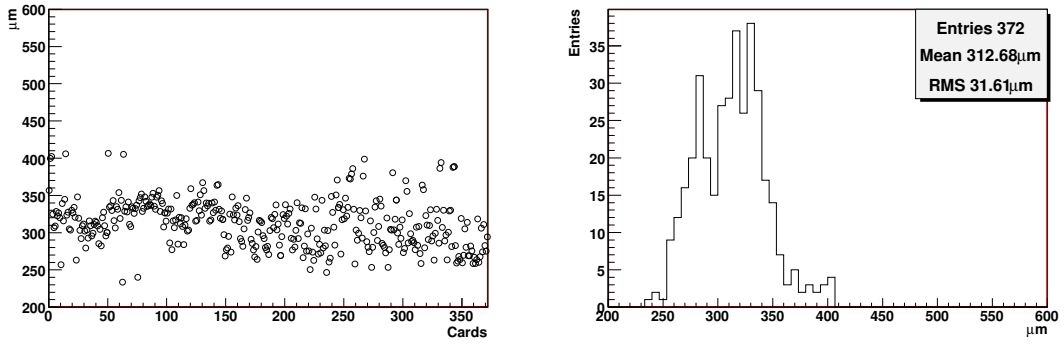

(c) Resolution for every card, calibration per card

(d) Resolution distribution, calibration per card

Figure 2.17: LEFT : Resolution for every cards. RIGHT : Distribution of resolution. UP : Calibration per detector. DOWN : Calibration per cards.

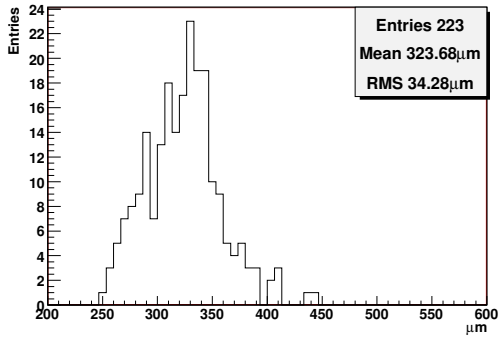

(a) $|\Delta T_0^{C-D}| > 0.5ns$, old T_0

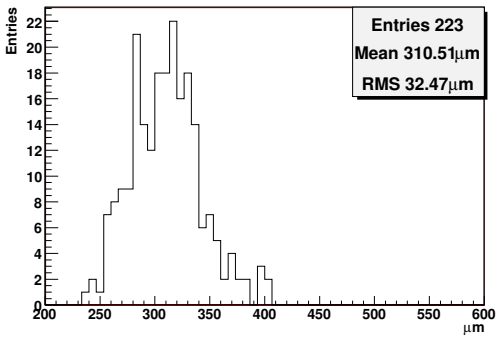

(b) $|\Delta T_0^{C-D}| > 0.5ns$, new T_0

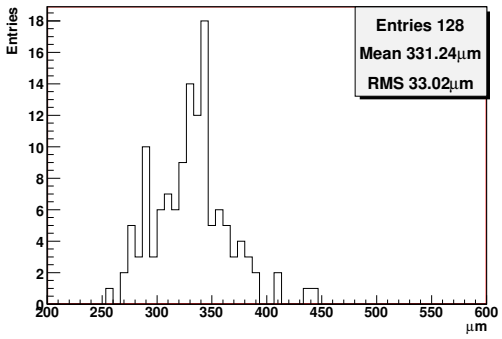

(c) $|\Delta T_0^{C-D}| > 1ns$, old T_0

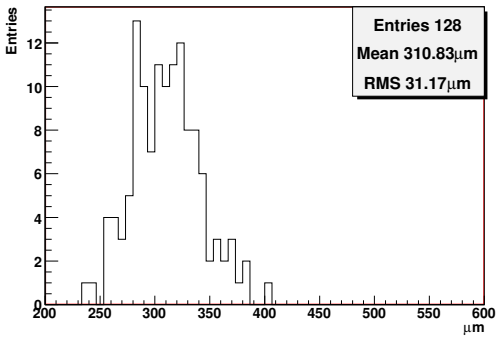

(d) $|\Delta T_0^{C-D}| > 1ns$, new T_0

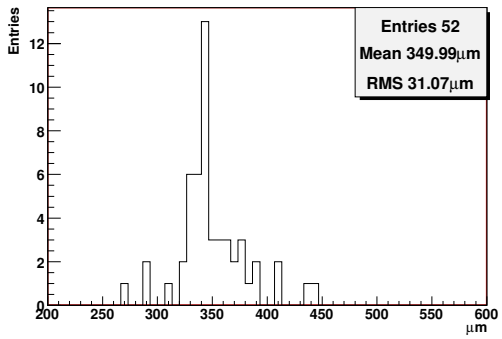

(e) $|\Delta T_0^{C-D}| > 2ns$, old T_0

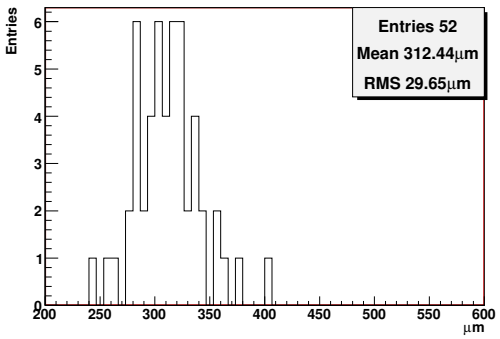

(f) $|\Delta T_0^{C-D}| > 2ns$, new T_0

Figure 2.18: LEFT : Resolution distribution for calibration per detector. RIGHT : Distribution of resolution for calibration per card. Every row has a different card sample selected on the offset of the new T_0 calibration : $\Delta T_0^{C-D} \equiv T_0^{Card} - T_0^{Detector}$

2.4.4 Conclusion of the T_0 calibration procedure

The procedure of the drift start time (T_0) determination per card was sucessfully applied for the calibration of the SDC. The improvement is clearly seen on the mean of residuals on each leg of the V-plots ($\eta_{left,right}$). There were three cards where the T_0 changed by more that $10ns$, on all the cards above the physical hole of the ST04 submodule. In these cases, the resolutions improved dramatically, around $100\mu m$. The effect on the overall resolution is small, below $10\mu m$ which means that most detectors were already well calibrated. But on a subsample of 128 cards, there is a mean improvement of about $20\mu m$ and for 52 cards, it is almost $40\mu m$.

In conclusion, the calibration of the drift start time (T_0) for the SDC is necessary in order to account for different cabling from card to card. It is also a more accurate description of the detector and clearly improves the resolution. The method is available in CORAL and the calibration database is filled with the T_0 constants.

Chapter 3

Open Charm Leptoproduction

High energetic scattering of leptons (electrons, muons and neutrinos) on nucleons is a very important tool for nucleon structure investigation. The leading process in case of charged leptons (e, μ) at an energy of 160 GeV is that a virtual photon emitted by the muon interacts with electrically charged constituents of the nucleon, quarks. Isolating the single photon exchange (or in a case of neutrino interactions, exchange of $W^{\pm}$ and Z bosons) allows to determine the quark distribution functions. Yet, interactions with the electrically neutral constituents, the gluons, are also possible by a somewhat more complicated mechanism: the Photon-Gluon Fusion (PGF), see Figure 3.1. The PGF process is detailed in the present chapter.

3.1 Notations

Accross the chapter the following notations are used.

Particles

μ, $\mu^{'}$ - incoming (beam) and scattered muon

γ^{*} - virtual photon

g - gluon

N - target nucleon

X - target fragments

$q, \bar{q}$ - quark and antiquark (any flavor)

$c, \bar{c}$ - charm quark and its antiquark

Variables

m_N - nucleon mass

Figure 3.1: Photon-gluon fusion process. The virtual photon γ^* emitted by the muon μ interacts with a gluon g from a nucleon target N. A quark-antiquark pair $q\bar{q}$ is produced as a result of the interaction.

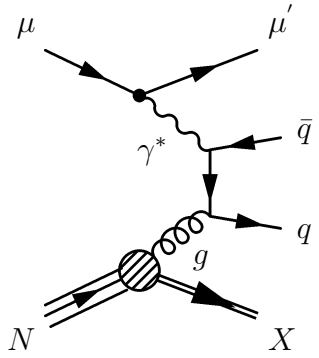

m_c - charm quark mass

E - incoming muon μ (beam) energy

E' - scattered muon μ' energy

ν - muon energy loss: $\nu = E - E' = E_{\gamma^*}$

$y = \nu/E$ the fraction of the muon's energy lost in the nucleon rest frame (laboratory system)

Q^2 - negative γ^* 4-momentum squared $Q^2 = -(p_{\gamma^*})^2$ $(Q^2 > 0)$

$\hat{s}$ - center of mass energy of the γ^* and gluon system $(\gamma^* g)$: $\hat{s} = (p_g + p_{\gamma^*})^2$

x - Bjorken variable: $x = Q^2/(2m_N\nu)$

x_g - momentum fraction of the nucleon carried by the gluon: $x_g = \hat{s}/(2m_N\nu)$

3.2 Cross Sections

A general formula for the lepton(μ)-nucleon(N) scattering $\mu N \to \mu' X$ cross section by single photon exchange is given by:

$$\frac{d^2\sigma^{\mu N}}{dE' d\Omega} = \frac{\alpha^2}{Q^4}\frac{E'}{E} L^{\mu\nu} W_{\mu\nu}$$

where $L^{\mu\nu}$ is the leptonic and $W_{\mu\nu}$ is the hadronic tensor, E is the incoming and E' the scattered lepton energy, and Ω is the scattered lepton solid angle. The cross section can be rewritten in terms of the structure functions F_1, F_2 as follows:

$$\frac{d^2\sigma^{\mu N}}{dx dQ^2} = \frac{4\pi\alpha^2}{Q^4 x}\left[xy^2 F_1(x,Q^2) + \left(1 - y - \frac{\gamma^2 y^2}{4}\right) F_2(x,Q^2)\right]$$

To go from charm muoproduction $\mu N \to Xc\bar{c}$ to the charm (virtual) photoproduction $\gamma^* N \to Xc\bar{c}$ cross section, the concept of virtual photon flux is used:

$$\frac{d^2\sigma^{\mu N \to c\bar{c}X}}{dQ^2 d\nu} = \Gamma(E; Q^2, \nu)\sigma^{\gamma^* N \to c\bar{c}X}(Q^2, \nu)$$

with the virtual photon flux:

$$\Gamma(E; Q^2, \nu) = \frac{\alpha_e}{2\pi}\frac{2(1-y) + y^2 + Q^2/2E^2}{Q^2(Q^2+\nu^2)^{1/2}}$$

The relation between virtual photon cross section and real photon (photoproduction) cross section is given by

$$\sigma^{\gamma^* N \to c\bar{c}X}(Q^2, \nu) = \frac{\sigma^{\gamma N \to c\bar{c}X}(\nu)}{1 + Q^2/M_0^2}$$

where the mass parameter M_0 is known from a fit of experimental data.

3.3 Photon-Gluon Fusion Cross Section and Asymmetry

The function $G_{ab}(x_g)$ describes the gluon polarization inside a nucleon [1]. The product $G_{ab}(x_g)dx_g$ gives the probability to find a gluon with a helicity a in a nucleon with a helicity b while the gluon carries the fraction x_g of the nucleon momentum. Nucleon and gluon helicities may have only two states which are indicated with the + and the − signs below. Due to parity considerations $G_{++} = G_{--}$ and $G_{+-} = G_{-+}$.

For the $\gamma^* N$ cross section $\sigma_{ab}^{\gamma^* N \to c\bar{c}X}$ the indices a, b also indicate the photon and the nucleon helicities (again ± signs will be used below). By using the factorization theorem [29], this cross section can be written as a convolution of a gluon structure function and the PGF subprocess cross section $d\sigma_{ab}^{\gamma^* g \to c\bar{c}}$ (where a are the photon - and b the gluon helicities; by parity $\sigma_{++}^{\gamma^* g \to c\bar{c}} = \sigma_{--}^{\gamma^* g \to c\bar{c}}$ and $\sigma_{+-}^{\gamma^* g \to c\bar{c}} = \sigma_{-+}^{\gamma^* g \to c\bar{c}}$):

$$d\sigma_{++}^{\gamma^* N \to c\bar{c}X}(x_g, \hat{s}) = G_{++}(x_g)d\sigma_{++}^{\gamma^* g \to c\bar{c}}(\hat{s}) + G_{-+}(x_g)d\sigma_{+-}^{\gamma^* g \to c\bar{c}}(\hat{s}) \quad (3.1)$$

$$d\sigma_{+-}^{\gamma^* N \to c\bar{c}X}(x_g, \hat{s}) = G_{+-}(x_g)d\sigma_{++}^{\gamma^* g \to c\bar{c}}(\hat{s}) + G_{--}(x_g)d\sigma_{+-}^{\gamma^* g \to c\bar{c}}(\hat{s}) \quad (3.2)$$

The cross section spin asymmetry may be written as

$$A^{\gamma^* N \to c\bar{c}X} = \frac{\int (d\sigma_{++}^{\gamma^* N \to c\bar{c}X} - d\sigma_{+-}^{\gamma^* N \to c\bar{c}X})}{\int (d\sigma_{++}^{\gamma^* N \to c\bar{c}X} + d\sigma_{+-}^{\gamma^* N \to c\bar{c}X})} \quad (3.3)$$

$$= \frac{\int \Delta d\sigma^{\gamma^* N \to c\bar{c}X}}{\int d\sigma^{\gamma^* N \to c\bar{c}X}} \quad (3.4)$$

$$= \frac{\int \Delta G \cdot \Delta d\sigma^{\gamma^* g \to c\bar{c}}}{\int G \cdot d\sigma^{\gamma^* g \to c\bar{c}}} \quad (3.5)$$

[1] Following the notations from [5].

where

$$
\begin{aligned}
G &= G_{++} + G_{-+} && (3.6)\\
\Delta G &= G_{++} - G_{-+} && (3.7)\\
d\sigma^{\gamma^* g\to c\bar{c}} &= d\sigma^{\gamma^* g\to c\bar{c}}_{++} + d\sigma^{\gamma^* g\to c\bar{c}}_{+-} && (3.8)\\
\Delta d\sigma^{\gamma^* g\to c\bar{c}} &= d\sigma^{\gamma^* g\to c\bar{c}}_{++} - d\sigma^{\gamma^* g\to c\bar{c}}_{+-} && (3.9)
\end{aligned}
$$

The PGF cross section $\sigma^{\gamma^* g\to c\bar{c}}_{ab}$ can be calculated in LO of QCD [30], in the limit $Q^2 \approx 0$ it is given by:

$$
\begin{aligned}
\Delta\sigma^{\gamma^* g\to c\bar{c}}(\hat{s}) &= \frac{4}{9}\frac{2\pi\alpha_e\alpha_s(\hat{s})}{\hat{s}}\left[3\beta - \log\frac{1+\beta}{1-\beta}\right] && (3.10)\\
\sigma^{\gamma^* g\to c\bar{c}}(\hat{s}) &= \frac{4}{9}\frac{2\pi\alpha_e\alpha_s(\hat{s})}{\hat{s}}\left[-\beta(2-\beta^2) + \frac{1}{2}(3-\beta^4)\log\frac{1+\beta}{1-\beta}\right] && (3.11)
\end{aligned}
$$

where $\hat{s}$ is the invariant mass square of the $\gamma^* g$ system and β is the c.m. velocity of the charmed quark:

$$\beta = \sqrt{1 - 4m_c^2/\hat{s}}$$

The ratio of helicity dependent and helicity independent PGF cross sections is usually denoted as $\hat{a}_{LL}$:

$$\hat{a}_{LL} = \frac{\Delta\sigma^{\gamma^* g\to c\bar{c}}}{\sigma^{\gamma^* g\to c\bar{c}}} \qquad (3.12)$$

The final formula for the PGF asymmetry is obtained after integration of the cross sections over all unobserved variables:

$$A^{\gamma^* N\to c\bar{c}X} = \frac{\Delta\sigma^{\gamma^* N\to c\bar{c}X}(\hat{s})}{\sigma^{\gamma^* N\to c\bar{c}X}(\hat{s})} = \frac{\int_{4m_c^2}^{2m_N Ey} d\hat{s}\int dx_g\ \Delta\sigma^{\gamma^* g\to c\bar{c}}(\hat{s})\Delta G(x_g,\hat{s})}{\int_{4m_c^2}^{2m_N Ey} d\hat{s}\int dx_g\ \sigma^{\gamma^* g\to c\bar{c}}(\hat{s}) G(x_g,\hat{s})} \qquad (3.13)$$

where the integration limits for the fractional gluon momentum x_g are determined by the detector acceptance for D-mesons.

To extract $\Delta G/G$ from the asymmetry, the following assumption is made:

$$A^{\gamma^* N\to c\bar{c}X} \approx \langle\hat{a}_{LL}\rangle \cdot \langle\frac{\Delta G}{G}\rangle \qquad (3.14)$$

where the average $\langle\rangle$ is over the x_g range covered by the detector.

The muon nucleon asymmetry $A^{\mu N\to c\bar{c}X}$ is related to the virtual photon asymmetry $A^{\gamma^* N\to c\bar{c}X}$ by:

$$A^{\mu N\to c\bar{c}} = D(y)\cdot A^{\gamma^* N\to c\bar{c}} \qquad (3.15)$$

where $D(y)$ is the depolarization factor:

$$D(y) \approx \frac{1-(1-y)^2}{1+(1-y)^2} \qquad (3.16)$$

In a hypothetical muon-nucleon scattering experiment which measures event rates $N^{\rightrightarrows}$, $N^{\leftleftarrows}$ when muon and nucleon spins are oriented parallel and anti-parallel in the laboratory system, the relation between the raw experimental asymmetry and the PGF asymmetry Equation 3.13 will be given by:

$$A_{raw}^{\mu N \to c\bar{c}X} = \frac{N^{\leftleftarrows} - N^{\rightrightarrows}}{N^{\leftleftarrows} + N^{\rightrightarrows}} = D P_B P_T A^{\gamma^* N \to c\bar{c}X} \tag{3.17}$$

where P_B is the beam and P_T is the target polarization.

Summarizing, the idea of the $\Delta G/G$ measurement is the following. In a muon-nucleon scattering experiment the observed counting asymmetry $A_{raw}^{\mu N \to c\bar{c}X}$ is related to the photon-nucleon asymmetry by Equation 3.17. This asymmetry being divided by the $\langle \hat{a}_{LL} \rangle$ of the events will give access to the $\Delta G/G$ ratio, see Equation 3.14.

Chapter 4

Data Analysis and Results

4.1 Unpolarized Differential Charm Production Cross Sections

4.1.1 Data Selection

In the muon-nucleon scattering reaction

$$\mu^+ N \to \mu^{+\prime} X Y \tag{4.1}$$

events with a c,$\bar{c}$ quark(s) produced in the final state should be selected. The COMPASS experiment proposed to detect D^* and D^0 mesons in the final state, which are the most frequently produced open charm mesons after fragmentation of a c or $\bar{c}$ quark.

Later in the text when a D^0 symbol is used, it is assumed that both D^0 and $\overline{D^0}$ mesons are involved (unless the difference between D^0 and $\overline{D^0}$ mesons is mentioned explicitly). Similarly, by using D^* the D^{*+} and D^{*-} mesons are assumed. The basic properties of the mesons are listed in the Appendix A.

In the present section criteria will be described for selecting events of the reactions:

$$\begin{aligned}
\mu^+ N &\to \mu^{+\prime} X D^0 \\
&\quad \hookrightarrow D^0 \to K^- \pi^+ \\
\mu^+ N &\to \mu^{+\prime} X \overline{D^0} \\
&\quad \hookrightarrow \overline{D^0} \to K^+ \pi^- \qquad (4.2) \\
\mu^+ N &\to \mu^{+\prime} X D^{*+} \\
&\quad \hookrightarrow D^{*+} \to D^0 \pi^+ \qquad (4.3) \\
&\quad\quad \hookrightarrow D^0 \to K^- \pi^+ \\
\mu^+ N &\to \mu^{+\prime} X D^{*-} \\
&\quad \hookrightarrow D^{*-} \to \overline{D^0} \pi^- \\
&\quad\quad \hookrightarrow \overline{D^0} \to K^+ \pi^-
\end{aligned}$$

The chosen decays of the D^0 and D^* mesons have small branching ratios (see Appendix A), but lead to large signal/background ratio. The data were taken during the years 2002-2004 and 2006. The analysis accepted all triggers (see [24, 26], and section 2.2 of the thesis) which cover a large region of inelasticity and photon virtuality. The integrated luminosity for the entire data sample is about $2.8/fb$. The reconstructed event sample has a size of 26.8 Terabytes and contains $8.3 \cdot 10^9$ DST events.

Before explaining in details the way how D-meson events were selected, the measured invariant $K\pi$ mass spectra are shown for the entire mass range in the Figure 4.1, separately for the various charge combinations. These spectra were extracted from the 2006 data only. The spectra for the 2 neutral combinations show 3 narrow peaks corresponding to $K^*(892)^0$, $K_2^*(1430)^0$ and $D^0(1865)$. The shape of $K^*(892)^0$ is remarkable. So as if the K^* interferes with another resonance. The prominence of these 3 resonances is presumably due to their narrow width. Certainly, there are other short-lived kaonic (strange) resonances present but they superimpose together with combinatorial and other background to a structureless distribution which can almost perfectly be described by a single exponential function, see Figure 4.2.

Figure 4.1: $K\pi$ invariant mass distribution, all four possible charge combinations ($K^-\pi^-$, $K^+\pi^+$, $K^-\pi^+$, $K^+\pi^-$), linear scale for event number. Data are from the year 2006.

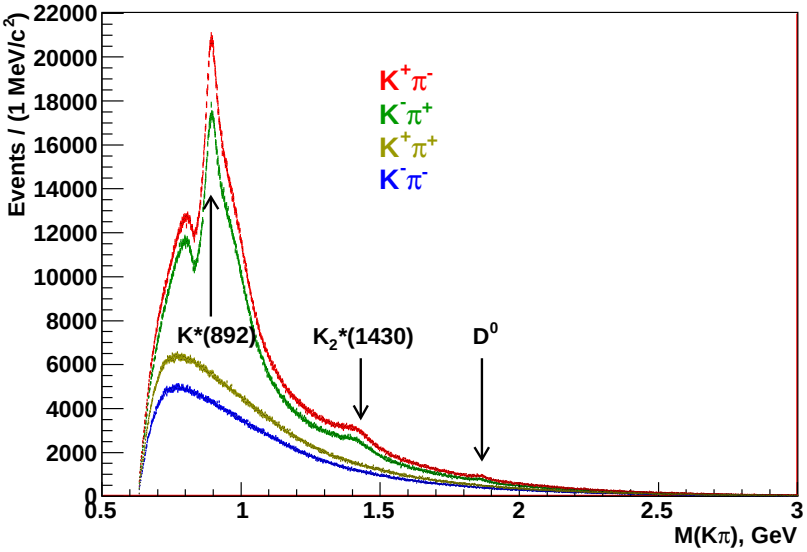

Cuts applied to select D-mesons

The search for events with D-mesons and the reconstruction of the D-mesons involves the following steps. First of all, **basic cuts on event topology** are applied. After that, the **search for D-meson** *candidates* in every event (0,1,2,... candidates may be found per event) is done. At the end, **final cuts on D-mesons** *candidates* are applied.

Figure 4.2: $K\pi$ invariant mass distribution, neutral charge combinations ($K^-\pi^+$ and $K^+\pi^-$), logarithmic vertical scale for event number. Data are from the year 2006.

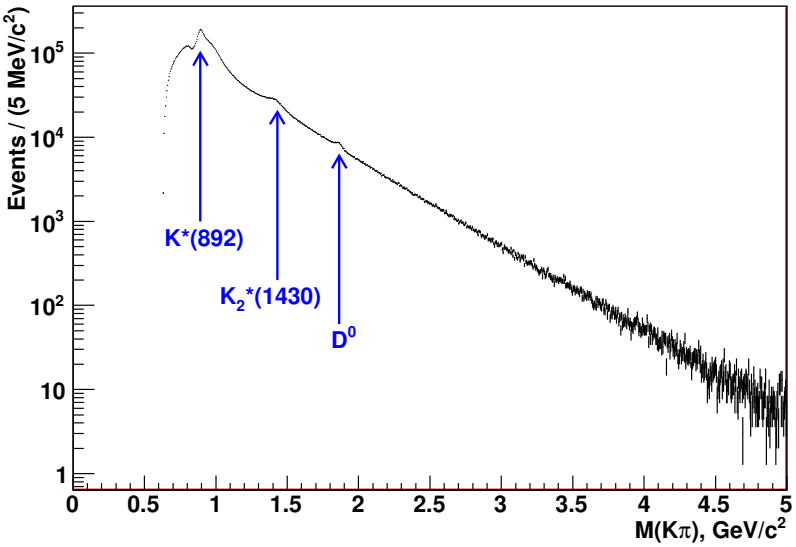

The Table 4.1 contains event reduction and survival rates after the basic cuts on event topology and D-meson candidates search have been performed. The **event counter** denotes the number of input DST events used in the analysis. The **primary vertex** cut removes events without a primary vertex. The check on a presence of a scattered muon in the primary vertex is done with the cut μ'. The minimum number of output tracks (excluding the scattered muon track) from the primary vertex should be two, this is checked with the cut **tracks** $>= 2$. The number of events with either at least one D^0 or at least one D^* candidate is denoted as D^* **or** D^0 **event**. The D^* **event** counts how many events contain at least one D^* candidate. The D^0 **event** counts how many events contain at least one D^0 candidate.

Table 4.1: Numbers of events after the basic cuts on event topology and D-mesons selection.

Cuts	2002	2003	2004	2006
Event counter	$8.37 \cdot 10^8$	$1.58 \cdot 10^9$	$3.24 \cdot 10^9$	$2.69 \cdot 10^9$
Primary vertex	$7.08 \cdot 10^8$	$1.45 \cdot 10^9$	$3.02 \cdot 10^9$	$2.48 \cdot 10^9$
μ'	$5.66 \cdot 10^8$	$1.15 \cdot 10^9$	$1.87 \cdot 10^9$	$1.57 \cdot 10^9$
Tracks $>= 2$	$3.66 \cdot 10^8$	$6.93 \cdot 10^8$	$1.13 \cdot 10^9$	$8.76 \cdot 10^8$
D^* or D^0 event	$4.98 \cdot 10^7$	$8.62 \cdot 10^7$	$1.28 \cdot 10^8$	$1.60 \cdot 10^8$
D^* event	$5.61 \cdot 10^6$	$1.53 \cdot 10^7$	$2.17 \cdot 10^7$	$2.55 \cdot 10^7$
D^0 event	$4.70 \cdot 10^7$	$7.68 \cdot 10^7$	$1.14 \cdot 10^8$	$1.49 \cdot 10^8$

Table 4.2: Number of events and D meson candidates in a mass window $\pm$ 700 MeV around the nominal D mass and of fitted D^* and D^0 mesons after the sequence of cuts applied. All data from the years 2002-2006 summed up

Cuts	D^*	D^0	μ'
	Events		Events
Total number of reconstructed events			$8.3 \cdot 10^9$
Primary vertex with incoming and scattered muon			$5.2 \cdot 10^9$
>= 2 additional tracks	$3.1 \cdot 10^9$		
Events with D^*/D^0 meson candidate(s)	$6.8 \cdot 10^7$	$3.9 \cdot 10^8$	
	Candidates		Events
Total number of D^*/D^0 meson candidates	$1.0 \cdot 10^8$	$1.5 \cdot 10^8$	
$3.2 < \lvert\Delta M\rvert < 8.9\ MeV$	$3.9 \cdot 10^7$		
PID relevant momentum cuts	$3.7 \cdot 10^6$	$1.5 \cdot 10^8$	
PID	$2.8 \cdot 10^5$	$4.8 \cdot 10^7$	
Advanced cuts	$1.7 \cdot 10^5$	$1.8 \cdot 10^7$	
Fiducial target volume cuts	$1.6 \cdot 10^5$	$1.7 \cdot 10^7$	$3.4 \cdot 10^9$
Fitted D^*/D^0 signal	8100	34000	

Selection of D^0 candidates.

All possible track pairs $t_i t_j$ from the best primary vertex are tried to form a $K\pi$ system with the track t_i assigned to kaon K and track t_j to pion π.

A combination $K\pi$ is called a D^0 *candidate*, if

- $|M(K\pi) - M_{PDG}(D^0)| < 700\ MeV$;
- soft Particle Identification (PID) cuts are applied based on RICH likelihoods: for a kaon track $LK(K) > 0.85 \cdot LK(bkg)$ and $LK(K) > 0.85 \cdot LK(\pi)$, for pion tracks $LK(\pi) > 0.85 \cdot LK(bkg)$ and $LK(\pi) > 0.85 \cdot LK(K)$ (see section 2.3);
- only the correct charge combinations are allowed: $K^-\pi^+$ and $K^+\pi^-$;

Selection of D^* candidates.

All possible track triple $t_i t_j t_k$ combinations from the best primary vertex are tried to form a $K\pi\pi_s$ system with the track t_i assigned to kaon K, track t_j to pion π and the last track t_k to pion π_s. Particles $K\pi$ are to form the D^0 mesons and pion π_s is from a $D^{*\pm} \to D^0\pi_s$ decay.

A combination $K\pi\pi_s$ is called a D^* *candidate*, if

- $|M(K\pi) - M_{PDG}(D^0)| < 700\ MeV$;
- $0 < |\Delta M| < 15\ MeV$, with $\Delta M = M(K\pi\pi_s) - M(K\pi) - M(\pi)$;
- only the correct charge combinations are allowed: $K^-\pi^+\pi_s^+$ and $K^+\pi^-\pi_s^-$.

Figure 4.3: $D^{*\pm}$ mesons tagging.

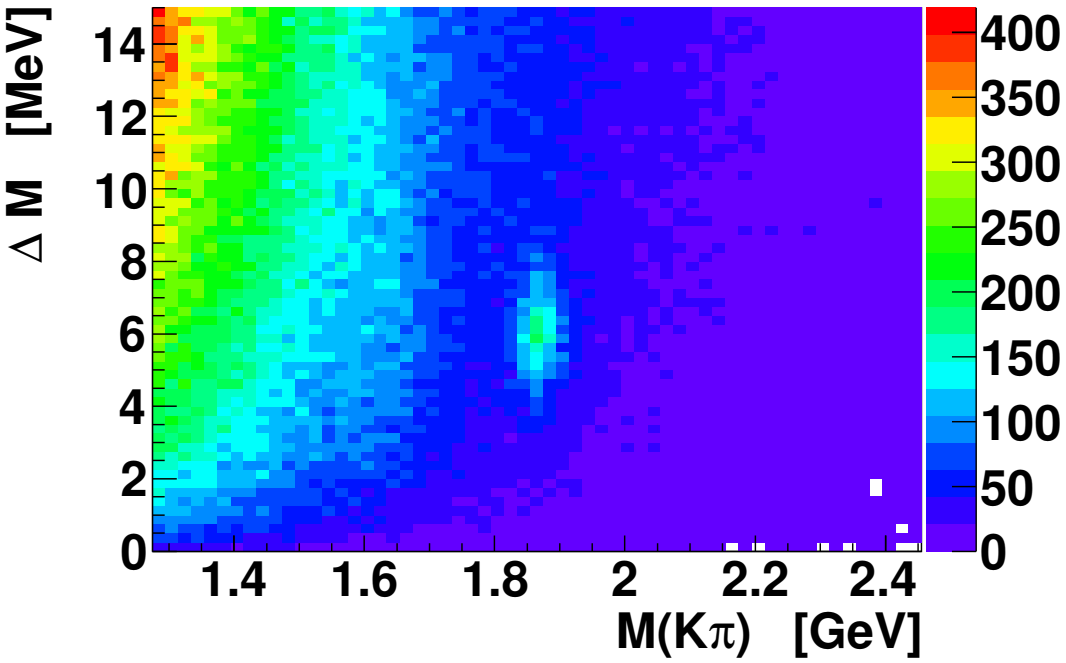

(a) Scatterplot for D^* candidates, before the ΔM cut: Vertical axis: ΔM, horizontal axis: $M(K\pi)$. The accumulation of events around the D^0 nominal mass and around $\Delta M = 6.1\ MeV$ corresponds to the decay sequence $D^* \to \pi_s D^0 \to \pi_s(K\pi)$.

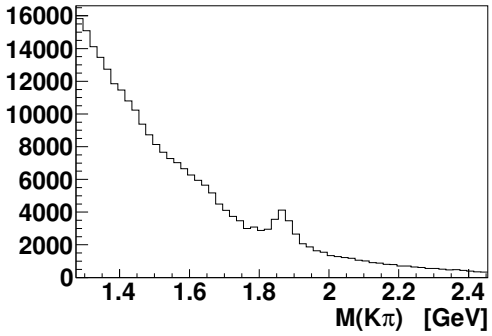

(b) Projection to the $M(K\pi)$ axis for a window $1 < \Delta M < 10\ MeV$

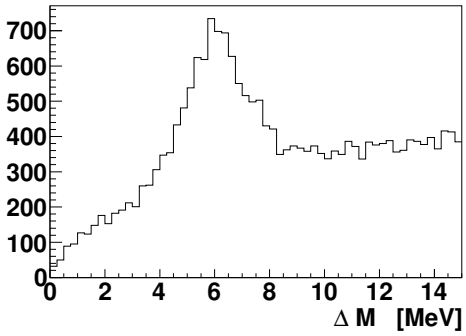

(c) Projection to the ΔM axis for a window $1.80 < M(K\pi) < 1.94\ GeV$

The ΔM cut importance is illustrated in Figure 4.3.

The total number of *events* with D^* and D^0 candidates is $6.8 \cdot 10^7$ and $3.9 \cdot 10^8$, after these (soft) particle identification and invariant mass cuts. The total number of D^* and D^0 *candidate combinations* in the entire mass window is $1.0 \cdot 10^8$ and $5.9 \cdot 10^8$, respectively.

Advanced cuts on D-mesons

As a final step, advanced cuts are applied to D^0 and D^* meson candidates.

Table 4.3: Particle identification details for D^* and D^0 sample: Choices of likelihood ratios, see section 2.3.

year	kaon ID		pion ID		electron rejection for π_s		
	$\frac{LK(K)}{LK(\pi)} >$	$\frac{LK(K)}{LK(bkg)} >$	$\frac{LK(\pi)}{LK(K)} >$	$\frac{LK(\pi)}{LK(bkg)} >$	$\frac{LK(e)}{LK(bkg)} <$	$\frac{LK(e)}{LK(\pi)} <$	$\frac{LK(e)}{LK(K)} <$
			D^*				
2002	0.99	0.99	1.00	1.00	1.5	1.0	1.0
2003	0.97	0.99	0.90	0.99	1.5	1.5	1.0
2004	1.02	0.95	0.90	0.99	1.5	1.5	1.0
2006	1.05	0.99	0.90	0.99	2.0	1.5	1.0
			D^0				
2002	0.98	1.15	1.00	1.00			
2003	1.02	1.05	0.90	0.99			
2004	1.02	1.05	0.90	0.99			
2006	1.10	0.99	0.90	0.99			

Stricter cuts for particle identification are applied, see Table 4.3. The ΔM window for the D^* is narrowed down: $3.2 MeV < |\Delta M| < 8.9 MeV/c^2$. A scatter plot ΔM versus M($K\pi$) is shown, before this ΔM cut, together with the projections, for the D^* *sample*, see Figure 4.3.

The following cuts, illustrated in Figure 4.4, were applied in order to increase the signal to background ratio without much reducing the signal. For the D^0 sample a cut on the energy of the (fast) pion from the D decay demands that it be larger than 7 GeV, but no cut is applied to the momentum of the slow pion (see Figure 4.4(a) and Figure 4.4(b)). The kaon energy is limited to the range 8.9 to 50 GeV, to allow particle identification with the RICH detector (Figure 4.4(c)).

A lower limit on the scaling variable $z_D = E_{D^0}/E_\gamma$ is imposed for both samples: $z_D > 0.2$ (Figure 4.4(d)). To remind, at this stage of data selection, the subscript D refers to a $K\pi$ combination considered being a D meson - candidate. Cuts on the cosine of the decay angle of the K in the cm system of the D^0 candidate are applied. $|cos(\Theta_K)| < 0.65$ for the D^0 candidate and $|cos(\Theta_K)| < 0.9$ for the D^* candidate (Figure 4.5).

Since the purpose of all these cuts is to reduce background without reducing much signal, in all cases the distribution of the finally accepted D signal events are also shown to demonstrate that these cuts indeed reduce the signal only insignificantly but background quite significantly.

The $cos(\Theta_K)$ distribution is the only distribution where a safe theoretical prediction can be made - it should be flat, after acceptance correction, for the signal events, since the D^0 has spin 0. Therefore, in Figure 4.5 the acceptance corrected distribution within the limits after the cut $|cos(\Theta_K)| < 0.9$ for the D^* is shown. How the acceptance correction was calculated will be explained below.

Finally, a target cut makes sure that the incoming muon may hit both (or in the year 2006 all three) target cells and that the primary vertex is safely associated with one or the other of the target cells. This cut would not be necessary for the study of the unpolarized charm production distributions and cross sections, but is needed for the asymmetry measurement.

After these advanced cuts the final D^* - tagged sample (in short D^* - *sample)* of events with 160k neutral $K\pi$ combinations in the mass window of $\pm 700\ MeV$ has been obtained. In order to make the samples non-overlapping, the D^* candidates are taken out of the D^0 sample, at the very end. This latter sample is then called in short D^0 - *sample*. It comprises 17 Million neutral $K\pi$ combinations in the mass window of $\pm 700\ MeV$.

In Figure 4.6 the invariant mass spectrum is shown for the D^0 -*sample* and D^* -*sample* before (Figure 4.6(a)(c)) and after (Figure 4.6(b)(d)) background subtraction. The spectra are shown summed and also separately for $K^-\pi^+$ and $K^+\pi^-$ combinations. These spectra show the signal peak searched for, at the nominal D^0- mass of 1865 MeV. The prominent peak to the left has already been seen in Figure 4.1,Figure 4.2, it is to be attributed to the narrow $K_2^*(1430)^0$. Furthermore, a shoulder or peak, about 250 MeV below the nominal D^0 -peak position can be seen (it is much more significant for the D^*-*sample*). For the Figure 4.6(d) only some feed-through of the $K_2^*(1430)^0$ resonance and a pronounced, rather narrow peak about 250 MeV below the nominal D^0 -peak position, can be seen. This peak at 1620 MeV can be shown, by Monte Carlo simulations, to be caused mainly by 3-body decays of the $D^0 \to K\pi\pi^0$, where the π^0 escaped detection, but also by decays with more than 3 particles.

The number of charm events is extracted from the invariant $K\pi$ mass spectra, for the two data samples, D^0 and D^*, after all cuts. It can be seen that the signal to background ratio is much better (about 1:1) for the events, where the D^0 and one additional pion have satisfied the ΔM cut described above. For the D^0 sample, without a D^*, the signal to background ratio is 1:10 but the number of signal events is a factor 7 higher.

To determine the number of good (signal) D^0 -events the invariant $K\pi$-mass spectra shown in Figure 4.6 were fitted by an exponential for the background, a Gaussian with 3 free parameters for the width, mass and height of the D^0 2-body decay signal, a special shape determined by Monte Carlo simulations for 3- and more- body decays of the D^0 (i.e. the peak at 1650 MeV) and relativistic Breit-Wigner intensities for the $K_2^*(1430)^0$ and $K_3^*(1780)$, see below. The data are remarkably well described in this simple way.

The number of D^0 mesons (two body decay) extracted by fit from the spectra Fig-

ure 4.6(a) and Figure 4.6(c) are shown in Table 4.4. For the combined event samples (without the D^* tag check) the number of $K_2^*(1430)^0$ and $K_3^*(1780)^0$ mesons extracted by fit are shown as well.

Table 4.4: Number N of mesons D^*, D^0, $K_2^*(1430)^0$, $K_3^*(1780)^0$ extracted from the fit after all cuts applied, data of the years 2002-2006. The fit functions are described in Appendix B.

Meson M	Events sample	$N(M+\bar{M})$	$N(M \to K^-\pi^+)$	$N(\bar{M} \to K^+\pi^-)$
D^* (M=D^0 from D^*)	D^*	8136 ± 132	3629 ± 90	4535 ± 97
D^0	D^0	33661 ± 1190	15219 ± 807	18437 ± 877
$K_2^*(1430)^0$	D^*+D^0	1008995 ± 4610	435224 ± 3065	574211 ± 3443
$K_3^*(1780)^0$	D^*+D^0	88145 ± 3719	37351 ± 2473	51209 ± 2778

Figure 4.4: Kinematical distributions for D^*-meson candidates before and after advanced cuts.

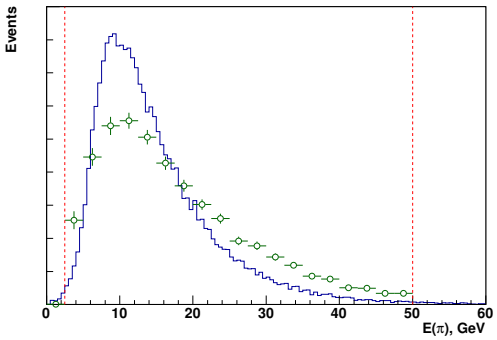

(a) Pion (π) energy distribution, before (solid blue line) and after (green circles) advanced cuts. Red lines correspond to the PID momenta cut for pions: $2.5 < E(\pi) < 50\ GeV$.

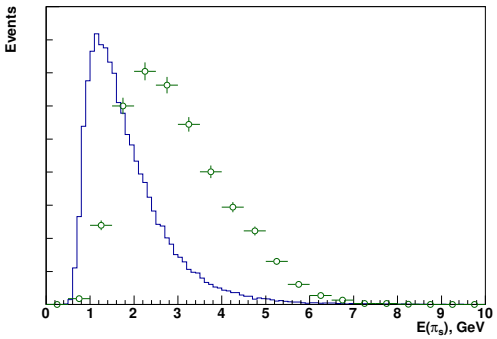

(b) Slow pion (π_s) energy distribution, before (solid blue line) and after (green circles) advanced cuts.

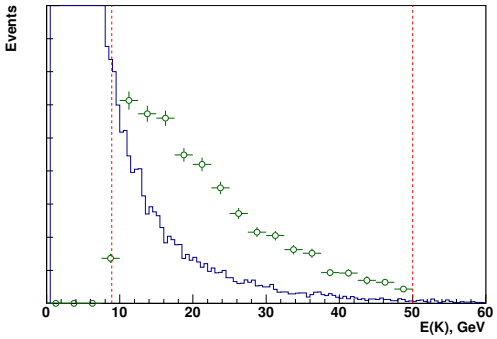

(c) Kaon (K) energy distribution, before (solid blue line) and after (green circles) advanced cuts. Red lines coresond to the PID momenta cut for kaons: $2.5 < E(K) < 50\ GeV$.

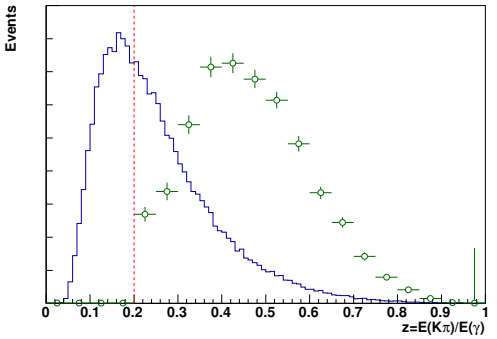

(d) Energy fraction $z = E(K\pi)/E_\gamma$ distribution of the $K\pi$ system. The red line corresponds to the cut: $z > 0.2$

Figure 4.5: Distribution of $cos(\Theta_K)$ in the D^0 rest frame for background (solid blue line) $K\pi$ combinations, D^0 signal (green circles) and acceptance corrected D^0 signal from the year 2004 (red boxes).

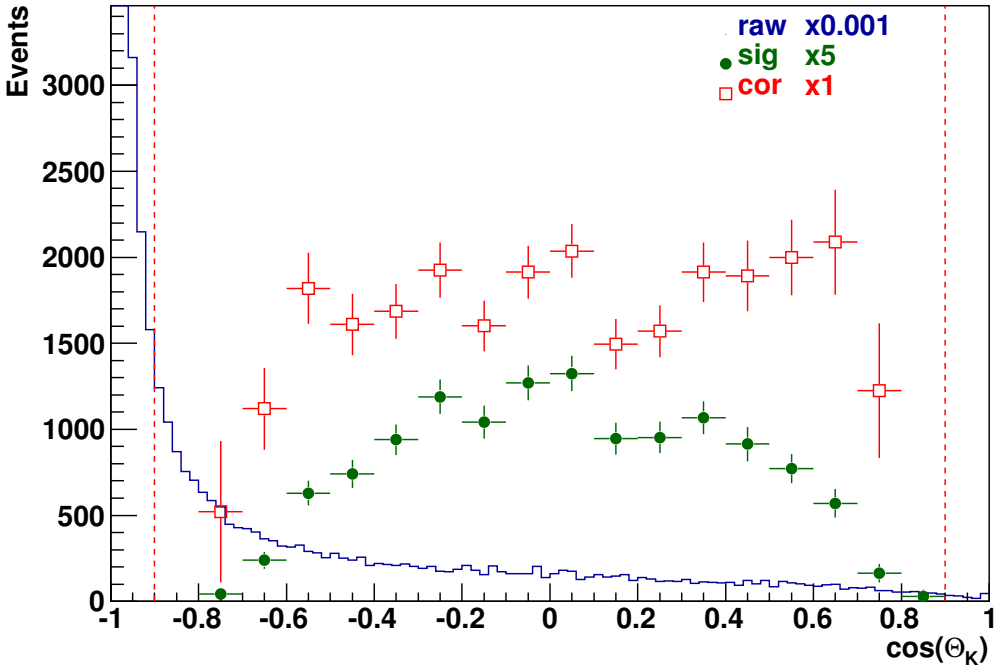

Figure 4.6: Invariant $M(K\pi)$ mass spectra within a window of $\pm 700\ MeV$ around the nominal D^0 mass. For D^0 and D^* event samples before and after background subtraction.

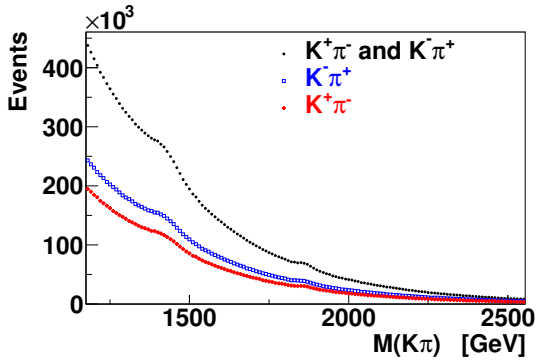

(a) D^0 sample

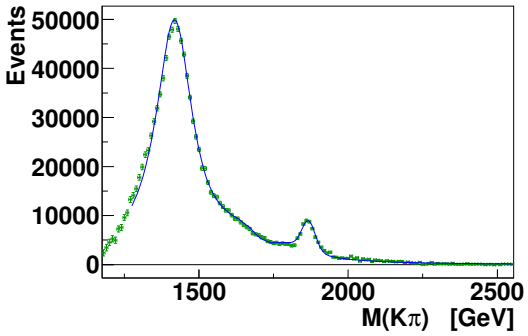

(b) D^0 sample after subtraction of exponential background

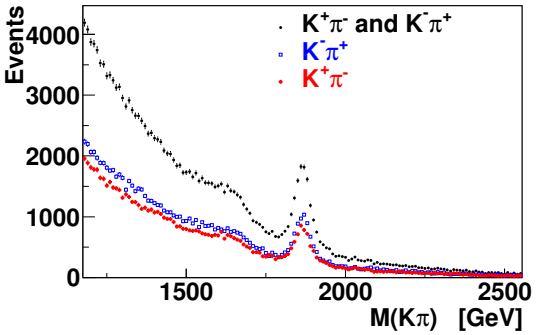

(c) D^* sample

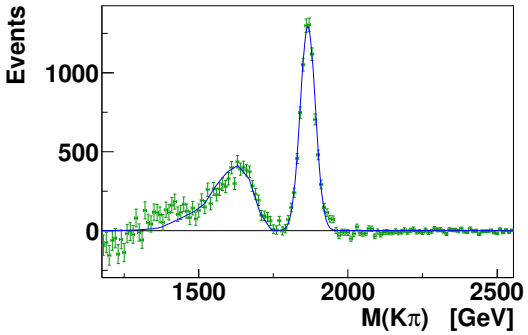

(d) D^* sample after subtraction of background

4.1.2 Method of signal extraction

In order to obtain the dependence of the D-signal and of background events or of the neighbouring $K_2^*(1430)^0$ resonance on measured kinematical parameters of the event (like transverse momentum and energy of the D-meson) the following procedure has been applied.

For each kinematical bin the invariant $K\pi$ mass spectrum is collected and the number of signal, background or $K_2^*(1430)^0$ events is obtained by the same kind of fit described above in order to describe the 2-body-decay signal, the 3-body decay peak, the $K_2^*(1430)^0$ and the background.

This method allows a control of the results by eye. As an example, where the original fit had problems and at the same time an interesting physics scenario had been revealed, Figure 4.7 shows a sequence of mass spectra for bins of the scaling variable z in case of the untagged D^0 sample. The fit assumed an exponential background, 2 resonances ($K_2^*(1430)^0$ and $D^0 \to K\pi$) and the 3-body decay peak. At high z the appearance of a - presumed-kaon resonance below the D^0 peak confused the fit so much that the fit result for the D^0 signal did not converge.

One may suspect that this resonance is the relatively narrow $K_3^*(1780)$ after having seen the dominance of the $K^*(890)$ and the $K_2^*(1430)^0$ at lower masses, owing to their comparatively narrow width. This resonance apparently follows the trend of the $K_2^*(1430)^0$ resonance being produced at larger values of z than the D^0, see next section.

As a consequence, the assumption of an additional resonance, $K_3^*(1780)$, had been introduced to the fit.

The second way of signal extraction is the standard method of side bin subtraction. This method had been applied first, but the fitting method was later on preferred, since applying the side bin subtraction to the $K_2^*(1430)^0$ signal led to problems, caused by the limited mass window of $\pm 700\ MeV$ around the D^0 mass, with the lower edge just below the $K_2^*(1430)^0$ resonance. However, the method of signal fitting in mass spectra for kinematical bins does not work for some of the potential variables, for instance, the transverse energy E_T or fractional gluon momentum x_g. Obviously, bins of transverse energy distort the invariant mass spectra so strongly, that the shape of the background is difficult to describe. Therefore, for this variable the sidebin subtraction was preferred. At the same time, the sidebin subtraction method for the other variables served as an internal cross check for the results obtained with the other, the signal-fitting method.

In the sidebin subtraction method three sets of events are selected where a $K\pi$ combination falls into one of 3 narrow $K\pi$ mass windows: one window containing the $D^0 \to K\pi$ signal plus background. This window is 100 MeV wide and centered at the nominal mass of the D^0 meson. The two sidebin windows contain only background, are 50 MeV wide and centered at 100 MeV above or below the nominal D^0 mass. Thus three independent event distributions of the $K\pi$ system are obtained as a function of any of the chosen kinematical parameters, like the transverse momentum or z variable of the $K\pi$ system. The two distributions observed in the sidebins are subtracted from the distribution of the central window. The basic assumption to justify this background subtraction method is that the

distribution of background events under the signal peak are, on the average, approximately the same as the distributions in the two side bins. In order to test this assumption, the background distributions in the two sidebins left and right of the signal have been compared. In all cases the distribution in the 2 sidebins agree so well that an interpolation to the central bin appears justified.

It is usual to assume that the number of background events in the central bin comprising the signal peak is equal to the sum of the two half-size side bins, i.e. that the background in this reduced mass range is approximately linear. However, it turned out that in case of the D^0-*sample* where the background is very high and the signal is the small difference between 2 large numbers, the linear interpolation is not good enough and the procedure had to be refined. The best estimate of the number of background events in the window around the D^0 - mass was obtained on the basis of the background parameters determined by the fit of the invariant $(K\pi)$ mass spectrum (integrated over all kinematic variables) and the total number of background events in the two side bins was correspondingly rescaled. Since about 5 percent of the signal is outside of the signal window, the value of the signal obtained by sidebin subtraction is expected to be correspondingly lower than the value obtained with the signal fitting method.

Appendix C contains more details on the signal extraction methods and comparison between the two methods.

4.1.3 Kinematical distributions before acceptance correction

The goal of Figure 4.8 displaying the (not acceptance-corrected) distributions of events as a function of accessible and relevant kinematical parameters, for the D^* and the (untagged) D^0- sample, is to compare the distributions of the $K\pi$ -system for the D^0, the $K_2^*(1430)^0$ and the background under the D^0, in order to show the - in some cases remarkable- differences. The reason why acceptance- uncorrected distributions serve for this comparison is that only for $D^* \to D^0\pi \to K\pi\pi$ signal events and only for a fraction of events (year 2004) the acceptance has been calculated.

Only the sum of both neutral charge combinations are shown in these figures.

In all of these pictures, the distribution for the D^0, the $K_2^*(1430)^0$ - signal, and for $K\pi$ - background combinations were obtained by fitting the entire mass spectra ($\pm 600 MeV$ around the D^0 at $1865 MeV$), in bins of the respective kinematical variable. The background is calculated from the fit for the mass window $1865 \pm 50 MeV$ for the case of the D^* sample.

In addition, the D^0 distributions were determined using the sidebin subtraction method. For the D^* sample a perfect agreement was found everywhere with the results of the fitting method. For the untagged D^0 sample disagreements beyond the statistical error were observed, for instance at low values of z or low $K\pi$ energy E. The explanation has been found in strongly varying background shapes, with additional broad resonances emerging below the $K_2^*(1430)^0$. The corresponding data points for D^0 and $K_2^*(1430)^0$ have been omitted, since obviously, for both, the fitting and sidebin subtraction methods, a larger invariant mass window and a more complex background description would have

been needed.

The reference system for the variables has been the photon nucleon reference system, with the nucleon at rest, unless stated otherwise. The characteristics of the virtual photon for the data samples used are displayed in Figure 4.8(a)-Figure 4.8(c).

The average values of the Q^2 and of x_{Bj} extracted from these distributions are 0.6 GeV^2 and 0.004, for the D^* events. Some perhaps interesting differences between the signal and background events can be seen at large values of Q^2 and of x_{BJ}.

As a function of the virtual photon energy ν (c) the distribution for the various $K\pi$ -systems display significantly different behaviour: The $K_2^*(1430)^0$ distribution peaks at lower values than that of D^0, the background at somewhat higher values.

The distributions for the D meson as a function of the squared transverse momentum p_T^2 show an almost single-exponential decrease and are significantly different from the case of background and $K_2^*(1430)^0$. From a fit of an exponential function (up to $p_T^2 = 2GeV^2$) the following slopes have been obtained: $-0.8 \pm 0.1/(GeV/c)^2$ for the D^*, $-1.0 \pm 0.1/(GeV/c)^2$ for the D^0 signal, $-2.0 \pm 0.1/(GeV/c)^2$ for the $K_2^*(1430)^0$ signal and $-1.7 \pm 0.1/(GeV/c)^2$ for the background events.

The distributions in the scaling variables $z = E_{K\pi}/E_\gamma$ show significant differences, too. The background is concentrated at smaller values of z than the D^0 signal. Even more remarkable, the distributions of the $K_2^*(1430)^0$ are peaked at significantly higher values of z than the D^0.

4.1.4 Acceptance

The acceptance has been calculated only for the D^* sample and only for the year 2004.

The overall acceptance for the D^* meson production by muons is divided into 2 parts:

A) The inclusive muon-event acceptance $A_\mu(x, y)$ where y is the energy of the virtual photon divided by the incoming muon energy, $y = \nu/E(\mu)$, and $x = x_{Bj}$.

B) The acceptance $A_D(x, y)$ or $A_D(E_D, p_\perp)$ for detecting, in addition, a D^* meson decay into $K\pi\pi$, as a function of x and y or of the D^0 (not D^*) energy E_D and transverse momentum $p_\perp$ in the laboratory system, or 1-dimensional acceptances $A_D(X)$ for the D^* meson, functions of the 4 kinematical variables to be considered (X= photon energy ν, D meson energy E_D, D meson transverse momentum squared p_T^2, and fractional momentum $z_D = E_D/E_\gamma$).

Moreover, the conditional acceptance $A_D^{had}(E_D, p_\perp)$, calculated only for the hadronic part of the event, i.e. after a primary vertex with an incoming and scattered muon has been reconstructed, has been considered and will be shown.

The acceptance was calculated by a complete Monte-Carlo simulation for the detector configuration in the year 2004.

Events were generated using the AROMA generator version 2.24 [31]. This program assumes that the dominant underlying mechanism for D^* production is photon-gluon fusion into $c\bar{c}$. Standard fragmentation (Peterson) functions were applied and parton showers, i.e. NLO processes, were switched on. The charm quark mass was set to 1.35 GeV. If a D^* was produced, its decay, either $D^{*+} \to D^0\pi^+ \to K^-\pi^+\pi^+$ or $D^{*-} \to \overline{D^0}\pi^- \to K^+\pi^-\pi^-$, (but

not both at the same time) was forced to be 100% for the acceptance calculation involving the hadronic part of the event, i.e, the reconstruction of the decay products of the D^*. The distributions obtained from this event generator are, at the same time considered to be the theoretical prediction. The same trigger conditions and the same data selection criteria as applied for real data were imposed and the scattered muon and hadrons were tracked through the spectrometer and particle identification was simulated, all like for the real data.

The inclusive muon acceptance $A_\mu(x, y)$ has been determined before any requirements concerning associate hadrons were imposed - apart, of course, for those implied by some of the triggers. (The calorimeter trigger, for instance, is based on hadronic energy). In total about 10M events were generated with the $D^{*+} \to D^0\pi^+ \to K^-\pi^+\pi^+$ decay and 10M events with the $D^{*-} \to \overline{D^0}\pi^- \to K^+\pi^-\pi^-$ decay.

The acceptances A_μ, A_D and A_D^{had} were calculated as a function of the reconstructed values of the kinematical variables. This definition implies that it can be bigger than one and it accounts for migration of events into other kinematical bins due to detector resolution effects.

Figure 4.9 shows a) the number of generated Monte-Carlo (AROMA) events, b) the inclusive muon acceptance $A_\mu(x, y)$, both in bins of x and y. In the relevant kinematical region the inclusive acceptance $A_\mu(x, y)$ [1] is fairly homogeneous and between 50 and 80 percent. Figure 4.9 c) displays the overall acceptance $A_D(x, y)$ to detect a muon vertex and the searched-for D* decay and e) the conditional hadron acceptance $A_D^{had}(x, y)$.

In Figure 4.10 the generated event distribution and acceptances are shown, like for the previous figure for D^0 and $\overline{D^0}$- mesons mixed, now as a function of the laboratory energy E_D and transverse momentum $p_\perp$ of the D with respect to the incoming muon beam [2]. Again, in addition to $A_D(E, p_\perp)$, the conditional, only hadron-related, acceptance $A_D^{had}(E, p_\perp)$ is shown in c).

In Figure 4.11 the acceptance, i.e. the ratio of reconstructed over generated events, as a function of laboratory energy and $p_\perp$ is shown in units of percent for the D^* tagged sample (D^{*+} and D^{*-} mixed together).

These plots and the table illustrate the acceptance of the spectrometer for D^* detection. The upper spectrometer acceptance angle of 80 $mrad$ (until the year 2004; in 2006 this angle was almost doubled) can be seen at low energy and large $p_\perp$. It is seen that, mainly due to the particle identification, the energy range of D^0 mesons from the D^* decay is limited to 20 to 80 GeV. Therefore, the final, 1-dimensional acceptances for the D^* mesons, as functions of the chosen variables (ν, E_D, p_T^2, and z_D) will be limited to this range of D

[1] To remind, here all COMPASS triggers (see section 2.2) were used for the accepance calculation. The trigger dependence of the muon acceptance $A_\mu(x, y)$ is presented in Appendix D.

[2] To display the spectrometer acceptance, $p_\perp$ calculated in the spectrometer reference system is more suited than the transverse momentum with respect to the virtual photon direction used to display physics properties. The 1-dimensional acceptance corrected distributions rather use the standard reference system, where the photon direction defines the z axis. To distinguish between the different reference systems used, different subscripts are used for the transverse momenta: $p_\perp$ wrt the muon beam and p_T wrt to the virtual photon direction

meson energies, i.e. they are calculated only for those events (on the generator level, before acceptance and reconstruction) where one of the D^* mesons decayed into $K\pi\pi$ and the D^0 energy was within the above range of 20 to 80 GeV in the laboratory. This corresponds to energies of 22 to 86 GeV for the D^*.

In all cases, only the final acceptances $A_D(X)$ are shown. The D^* acceptance had been determined in 3 steps in order to understand the separate contributions of tracking and particle identification to the final D meson acceptance: Step 1) where no particle identification is required at all, step 2) where only the K and π momentum cuts are imposed, as required by particle identification using the RICH detector. step 3) where the particle identification using all the RICH information is switched on for determining the final acceptance A_D. The decrease of the acceptance, going from 1 to 3 is not large: This is illustrated by the total number of D^* mesons accepted and reconstructed after the steps 1 to 3: $2.8 \cdot 10^6$ generated D^* events with a complete inclusive event topology - i.e. after the cuts relevant to select an incoming and outgoing muon from a vertex within one of the target cell fiducial volumes. $4.4 \cdot 10^5$ reconstructed events after step 1, $3.5 \cdot 10^5$ after step 2, $2.8 \cdot 10^5$ after step 3. (Similar reduction rates have been observed for the real data analysis from step 1 to 3. This demonstrates the high efficiency of the RICH detector setup and analysis procedures and the good match between RICH and spectrometer acceptance for this kind of physics processes.

The one-dimensional acceptance functions are shown in Figure 4.12, separately for the D^0 and $\overline{D^0}$, as a function of transverse momentum p_T^2, D meson energy E_D, energy of the photon ν and z_D. Also the acceptance ratio for D^0 and $\overline{D^0}$ is shown in each case. From the comparison it can be concluded that within the accuracy of the Monte-Carlo simulation, the acceptances are almost equal for D^0 and $\overline{D^0}$, the acceptance for the D^0 being slightly higher than that for the $\overline{D^0}$. This observation is important, since significant differences are observed for the distributions and semi-inclusive cross sections of D^0 and $\overline{D^0}$ as a function of z_D and ν, to be shown below.

4.1.5 Integrated luminosity and total visible cross section

The number of incoming muons, potentially crossing both target cells, is determined as follows. The hits in a scintillating fibre station installed directly in front of the target are counted. The number is typically $2 \cdot 10^8$ $particles/spill$. This station has a cross section somewhat larger than that of the target. Only a fraction of these muons will actually cross both target cells, after the appropriate fiducial volume cuts.

This fraction has been determined from random trigger events using reconstructed beam muons which do not interact in the target. All beam tracks in a time window around the trigger signal of the random trigger events are reconstructed and it is checked, how many tracks hitting the fibre station also cross both target cells, after fiducial volume cuts. A further correction factor due to the reconstruction efficiency of the beam momentum station was as well determined using random trigger events. For beam tracks without interaction in the target, two momentum measurements are available in COMPASS, one in the beam momentum station, the other one in the small angle spectrometer. Comparing

both, the reconstruction efficiency of the beam momentum station was obtained to be 0.96.

The typical reduction factor including all the effects described above is 0.6.

The data acquisition and trigger dead time, the latter being different for the various parallel triggers, further reduces the effective number of muons which are counted for the luminosity. The typical reduction factor due to dead time is 0.95.

The target thickness for the runs in 2004 was determined to be $3.49 \cdot 10^{25}$ $nucleons/cm^2$. Multiplying the total flux of muons in 2004, for data taken with longitudinal target polarisation, with the target thickness a total integrated luminosity in the year 2004 of $\mathcal{L} = 0.707$ $fb^{-1}$was obtained[3].

For this same year, also the acceptance of the spectrometer was determined as described above.

The total visible cross section for the D^* mesons produced in the year 2004 is calculated on the base of the four (as function of variables ν, E, z and p_T^2) differential cross sections presented in the next subsection 4.1.6. The 0.048 nb for the production of D^* with subsequent decay $K\pi\pi$ is obtained.

Using the known branching ratio (2.6 %) of D^* to $K\pi\pi$, the observed D^* meson production cross section is 1.8 ± 0.4 nb, where the 20 % error accounts for both the statistical and estimated systematic error.

AROMA gives a cross section of 7.2 nb for charm anticharm production, for the chosen (default) charm quark mass of 1.35 GeV. Assuming 0.6 D^* mesons per event - a standard guess- and accounting for the energy cut $20 < E_D < 80$ GeV, which reduces the number of charm events by another factor of 0.6 , the corresponding AROMA cross section predicted for COMPASS is 2.6 nb. The PGF cross section for open charm production strongly depends on the charm quark mass. Taking into account that the default settings were used for the AROMA generator without any special tuning, the agreement between the measured and AROMA predicted cross sections was found to be satisfactory.

4.1.6 Semi-inclusive differential cross sections for $D^{*\pm}$ muoproduction

The uncorrected distributions, prior to acceptance corrections, were shown above for all the years of data taking, 2002 to 2006, regardless whether the signal came from a D^0 or $\overline{D^0}$ or the corresponding D* parent. In this section the semi-inclusive cross sections for D* production will be shown, for the year 2004 data only, after acceptance-correction and division by integrated luminosity and branching ratios, separately for D^{*+} and D^{*-}.

A study of the differences between the relevant distributions should provide a valuable insight into the production mechanism. In a simple LO approach, assuming photon-gluon fusion with independent fragmentation of the charm and anticharm quark as being the relevant production mechanism, no differences should be observed between D^0 and $\overline{D^0}$, provided the detector acceptance is equal for both. (Only small acceptance differences

[3]This value was cross checked with another method of integrated luminosity extraction presented in Appendix D.

have been observed, as described above). However for all processes, where the quark content of the target nucleon enters, differences may occur. If parton showers are switched on in AROMA [31], the flavour dependent quark distribution functions of the nucleon come into the play. Processes like associated production of $\overline{D^0}$ with a Λ_c will lead to a difference between kinematical distributions of D^0 and $\overline{D^0}$. So will processes where an initial quark in the nucleon absorbs the virtual photon, radiates a heavy gluon which then decays to $c\bar{c}$, or where in the course of fragmentation the $\bar{c}$ quark picks up quarks from the nucleon.

It has already been noted (see Table 4.4) that about 20 percent more $\overline{D^0}$ are observed in the detector acceptance of COMPASS than D^0.

From the quark content of the D^0 ($\rightarrow K^-\pi^+$) and the $\overline{D^0}$ ($\rightarrow K^+\pi^-$) it follows that only the latter has a valence quark in common with the target nucleon and can be produced in association with a Λ_c. Similarily, from $K_2^*(1430)^0$ ($\rightarrow K^+\pi^-$) and $K_2^*(\bar{1}430)^0$ ($\rightarrow K^-\pi^+$) only the former has a valence quark in common with the nucleon and be produced in association with a Λ. Thus the $K^+\pi^-$ combination may result, in both cases, from a valence quark and/or associated production.

Table 4.5: Semi-inclusive differential cross sections for D^{*+} and D^{*-} production as a function of γ^* energy ν.

ν [GeV]	$d\sigma/d\nu$ [nb/GeV]	
	D^{*+}	D^{*-}
28	0.000 ± 0.000	0.018 ± 0.027
36	0.006 ± 0.010	0.012 ± 0.008
44	0.009 ± 0.007	0.070 ± 0.014
52	0.052 ± 0.010	0.078 ± 0.012
60	0.083 ± 0.011	0.083 ± 0.011
68	0.087 ± 0.010	0.085 ± 0.011
76	0.089 ± 0.010	0.116 ± 0.011
84	0.069 ± 0.008	0.094 ± 0.010
92	0.080 ± 0.009	0.088 ± 0.010
100	0.068 ± 0.009	0.098 ± 0.010
108	0.072 ± 0.009	0.054 ± 0.009
116	0.044 ± 0.007	0.068 ± 0.009
124	0.040 ± 0.007	0.056 ± 0.009
132	0.039 ± 0.009	0.042 ± 0.008
140	0.022 ± 0.009	0.023 ± 0.009
$\sigma^{D^{*+}}$, $\sigma^{D^{*-}}$	0.762 ± 0.034	0.985 ± 0.046
$\sigma^{D^{*\pm}}$	1.747 ± 0.057	

In Figure 4.13 and Table 4.5-Table 4.8 the semi-inclusive differential cross sections of D^0 and $\overline{D^0}$ signal events are shown as a function of ν, E_D, p_T^2, and z_D. The total (visible) cross section for $D^{*\pm}$ and separately for D^{*+} and D^{*-} mesons is also calculated and presented in the tables, see last two rows.

The errors presented in the figures and the tables are statistical ones. Ideally the cross sections ($\sigma^{D^{*+}}$, $\sigma^{D^{*-}}$ and $\sigma^{D^{*\pm}}$) obtained from these four differential cross section distributions should be the same (the same number of events is distributed in four different

Table 4.6: Semi-inclusive differential cross sections for D^{*+} and D^{*-} production as a function of D^0 energy E_D.

E [GeV]	$d\sigma/dE$ [nb/GeV]	
	D^{*+}	D^{*-}
22.5	0.177 ± 0.028	0.245 ± 0.036
27.5	0.188 ± 0.018	0.198 ± 0.019
32.5	0.155 ± 0.013	0.171 ± 0.015
37.5	0.092 ± 0.010	0.112 ± 0.012
42.5	0.087 ± 0.009	0.106 ± 0.011
47.5	0.058 ± 0.007	0.085 ± 0.009
52.5	0.055 ± 0.006	0.057 ± 0.007
57.5	0.029 ± 0.005	0.053 ± 0.007
62.5	0.014 ± 0.004	0.030 ± 0.006
67.5	0.015 ± 0.005	0.017 ± 0.006
72.5	0.015 ± 0.010	0.019 ± 0.008
77.5	0.007 ± 0.014	0.005 ± 0.007
$\sigma^{D^{*+}}$, $\sigma^{D^{*-}}$	0.892 ± 0.044	1.098 ± 0.050
$\sigma^{D^{*\pm}}$	1.990 ± 0.066	

Table 4.7: Semi-inclusive differential cross sections for D^{*+} and D^{*-} production as a function of fractional energy z.

z	$d\sigma/dz$ [nb]	
	D^{*+}	D^{*-}
0.225	0.044 ± 0.013	0.044 ± 0.015
0.275	0.051 ± 0.014	0.069 ± 0.011
0.325	0.096 ± 0.013	0.097 ± 0.017
0.375	0.117 ± 0.013	0.138 ± 0.014
0.425	0.140 ± 0.013	0.136 ± 0.013
0.475	0.136 ± 0.012	0.120 ± 0.012
0.525	0.088 ± 0.010	0.129 ± 0.011
0.575	0.072 ± 0.008	0.103 ± 0.011
0.625	0.040 ± 0.006	0.076 ± 0.009
0.675	0.020 ± 0.005	0.055 ± 0.008
0.725	0.010 ± 0.003	0.025 ± 0.005
0.775	0.004 ± 0.003	0.012 ± 0.004
$\sigma^{D^{*+}}$, $\sigma^{D^{*-}}$	0.820 ± 0.035	1.008 ± 0.040
$\sigma^{D^{*\pm}}$	1.827 ± 0.053	

ways):

$$\sigma_{\nu}^{D^{*+}} = \sigma_{E_D}^{D^{*+}} = \sigma_{p_T^2}^{D^{*+}} = \sigma_{z}^{D^{*+}}$$
$$\sigma_{\nu}^{D^{*-}} = \sigma_{E_D}^{D^{*-}} = \sigma_{p_T^2}^{D^{*-}} = \sigma_{z}^{D^{*-}}$$
$$\sigma_{\nu}^{D^{*\pm}} = \sigma_{E_D}^{D^{*\pm}} = \sigma_{p_T^2}^{D^{*\pm}} = \sigma_{z}^{D^{*\pm}}$$

The observed differences (which are beyond of any statistical fluctuations) are due to the systematic errors related to the applied procedure of the cross section extraction. The

Table 4.8: Semi-inclusive differential cross sections for D^{*+} and D^{*-} production as a function of squared transverse momentum p_T^2.

p_T^2 $[(\mathrm{GeV/c})^2]$	$d\sigma/dp_T^2$ $[\mathrm{nb/(GeV/c)^2}]$	
	D^{*+}	D^{*-}
0.20	0.816 ± 0.079	0.970 ± 0.096
0.41	0.503 ± 0.058	0.779 ± 0.072
0.65	0.381 ± 0.047	0.558 ± 0.055
0.93	0.369 ± 0.039	0.352 ± 0.038
1.25	0.201 ± 0.027	0.241 ± 0.028
1.62	0.165 ± 0.021	0.187 ± 0.023
2.05	0.087 ± 0.015	0.137 ± 0.018
2.53	0.047 ± 0.010	0.096 ± 0.015
3.09	0.057 ± 0.010	0.044 ± 0.008
3.74	0.022 ± 0.007	0.033 ± 0.008
4.47	0.009 ± 0.005	0.017 ± 0.006
5.32	0.005 ± 0.006	0.007 ± 0.005
$\sigma^{D^{*+}}$, $\sigma^{D^{*-}}$	0.743 ± 0.032	0.955 ± 0.037
$\sigma^{D^{*\pm}}$	1.698 ± 0.049	

acceptances are calculated with some errors. Also by using one-dimensional acceptances one relies to some degree on the correctness of the event generator to distribute data in the event phase space [4]. Another contribution to the systematic error is the fit function shape used for the signal extraction. It has been demonstrated (see Figure 4.7) that the $K\pi$ invariant mass distribution may change its shape in some kinematic regions. Despite the fact that the presented case was cured, one cannot exclude the existence of other (weak) dependences. An inspection of differences (in the values of the four total visible cross sections obtained from the four differential cross sections as a function of variables ν, E_D, p_T^2, and z_D) leads to the conclusion that the systematic error due to using the one-dimensional acceptances and signal extraction method is about 10 %. On top of this, the integrated luminosity error should be added (about 15 %). There is also a systematic error $< 5\%$ due to data selection cuts. The total systematic and statistical error was estimated to be ≈ 20 %.

These cross sections are compared with the predicted theoretical distributions, based on the assumption that the process is photon-gluon fusion to $c\bar{c}$ and higher order QCD radiation processes. The theoretical distributions are precisely those produced by the AROMA generator and subsequent hadronization, i.e. calculated by the program package which was used to determine the detector acceptance.

The p_T^2 and z_D distributions are also compared with results published by the EMC collaboration 20 years ago [22], based on 92 events, obtained with higher muon beam energy and a cut on $Q^2 > 3\ GeV^2$. EMC did not distinguish between $\overline{D^0}$ and D^0; within the statistical precision they found equality. So, in order to compare with the present data, their data points and errors have been divided by a factor 2.

[4] By using multidimensional acceptances this error can be reduced, but that would require much more elaborate acceptance calculation.

The general agreement between the shape of the corrected, measured distributions and corresponding AROMA predictions, with parton showers switched on, is rather good. (A normalization factor has been applied so that the total AROMA cross section is $1.8 \pm 0.4\ nb$ instead of $2.6\ nb$. To remind, the latter value is based on assumptions concerning the charm quark mass and the fraction of charm events with a D* meson in the final state.)

A closer inspection of the plots reveal some interesting features. The distribution of D^0 and $\overline{D^0}$ as a function of ν shows that $\overline{D^0}$ is systematically higher than D^0. A striking difference is seen at threshold. The effective threshold of D^0 appears to be about 10 GeV higher than that of $\overline{D^0}$ - whereas the AROMA generator produces also somewhat more $\overline{D^0}$ than D^0, but the differences at threshold are far less pronounced.

A corresponding feature can be observed for the z_D distribution. In the large z region which is mainly fed by low ν (verified but not shown here) the number of $\overline{D^0}$ becomes significantly larger than that of D^0. Again, whereas the theoretical distributions show more $\overline{D^0}$ than D^0 as well, the size of the effect is smaller. (Below we will show asymmetries of production rates as a function of the 4 variables, making use of the full statistics of the measured data). For the remaining semi-inclusive differential cross sections, functions of E_D, and p_T^2, there are no remarkable differences in the shape of the distributions of D^0 and $\overline{D^0}$. The relative abundance of the $\overline{D^0}$ appears to be uniformly distributed, in these variables. And the agreement with the theoretical distributions appears to be very good.

Finally, Figure 4.14 shows particle-antiparticle asymmetries of the semi-inclusive cross sections:

$$A(X) = \frac{d\sigma^{D^{*+}}(X) - d\sigma^{D^{*-}}(X)}{d\sigma^{D^{*+}}(X) + d\sigma^{D^{*-}}(X)} \tag{4.4}$$

for the D* sample, and for AROMA, as a function of the same set of variables X as used in the previous two figures. Here the full statistics of the years 2002-2006 was used. It is assumed that the acceptances for the two charge combinations are equal. (As shown above, for the year 2004, they are indeed nearly equal, see Figure 4.12). As a function of ν, the asymmetry is about -0.5 at $40 GeV$. The most remarkable observation is again, with higher statistical precision that the measured asymmetry decreases more significantly for increasing z_D than the theoretical asymmetry.

Asymmetries between the production of D^0 and $\overline{D^0}$ or D^{*+} and D^{*-} have been observed in numerous earlier experiments (charm photoproduction [32], and charm production by hadrons [33, 34, 35, 36, 37, 38, 39]), but not as pronounced as in the present experiment, which covers the region from threshold up to 140 GeV of virtual photon energies.

The asymmetries observed by COMPASS support the presence of other mechanism than PGF with independent fragmentation. This observation applies in particular to the region of hard fragmentation (large z) and or low photon energy ν.

Table 4.9: D^{*+} - D^{*-} asymmetry as a function of virtual photon energy ν, D^0 energy E_D, fractional energy z and squared transverse momentum p_T^2.

$\nu \pm \Delta\nu/2$ [GeV]	$\frac{N(D^{*+})-N(D^{*-})}{N(D^{*+})+N(D^{*-})}$	$E \pm \Delta E/2$ [GeV]	$\frac{N(D^{*+})-N(D^{*-})}{N(D^{*+})+N(D^{*-})}$
28 ± 4	-0.130 ± 0.415	12.5 ± 2.5	-0.263 ± 0.333
36 ± 4	-0.610 ± 0.098	17.5 ± 2.5	-0.099 ± 0.092
44 ± 4	-0.272 ± 0.082	22.5 ± 2.5	-0.149 ± 0.051
52 ± 4	-0.207 ± 0.059	27.5 ± 2.5	-0.034 ± 0.041
60 ± 4	-0.032 ± 0.051	32.5 ± 2.5	-0.045 ± 0.039
68 ± 4	-0.174 ± 0.047	37.5 ± 2.5	-0.038 ± 0.042
76 ± 4	-0.123 ± 0.044	42.5 ± 2.5	-0.148 ± 0.043
84 ± 4	-0.078 ± 0.046	47.5 ± 2.5	-0.139 ± 0.049
92 ± 4	-0.116 ± 0.053	52.5 ± 2.5	-0.159 ± 0.050
100 ± 4	-0.109 ± 0.048	57.5 ± 2.5	-0.203 ± 0.057
108 ± 4	-0.027 ± 0.057	62.5 ± 2.5	-0.180 ± 0.080
116 ± 4	-0.108 ± 0.060	67.5 ± 2.5	-0.103 ± 0.109
124 ± 4	-0.090 ± 0.068	72.5 ± 2.5	-0.235 ± 0.185
132 ± 4	-0.018 ± 0.084	77.5 ± 2.5	$+0.074 \pm 0.231$
140 ± 4	$+0.016 \pm 0.119$	82.5 ± 2.5	$+0.593 \pm 0.604$
148 ± 4	-0.215 ± 0.420	87.5 ± 2.5	$+0.288 \pm 2.146$

$z \pm \Delta z/2$	$\frac{N(D^{*+})-N(D^{*-})}{N(D^{*+})+N(D^{*-})}$	$p_T^2 \pm \Delta p_T^2/2$ [(GeV/c)^2]	$\frac{N(D^{*+})-N(D^{*-})}{N(D^{*+})+N(D^{*-})}$
0.225 ± 0.025	-0.090 ± 0.082	0.20 ± 0.10	-0.091 ± 0.046
0.275 ± 0.025	$+0.042 \pm 0.071$	0.41 ± 0.11	-0.151 ± 0.046
0.325 ± 0.025	$+0.011 \pm 0.052$	0.65 ± 0.13	-0.108 ± 0.046
0.375 ± 0.025	-0.054 ± 0.043	0.93 ± 0.15	-0.071 ± 0.045
0.425 ± 0.025	$+0.002 \pm 0.041$	1.25 ± 0.17	-0.113 ± 0.047
0.475 ± 0.025	-0.068 ± 0.040	1.62 ± 0.20	-0.116 ± 0.045
0.525 ± 0.025	-0.137 ± 0.041	2.05 ± 0.23	-0.135 ± 0.052
0.575 ± 0.025	-0.223 ± 0.046	2.53 ± 0.26	-0.232 ± 0.059
0.625 ± 0.025	-0.193 ± 0.052	3.09 ± 0.30	-0.110 ± 0.065
0.675 ± 0.025	-0.260 ± 0.059	3.74 ± 0.34	-0.132 ± 0.076
0.725 ± 0.025	-0.479 ± 0.078	4.47 ± 0.39	-0.317 ± 0.105
0.775 ± 0.025	-0.609 ± 0.099	5.32 ± 0.45	-0.071 ± 0.167
0.825 ± 0.025	-0.939 ± 0.213	6.30 ± 0.52	$+0.181 \pm 0.327$
0.875 ± 0.025	-0.926 ± 0.419	7.41 ± 0.60	-0.509 ± 0.493

Figure 4.7: Invariant $K\pi$ mass spectra in bins of the scaling variable z, for the untagged D^0 sample. The two peaks (D^0 and $K_2^*(1430)^0$) seen at low z (and in the integrated spectrum, Figure 4.6), were fitted with a Gaussian and a Breit-Wigner intensity. The vertical red lines indicate the nominal positions of the $K_2^*(1430)^0$ and D^0. The enhanced production at large z of a broad $K\pi$ resonance around 1780 MeV requires a different parameterization (one extra Breit-Wigner peak) of the spectrum than at lower z, in order to correctly determine the intensity of the D^0 signal at 1865 MeV. The small insets demonstrate the signal behavior after the removal of the fitted exponential background.

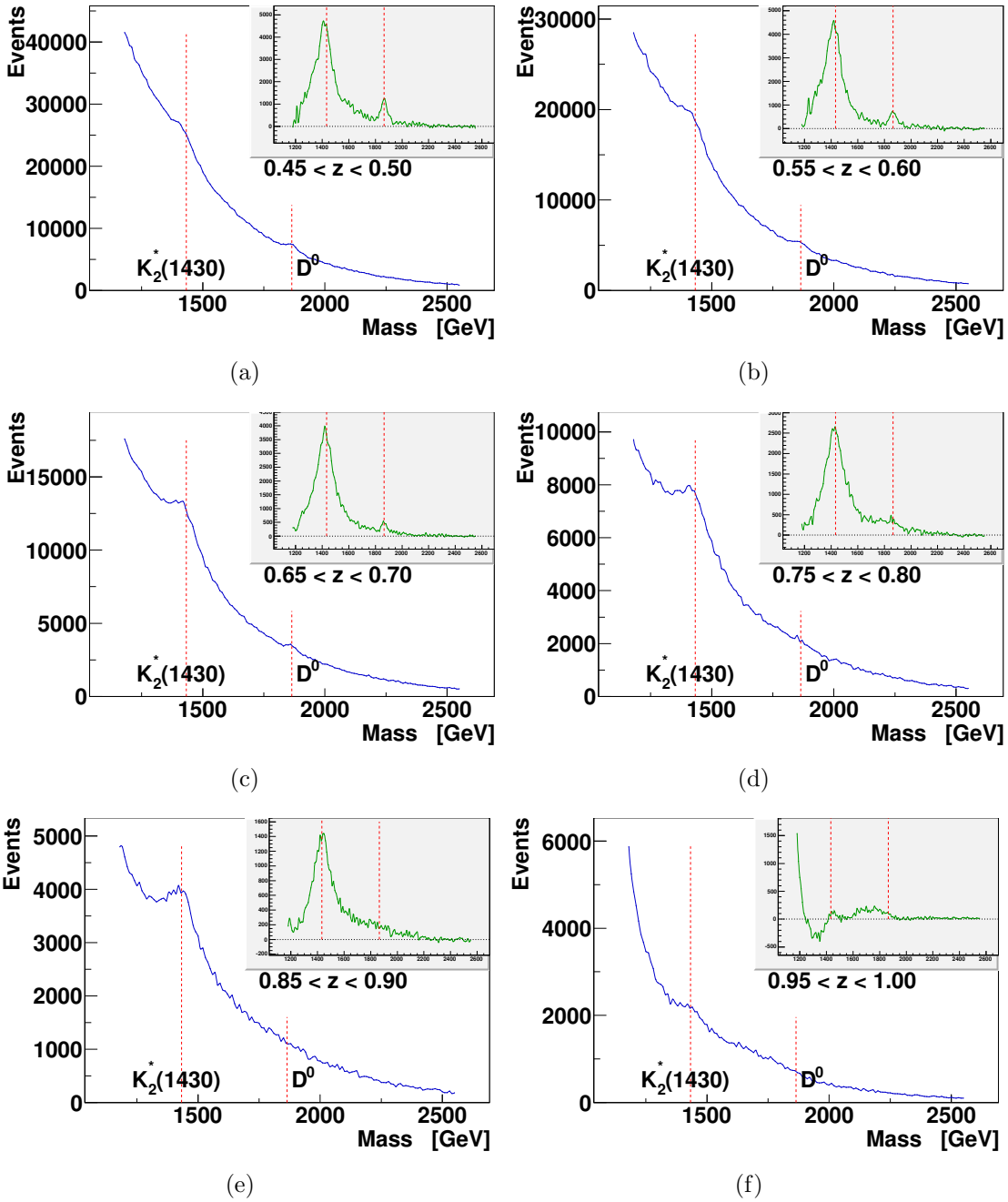

Figure 4.8: Measured kinematical distributions, before acceptance correction, of various $K\pi$ systems: D^0 signals from the untagged D^0 and the D^* sample; $K_2^*(1430)^0$ meson and background from the D^* sample; the background is taken from the $K\pi$ sidebin window centered at 1865 $\pm$ 100 MeV/c^2 with a width of 50 MeV/c^2. (Data from the years 2002 to 2006)

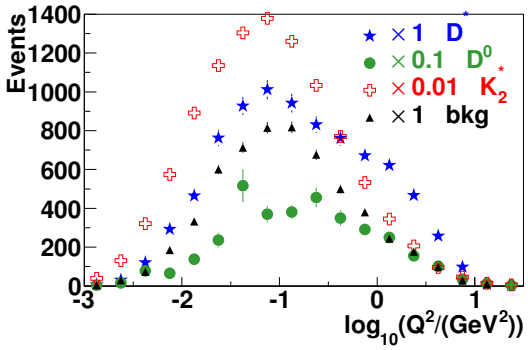

(a) Distributions as a function of $log_{10}(Q^2)$

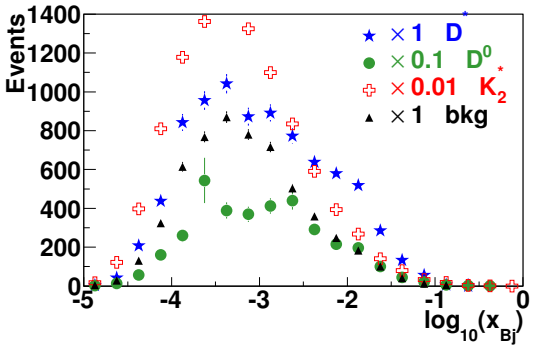

(b) Distributions as a function of $log_{10}(x_{Bj})$

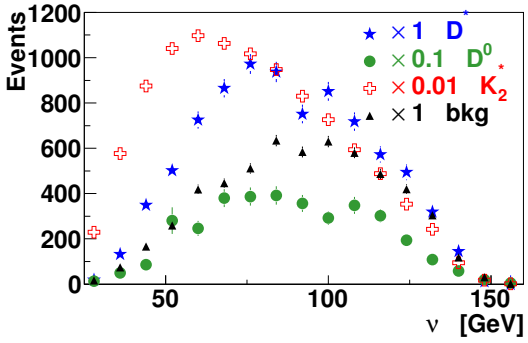

(c) Distributions as a function of ν

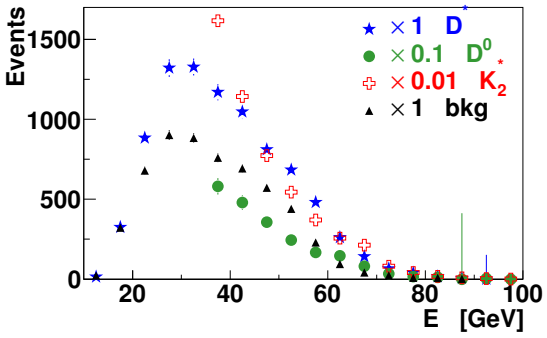

(d) Distributions as a function of $K\pi$ energy E

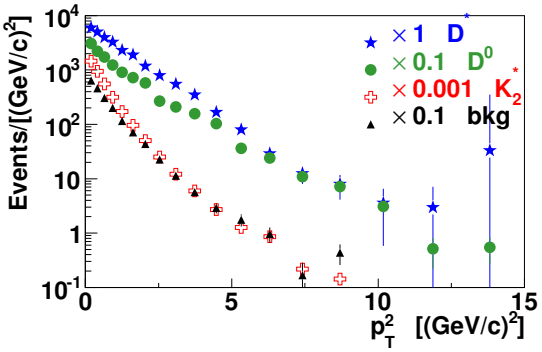

(e) Distributions as a function of squared transverse momentum p_T^2

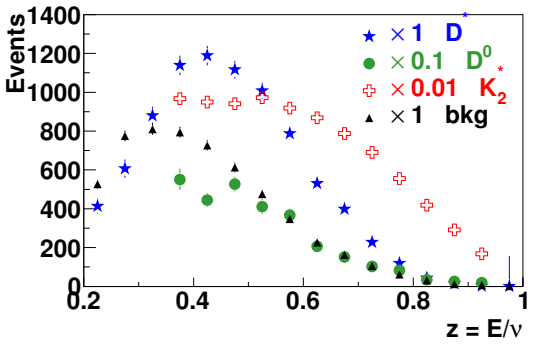

(f) Distributions as a function of energy fraction $z = E/\nu$

Figure 4.9: a) Generated events as a function of muon variables x and y. Acceptances as determined from AROMA for photon-gluon fusion to charm anticharm, as a function of the muon variables x,y: b) inclusive acceptance A_μ for detecting an event with an incoming and outgoing muon and a primary vertex, c) acceptance A_D for detecting a D^* meson, d) conditional hadron acceptance A_D^{had} after muon related cuts.

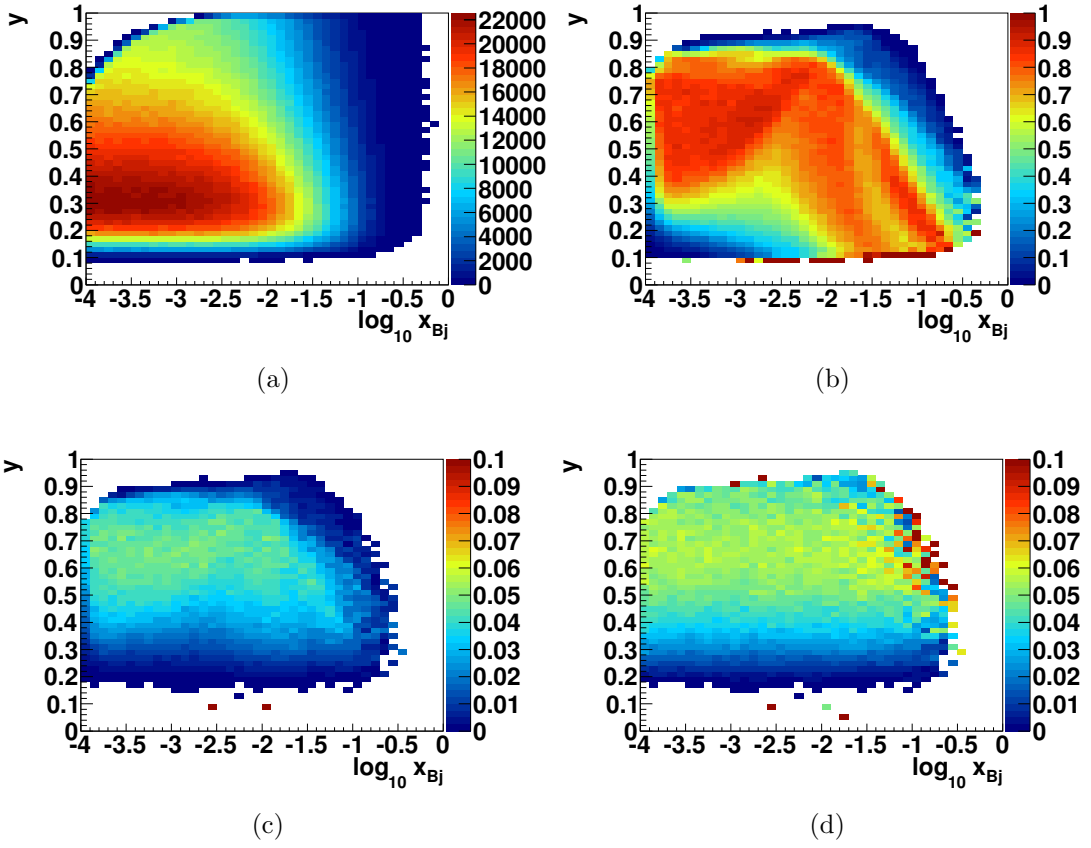

Figure 4.10: Generated distribution and acceptance of D^* mesons as a function of E_D and p_T relative to the incoming muon direction.

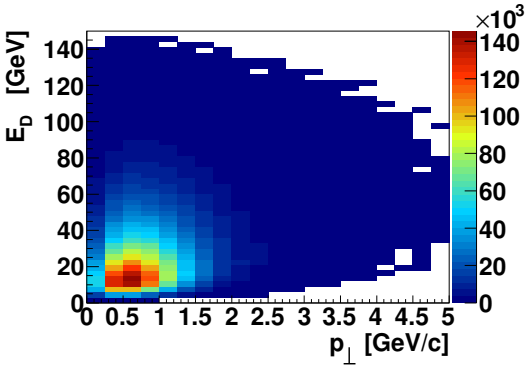

(a) Number of generated D^* events

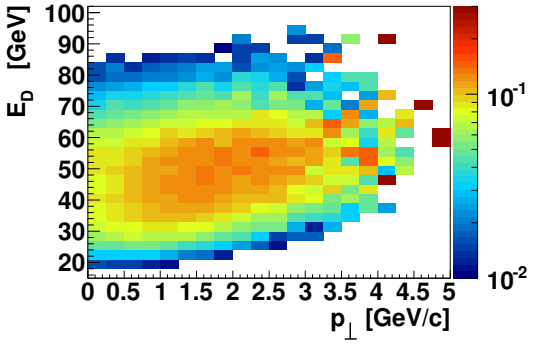

(b) Acceptance A_D

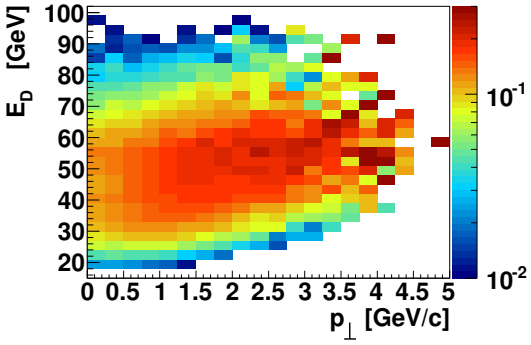

(c) Conditional acceptance A_D^{had}

Figure 4.11: Table of acceptance A_D, numbers in percent, in bins of energy E_D and transverse momentum p_T.

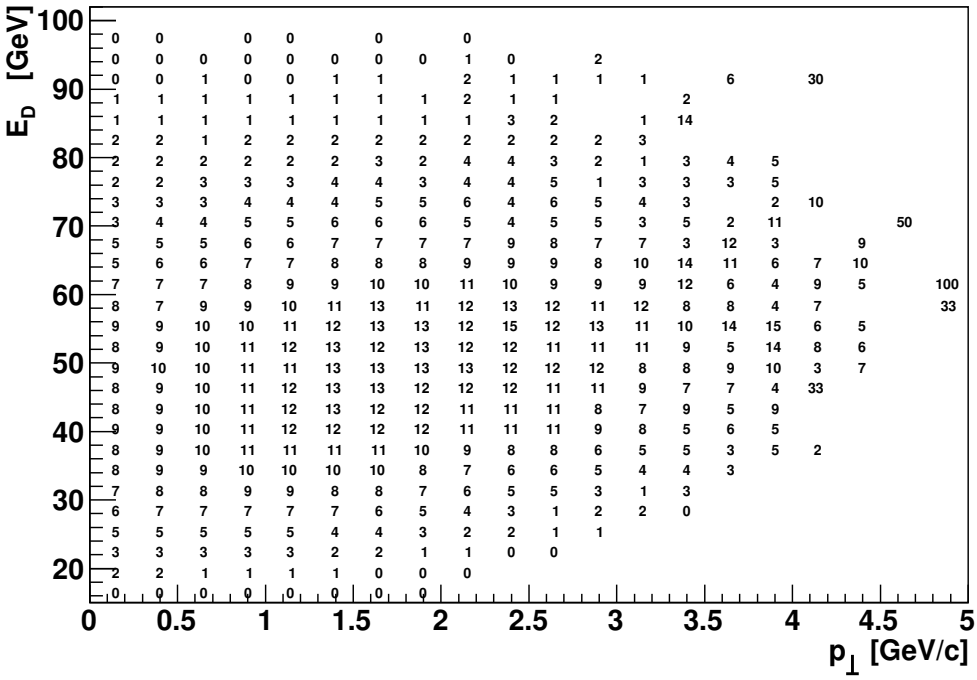

Figure 4.12: Acceptances as a function of gamma energy ν, and D^0 variables E,p_T^2,z. For all acceptance distributions, the red boxes correspond to the D^0 and the blue triangles to the $\bar{D}^0$ events. The black circles show the ratio of acceptances $A_{D^0}/A_{\bar{D}^0}$, the corresponding Y-axes of the ratios are drawn on the right hand side of the figures.

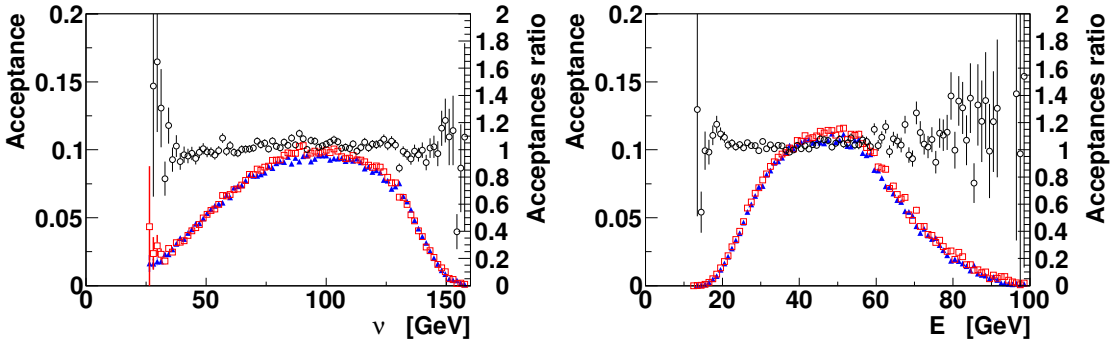

(a) Acceptances as a function of gamma energy ν

(b) Acceptances as a function of D^0 energy E

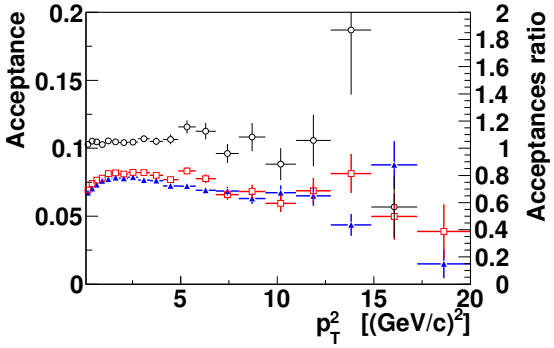

(c) Acceptances as a function of D^0 squared transverse momentum p_T^2

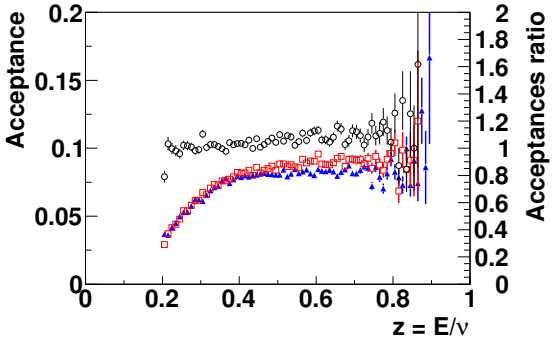

(d) Acceptances as a function of D^0 energy fraction $z = E/\nu$

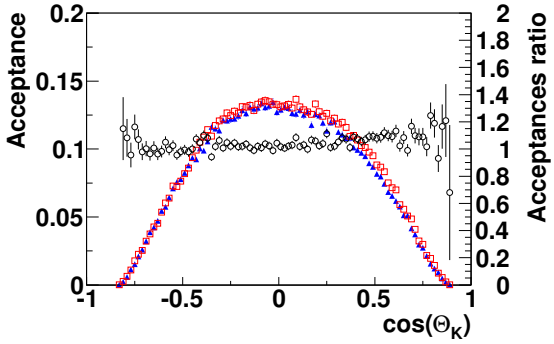

(e) Acceptances as a function of $cos(\Theta_K)$ in the D^0 rest frame

Figure 4.13: Semi-inclusive differential cross sections for D^0 and $\bar{D}^0$ production as a function of ν, E_D, p_T^2 and z_D. For all distributions, the red boxes correspond to the D^0 and the blue triangles to the $\bar{D}^0$ events. The green points are from the EMC experiment, see text. (Data from the year 2004 only, D^* sample).

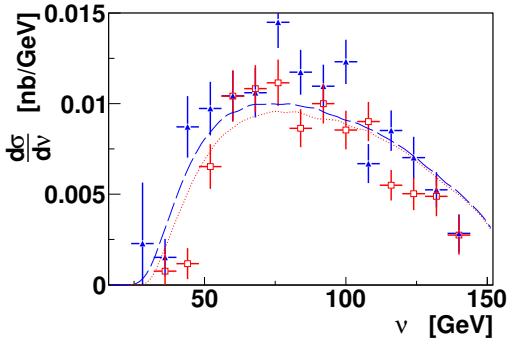

(a) ...as function of the virtual photon energy ν

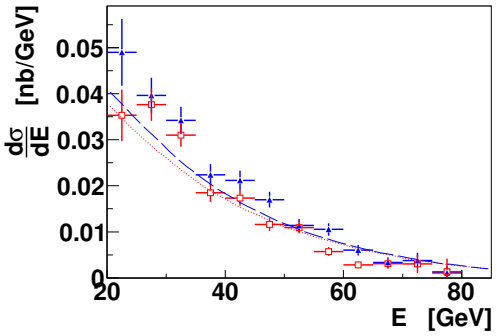

(b) ...as function of the D^0 energy E_D

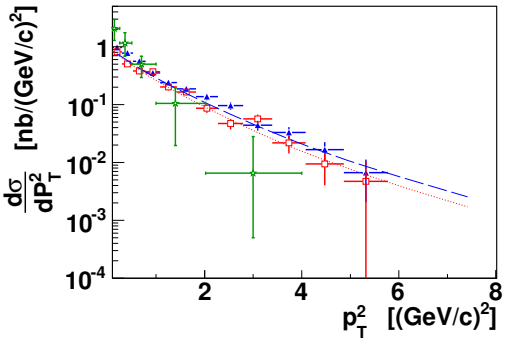

(c) ...as function of the squared transverse momentum p_T^2

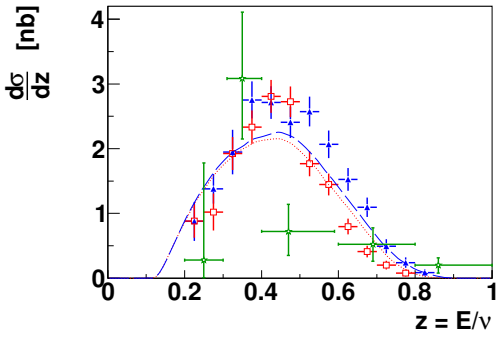

(d) ...as function of the fractional energy z_D

Figure 4.14: Measured asymmetry $\frac{dN(D^0)-dN(\bar{D^0})}{dN(D^0)+dN(\bar{D^0})}$ for D^* data (blue stars) and AROMA generator (red crosses) events as a function of the four kinematical variables. All data 2002-2006 were used.

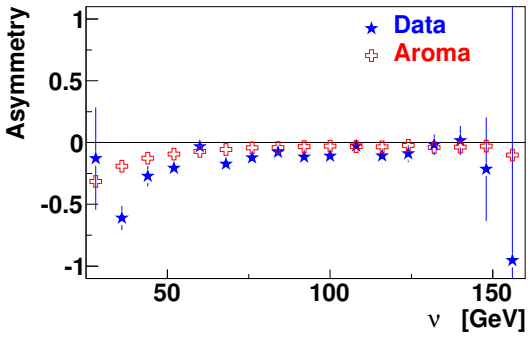

(a) Asymmetry as a function of the gamma energy ν

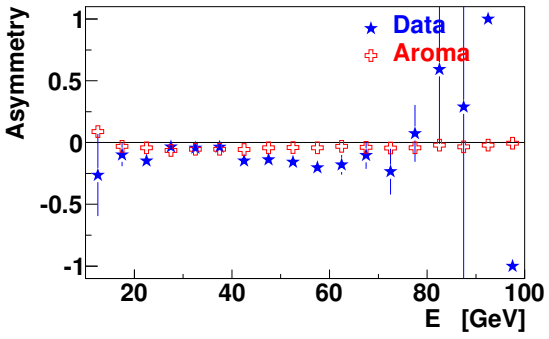

(b) Asymmetry as a function of the D energy E

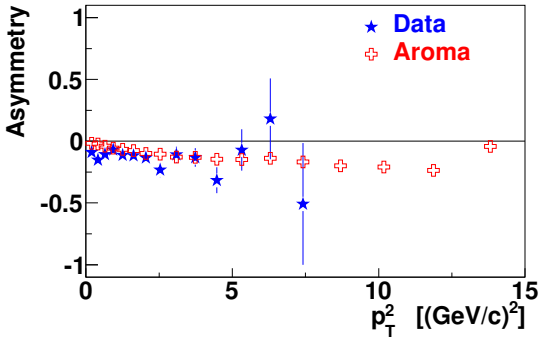

(c) Asymmetry as a function of the squared transverse momentum p_T^2

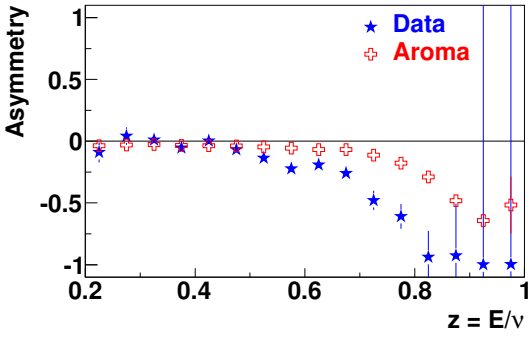

(d) Asymmetry as a function of the energy fraction $z = E/\nu$

4.1.7 More Particle-Antiparticle Asymmetries

The calculation of particle-antiparticle asymmetry defined in Equation 4.4 can be applied not only for $D^{*\pm}$-mesons, but also for D^0 and $\overline{D^0}$ mesons (without the D^* tag) and the nearby $K_2^*(1430)^0$ and $\overline{K_2^*}(1430)^0$ mesons:

$$A_{D^0}(X) = \frac{d\sigma^{D^0}(X) - d\sigma^{\overline{D^0}}(X)}{d\sigma^{D^0}(X) + d\sigma^{\overline{D^0}}(X)} \tag{4.5}$$

$$A_{K_2^*(1430)^0}(X) = \frac{d\sigma^{\overline{K_2^*}(1430)^0}(X) - d\sigma^{K_2^*(1430)^0}(X)}{d\sigma^{\overline{K_2^*}(1430)^0}(X) + d\sigma^{K_2^*(1430)^0}(X)} \tag{4.6}$$

It has been shown (see Figure 4.12) that the acceptances for detection of D^{*+} and D^{*-} mesons are almost equal (with a $\approx 10\%$ relative error). It is *assumed* that the acceptances are also equal for the other $K\pi$ systems: untagged D^0, $\overline{D^0}$ mesons; mesons $K_2^*(1430)^0$, $\overline{K_2^*}(1430)^0$; and for the background as well. This assumption is pretty much safe - all these systems pass the same cuts (for the data selection) and sit close to each other in the invariant mass distribution.

All asymmetries were calculated as a function of variable x_{Bj} and also as a function of energy and transverse momentum (E, p_T) of the $K\pi$ system. The results are presented in Table 4.10 - Table 4.15 and Figure 4.15 - Figure 4.20.

The particle-antiparticle asymmetry is seen for all the three mesons: $D^{*\pm}$, D^0 and $K_2^*(1430)^0$, with an average asymmetry approximately equal to ≈ -0.1. No strong dependence of the asymmetry is observed versus energy and transverse momentum $(E, P_\perp)$ of the $K\pi$ system. Possibly, the particle-antiparticle asymmetry shows some trend as a function of x_{Bj} variable, which can be seen on Figure 4.16, Figure 4.18 and Figure 4.20.

Table 4.10: Number of D^{*+} and D^{*-} mesons combined $N(D^{*+}, D^{*-})$ and particle-antiparticle separated $N(D^{*+})$, $N(D^{*-})$ with the corresponding asymmetry Equation 4.4 as a function of energy and transverse momentum of the $K\pi$ system.

bin	$P_T[GeV/c]$	E [GeV]	$N(D^*, \bar{D}^*)$	$N(D^*)$	$N(\bar{D}^*)$	$\frac{N(D^*)-N(\bar{D}^*)}{N(D^*)+N(\bar{D}^*)}$
1	$0.0-0.3$	$0-30$	250 ± 25	124 ± 19	125 ± 16	-0.002 ± 0.098
2	$0.0-0.3$	$30-50$	309 ± 31	156 ± 19	164 ± 21	-0.026 ± 0.089
3	$0.0-0.3$	$50-160$	92 ± 15	43 ± 9	54 ± 10	-0.106 ± 0.140
4	$0.3-0.7$	$0-30$	791 ± 47	342 ± 32	441 ± 35	-0.127 ± 0.060
5	$0.3-0.7$	$30-50$	1122 ± 54	505 ± 36	626 ± 40	-0.107 ± 0.048
6	$0.3-0.7$	$50-160$	446 ± 29	196 ± 20	251 ± 22	-0.124 ± 0.065
7	$0.7-1.0$	$0-30$	630 ± 38	271 ± 25	348 ± 28	-0.125 ± 0.060
8	$0.7-1.0$	$30-50$	988 ± 46	466 ± 34	520 ± 33	-0.055 ± 0.048
9	$0.7-1.0$	$50-160$	370 ± 25	158 ± 17	205 ± 18	-0.131 ± 0.069
10	$1.0-1.5$	$0-30$	629 ± 34	304 ± 23	321 ± 24	-0.028 ± 0.054
11	$1.0-1.5$	$30-50$	1190 ± 45	547 ± 31	664 ± 33	-0.097 ± 0.037
12	$1.0-1.5$	$50-160$	497 ± 27	199 ± 17	282 ± 20	-0.171 ± 0.054
13	$1.5-5.0$	$0-30$	268 ± 19	101 ± 13	143 ± 14	-0.172 ± 0.079
14	$1.5-5.0$	$30-50$	779 ± 32	350 ± 21	424 ± 23	-0.096 ± 0.040
15	$1.5-5.0$	$50-160$	369 ± 20	131 ± 13	226 ± 16	-0.265 ± 0.056
weighted average						-0.111 ± 0.015

Table 4.11: The same as Table 4.10 but as a function of x_{Bj}: number of D^{*+} and D^{*-} mesons combined $N(D^{*+}, D^{*-})$ and particle-antiparticle separated $N(D^{*+})$, $N(D^{*-})$ with the corresponding asymmetry Equation 4.4 as a function of x_{Bj}.

bin	$log_{10}(x_{Bj})$	$N(D^*, \bar{D}^*)$	$N(D^*)$	$N(\bar{D}^*)$	$\frac{N(D^*)-N(\bar{D}^*)}{N(D^*)+N(\bar{D}^*)}$
1	$> 10^{-1}$	7 ± 5	3 ± 4	1 ± 7	$+0.583 \pm 2.695$
2	$10^{-2} - 10^{-1}$	993 ± 40	461 ± 27	545 ± 29	-0.083 ± 0.039
3	$10^{-3} - 10^{-2}$	2867 ± 76	1253 ± 52	1633 ± 56	-0.132 ± 0.026
4	$10^{-4} - 10^{-3}$	3647 ± 93	1693 ± 64	1964 ± 68	-0.074 ± 0.025
5	$< 10^{-5}$	684 ± 39	265 ± 26	434 ± 29	-0.242 ± 0.056
weighted average					-0.110 ± 0.016

Figure 4.15: Particle-antiparticle asymmetry Equation 4.4 from Table 4.10 for $D^{*\pm}$ mesons as a function of energy and transverse momentum of the $K\pi$ system.

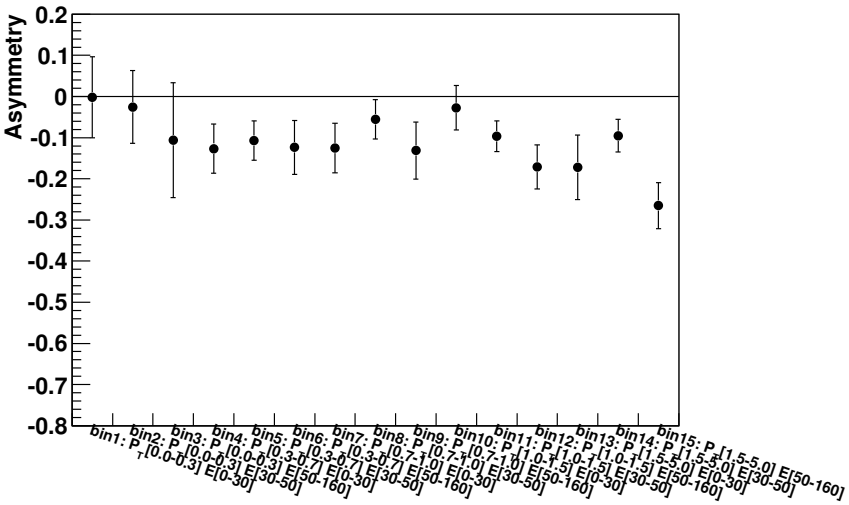

Figure 4.16: Particle-antiparticle asymmetry Equation 4.4 from Table 4.11 for $D^{*\pm}$ mesons as a function of x_{Bj}.

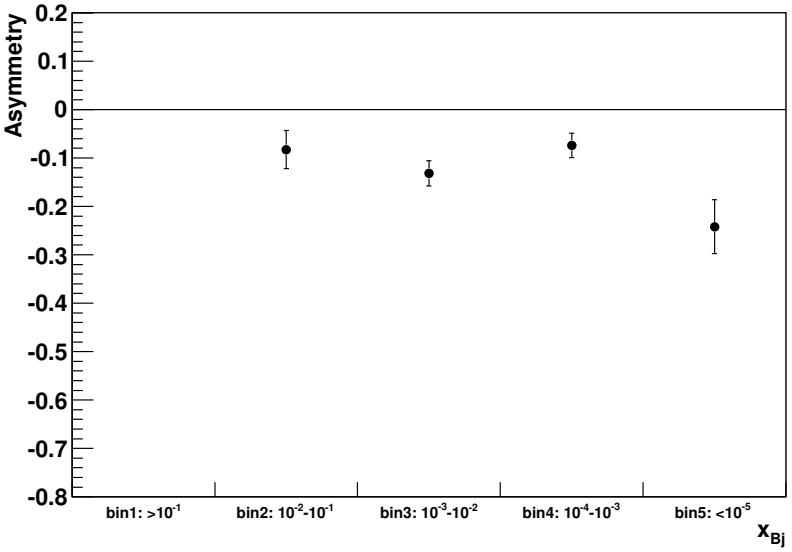

Table 4.12: The same as Table 4.10 but for the D^0 and $\overline{D^0}$ mesons without the D^* tag: number of D^0 and $\overline{D^0}$ mesons combined $N(D^0, \overline{D^0})$ and particle-antiparticle separated $N(D^0)$, $N(\overline{D^0})$ with the corresponding asymmetry Equation 4.5 as a function of energy and transverse momentum of the $K\pi$ system.

bin	$P_T[GeV/c]$	E [GeV]	$N(D^0, \bar{D^0})$	$N(D^0)$	$N(\bar{D^0})$	$\frac{N(D^0)-N(\bar{D^0})}{N(D^0)+N(\bar{D^0})}$
1	$0.0-0.3$	$0-30$	1831 ± 349	831 ± 135	686 ± 346	$+0.096 \pm 0.262$
2	$0.0-0.3$	$30-50$	1912 ± 292	1206 ± 182	682 ± 244	$+0.277 \pm 0.179$
3	$0.0-0.3$	$50-160$	737 ± 171	347 ± 103	440 ± 91	-0.119 ± 0.178
4	$0.3-0.7$	$0-30$	4271 ± 584	1249 ± 338	2575 ± 357	-0.347 ± 0.134
5	$0.3-0.7$	$30-50$	4877 ± 459	2866 ± 442	2593 ± 313	$+0.050 \pm 0.098$
6	$0.3-0.7$	$50-160$	1469 ± 284	748 ± 391	1067 ± 229	-0.176 ± 0.274
7	$0.7-1.0$	$0-30$	2902 ± 367	1358 ± 223	1545 ± 297	-0.064 ± 0.126
8	$0.7-1.0$	$30-50$	4666 ± 361	2037 ± 235	2604 ± 395	-0.122 ± 0.094
9	$0.7-1.0$	$50-160$	1863 ± 254	1071 ± 155	917 ± 155	$+0.077 \pm 0.111$
10	$1.0-1.5$	$0-30$	1706 ± 226	1099 ± 267	608 ± 121	$+0.287 \pm 0.144$
11	$1.0-1.5$	$30-50$	5839 ± 560	2178 ± 252	3277 ± 250	-0.201 ± 0.067
12	$1.0-1.5$	$50-160$	2180 ± 288	964 ± 238	1217 ± 198	-0.116 ± 0.146
13	$1.5-5.0$	$0-30$	657 ± 144	265 ± 49	445 ± 89	-0.254 ± 0.128
14	$1.5-5.0$	$30-50$	3457 ± 241	1460 ± 158	1993 ± 183	-0.154 ± 0.069
15	$1.5-5.0$	$50-160$	1558 ± 123	730 ± 98	799 ± 95	-0.045 ± 0.089
weighted average						-0.092 ± 0.029

Figure 4.17: Particle-antiparticle asymmetry Equation 4.5 from Table 4.12 for D^0 and $\overline{D^0}$ mesons without the D^* tag as a function of energy and transverse momentum of the $K\pi$ system.

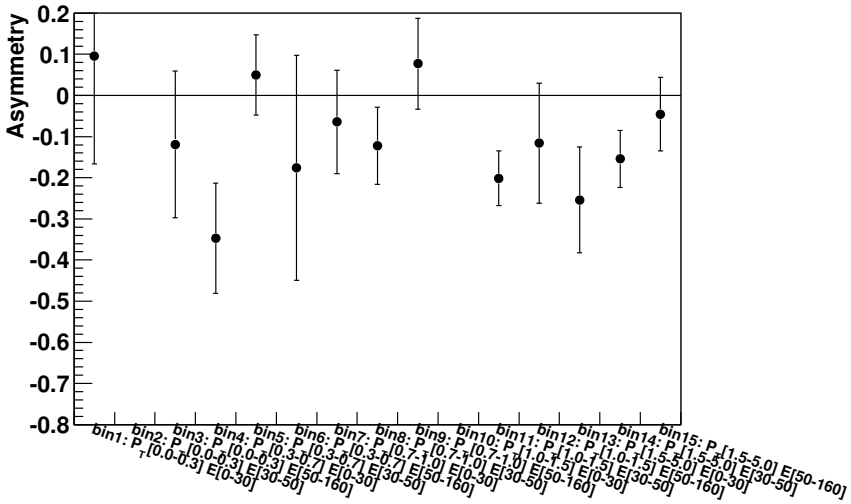

Table 4.13: The same as Table 4.12 but as a function of x_{Bj}: number of D^0 and $\overline{D^0}$ mesons combined $N(D^0, \overline{D^0})$ and particle-antiparticle separated $N(D^0)$, $N(\overline{D^0})$ with the corresponding asymmetry Equation 4.5 as a function of x_{Bj}.

bin	$log_{10}(x_{Bj})$	$N(D^0, \bar{D}^0)$	$N(D^0)$	$N(\bar{D}^0)$	$\frac{N(D^0)-N(\bar{D}^0)}{N(D^0)+N(\bar{D}^0)}$
1	$> 10^{-1}$	70 ± 24	34 ± 16	36 ± 19	-0.034 ± 0.347
2	$10^{-2} - 10^{-1}$	3558 ± 180	1517 ± 139	2041 ± 28	-0.147 ± 0.045
3	$10^{-3} - 10^{-2}$	13300 ± 755	5461 ± 473	7757 ± 577	-0.174 ± 0.055
4	$10^{-4} - 10^{-3}$	13880 ± 776	6633 ± 539	7300 ± 564	-0.048 ± 0.056
5	$< 10^{-5}$	1858 ± 397	1287 ± 222	957 ± 267	$+0.147 \pm 0.161$
weighted average					-0.117 ± 0.029

Figure 4.18: Particle-antiparticle asymmetry Equation 4.5 from Table 4.12 for D^0 and $\overline{D^0}$ mesons without the D^* tag as a function of x_{Bj}.

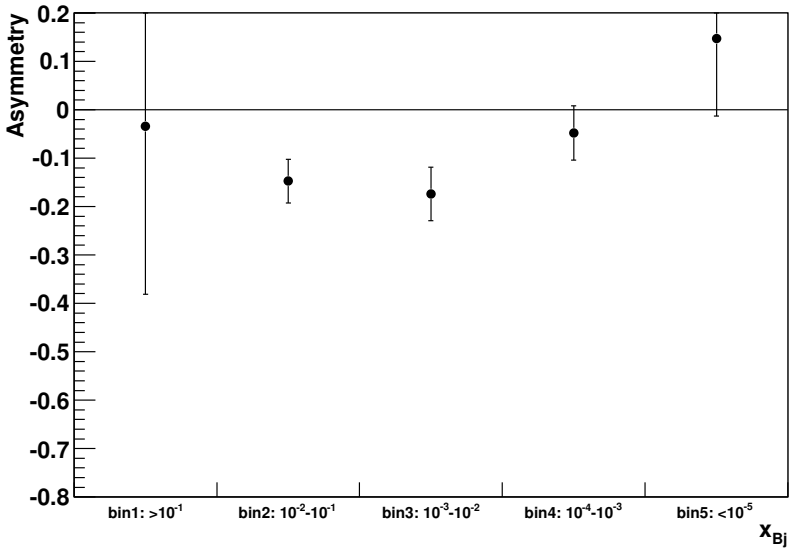

Table 4.14: Number of $K_2^*(1430)^0$ and $\overline{K_2^*}(1430)^0$ mesons combined $N(K_2^*, \overline{K_2^*})$ and particle-antiparticle separated $N(K_2^*)$, $N(\overline{K_2^*})$ with the corresponding asymmetry Equation 4.6 as a function of energy and transverse momentum of the $K\pi$ system.

bin	$P_T[GeV/c]$	E [GeV]	$N(K, \bar{K})$	$N(\bar{K})$	$N(K)$	$\frac{N(\bar{K})-N(K)}{N(\bar{K})+N(K)}$
1	$0.0-0.3$	$0-30$	80480 ± 1312	32600 ± 787	48480 ± 1040	-0.196 ± 0.016
2	$0.0-0.3$	$30-50$	88850 ± 1858	38500 ± 851	50080 ± 1771	-0.131 ± 0.020
3	$0.0-0.3$	$50-160$	15590 ± 863	7429 ± 621	8151 ± 581	-0.046 ± 0.055
4	$0.3-0.7$	$0-30$	220900 ± 3246	96410 ± 1320	125000 ± 1605	-0.129 ± 0.009
5	$0.3-0.7$	$30-50$	256200 ± 2076	110200 ± 1390	146300 ± 1545	-0.141 ± 0.008
6	$0.3-0.7$	$50-160$	76920 ± 1158	34010 ± 787	42490 ± 1578	-0.111 ± 0.022
7	$0.7-1.0$	$0-30$	98120 ± 1354	42890 ± 892	55450 ± 1018	-0.128 ± 0.014
8	$0.7-1.0$	$30-50$	131000 ± 1497	57370 ± 998	73740 ± 1114	-0.125 ± 0.011
9	$0.7-1.0$	$50-160$	38940 ± 828	17100 ± 558	21840 ± 612	-0.122 ± 0.021
10	$1.0-1.5$	$0-30$	48440 ± 998	21100 ± 652	27470 ± 755	-0.131 ± 0.020
11	$1.0-1.5$	$30-50$	80040 ± 1202	35480 ± 801	44600 ± 897	-0.114 ± 0.015
12	$1.0-1.5$	$50-160$	23350 ± 1242	10950 ± 454	12410 ± 861	-0.062 ± 0.040
13	$1.5-5.0$	$0-30$	7824 ± 771	2994 ± 444	4668 ± 312	-0.218 ± 0.077
14	$1.5-5.0$	$30-50$	17360 ± 576	7696 ± 382	9658 ± 431	-0.113 ± 0.033
15	$1.5-5.0$	$50-160$	6674 ± 340	3229 ± 420	3462 ± 249	-0.035 ± 0.074
weighted average						-0.133 ± 0.004

Figure 4.19: Particle-antiparticle asymmetry Equation 4.6 from Table 4.14 for $K_2^*(1430)^0$ and $\overline{K_2^*}(1430)^0$ mesons as a function of energy and transverse momentum of the $K\pi$ system.

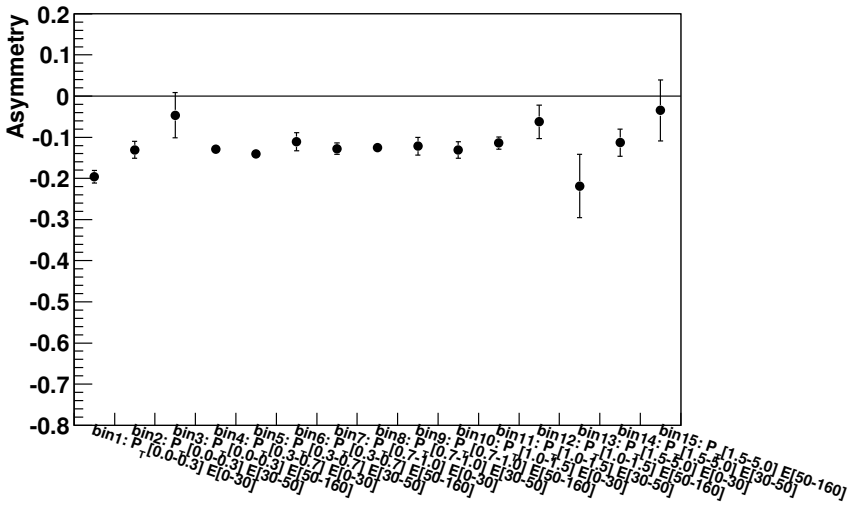

Table 4.15: The same as Table 4.14 but as a function of x_{Bj}: number of $K_2^*(1430)^0$ and $\overline{K_2^*}(1430)^0$ mesons combined $N(K_2^*, \overline{K_2^*})$ and particle-antiparticle separated $N(K_2^*)$, $N(\overline{K_2^*})$ with the corresponding asymmetry Equation 4.6 as a function of x_{Bj}.

bin	$log_{10}(x_{Bj})$	$N(K, \bar{K})$	$N(\bar{K})$	$N(K)$	$\frac{N(\bar{K})-N(K)}{N(\bar{K})+N(K)}$
1	$> 10^{-1}$	2033 ± 256	550 ± 152	1447 ± 204	-0.449 ± 0.124
2	$10^{-2} - 10^{-1}$	51560 ± 380	21030 ± 457	30680 ± 1184	-0.187 ± 0.021
3	$10^{-3} - 10^{-2}$	293000 ± 2537	127200 ± 1698	166000 ± 1886	-0.132 ± 0.009
4	$10^{-4} - 10^{-3}$	526300 ± 3340	230500 ± 2222	296100 ± 2493	-0.125 ± 0.006
5	$< 10^{-5}$	134100 ± 1552	56440 ± 1021	77810 ± 1177	-0.159 ± 0.011
weighted average					-0.135 ± 0.005

Figure 4.20: Particle-antiparticle asymmetry Equation 4.6 from Table 4.14 for $K_2^*(1430)^0$ and $\overline{K_2^*}(1430)^0$ mesons as a function of x_{Bj}.

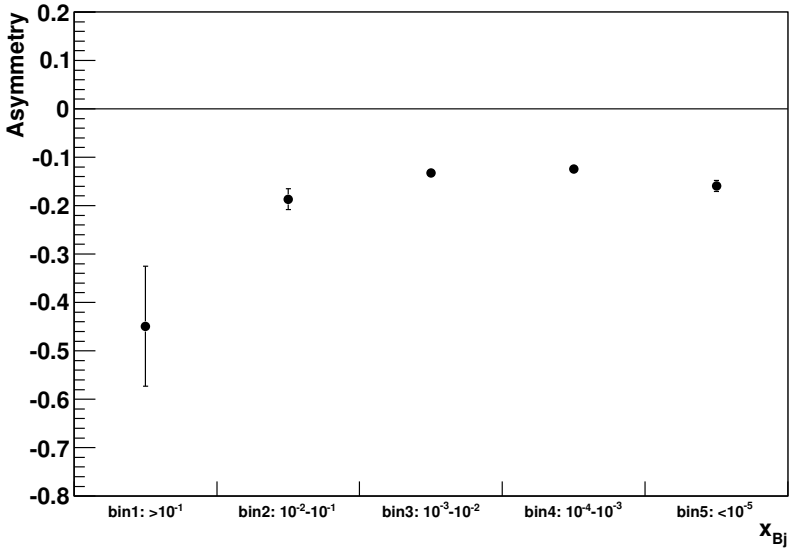

4.2 Search for Longitudinal Double Spin Asymmetries in Charm Production

4.2.1 Event Counting and Spin Asymmetries

In the following, a setup with a longitudinally polarized beam and target (i.e. polarized along or opposite to the beam direction) is considered.

The cross section of a beam and target particle interaction depends on their spin orientation. If both spins are oriented the same way in the laboratory system (along or opposite to the beam direction) the differential cross secion is $\sigma^{\overrightarrow{\Rightarrow}}$. For opposite spin projections, the differential cross secion is $\sigma^{\overleftrightarrow{\Rightarrow}}$.

The interactions between a beam and target particle are registered by detectors with some efficiency ϵ, which is called *acceptance*. The target acceptance may vary over time. It is useful to introduce a term *run*: the time interval during which acceptances and other parameters of the setup are assumed to be constant.

The number of interactions in a target, for a given target and beam polarisation, depends on the number of nuclei in the target, the detector acceptance (including reconstruction and trigger efficiency), on the integrated beam flux and elementary cross section. The number of interactions occurring in the target during a single run can be written as:

$$N = \epsilon \left[(\Phi^{\Rightarrow} n^{\rightarrow} + \Phi^{\Leftarrow} n^{\leftarrow}) \sigma^{\overrightarrow{\Rightarrow}} + (\Phi^{\Rightarrow} n^{\leftarrow} + \Phi^{\Leftarrow} n^{\rightarrow}) \sigma^{\overleftrightarrow{\Rightarrow}} \right] \tag{4.7}$$

Where:

N - number of interactions between the beam and the target in a run;

$\Phi^{\Rightarrow}$, $\Phi^{\Leftarrow}$ - integrated (for this run) flux of beam particles with spin projections along and opposite to the beam direction (positive and negative helicities);

Φ - total flux:

$$\Phi = \Phi^{\Rightarrow} + \Phi^{\Leftarrow}$$

P_b - beam polarization:

$$P_b = \frac{\Phi^{\Rightarrow} - \Phi^{\Leftarrow}}{\Phi^{\Rightarrow} + \Phi^{\Leftarrow}} = \frac{\Phi^{\Rightarrow} - \Phi^{\Leftarrow}}{\Phi}$$

$n^{\rightarrow}$, $n^{\leftarrow}$ - number of target particles with spin projections along and opposite to the beam direction;

n - total number of target particles:

$$n = n^{\rightarrow} + n^{\leftarrow}$$

f - is called *dilution* factor - the fraction of target neclei which can be polarized;

P_t - target polarization:

$$P_t = \frac{n^{\rightarrow} - n^{\leftarrow}}{f(n^{\rightarrow} + n^{\leftarrow})} = \frac{n^{\rightarrow} - n^{\leftarrow}}{fn}$$

$\sigma^{\overrightarrow{\Rightarrow}}$, $\sigma^{\overrightarrow{\Leftarrow}}$ - spin dependent cross sections, introduced earlier;

average (unpolarized) cross section

$$\langle\sigma\rangle = \left[\sigma^{\overrightarrow{\Rightarrow}} + \sigma^{\overrightarrow{\Leftarrow}}\right]/2$$

the polarized cross section difference

$$\Delta\sigma = \sigma^{\overrightarrow{\Leftarrow}} - \sigma^{\overrightarrow{\Rightarrow}}$$

cross section asymmetry

$$A = \frac{\Delta\sigma}{\sigma} = \frac{\sigma^{\overrightarrow{\Leftarrow}} - \sigma^{\overrightarrow{\Rightarrow}}}{\sigma^{\overrightarrow{\Leftarrow}} + \sigma^{\overrightarrow{\Rightarrow}}}$$

The original Equation 4.7 can be rewritten as:

$$\begin{aligned} N &= \epsilon\left[(\Phi^{\Rightarrow}n^{\rightarrow} + \Phi^{\Leftarrow}n^{\leftarrow})\sigma^{\overrightarrow{\Rightarrow}} + (\Phi^{\Rightarrow}n^{\leftarrow} + \Phi^{\Leftarrow}n^{\rightarrow})\sigma^{\overrightarrow{\Leftarrow}}\right] \\ &= \frac{\epsilon}{2}\Big[(\Phi^{\Rightarrow} + \Phi^{\Leftarrow})(n^{\rightarrow} + n^{\leftarrow})(\sigma^{\overrightarrow{\Rightarrow}} + \sigma^{\overrightarrow{\Leftarrow}}) + \\ &\quad (\Phi^{\Rightarrow} - \Phi^{\Leftarrow})(n^{\rightarrow} - n^{\leftarrow})(\sigma^{\overrightarrow{\Rightarrow}} - \sigma^{\overrightarrow{\Leftarrow}})\Big] \\ &= \epsilon\Phi\langle\sigma\rangle n\left(1 - P_b P_t f\frac{\Delta\sigma}{\sigma}\right) \end{aligned} \tag{4.8}$$

Of course, all values like acceptance, cross sections, etc. are not constant - they may vary from one event to another. If the set of variables $\vec{x} = (x_1, x_2, ...x_k)$ represents all quantities (observables) which influence the rate of events N (including time), then the full formula will become:

$$\frac{d^k N(\vec{x})}{d\vec{x}} = \epsilon(\vec{x}) \cdot \Phi(\vec{x}) \cdot \left\langle \frac{d^k\sigma}{d\vec{x}} \right\rangle \cdot n(\vec{x}) \left[1 - P_b(\vec{x})P_t(\vec{x})f(\vec{x})\frac{d^k\Delta\sigma/d\vec{x}}{d^k\sigma/d\vec{x}}\right] \tag{4.9}$$

where $d\vec{x} = \prod_{i=1}^{k} dx_i$

4.2.2 Practical Asymmetry Calculation

Figure 4.21: The principle of spin asymmetry calculation. There are two measurements (runs) with integrated beam fluxes Φ_1 and Φ_2. The beam polarizations in the runs are P_{b1} and P_{b2} accordingly. The target consists of two cells (*upstream* and *downstream*), longitudinally polarized (arrows inside the boxes) in opposite directions in every run. The measured numbers of signal events from the first run are N_u^+, N_d^- and from the second run N_u^-, N_d^+. The $\pm$ signs indicate the target cell polarization projection: "+" is along and "-" is opposite to the beam direction. The indices u, d identify the upstream or downstream target cell. Acceptances ϵ and target polarizations P_t are indicated as well.

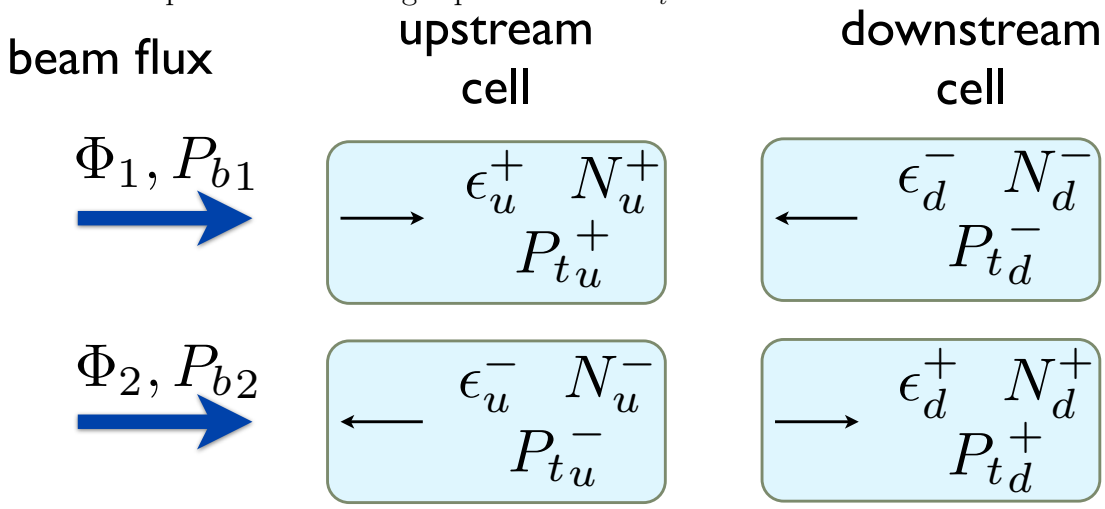

A direct method of the cross section asymmetry A determination would require a very precise knowledge of all of the variables of the Equation 4.9, which is a very difficult task. In addition, different systematic effects may significantly influence the final asymmetry value. One of the biggest contributors to the systematic error is an acceptance ϵ variation: if the event detection acceptance has changed and the experimenter did not realize that, he would assume that the difference is due to physics, which would lead to a wrong conclusion on a measured asymmetry value.

To reduce the systematic errors related to the acceptance variations, the following measurement method is applied. First of all the target material is split into two (or more) *cells* and the beam will cross all target cells in a run. The first cell (in the beam direction) is called *upstream* and the second one is *downstream*. In addition, from time to time the target is repolarized, so that the cell polarizations will swap.

An example of such measurements is illustrated on the Figure 4.21. For the four

counting rates $N^{\pm}_{ud}$, the four equations (of the type Equation 4.8) can be written:

$$\begin{cases} N^+_u = \Phi_1 \epsilon^+_u \langle\sigma\rangle n(1 - P_{b1}P^+_{tu} f\frac{\Delta\sigma}{\sigma}) \\ N^-_d = \Phi_1 \epsilon^-_d \langle\sigma\rangle n(1 - P_{b1}P^-_{td} f\frac{\Delta\sigma}{\sigma}) \\ N^-_u = \Phi_2 \epsilon^-_u \langle\sigma\rangle n(1 - P_{b2}P^-_{tu} f\frac{\Delta\sigma}{\sigma}) \\ N^+_d = \Phi_2 \epsilon^+_d \langle\sigma\rangle n(1 - P_{b2}P^+_{td} f\frac{\Delta\sigma}{\sigma}) \end{cases} \tag{4.10}$$

In this system of four equations, there are too many unknown values: two beam fluxes Φ_1 and Φ_2, four acceptances ϵ^+_u, ϵ^-_u, ϵ^+_d, ϵ^-_d, the average unpolarized cross section $\langle\sigma\rangle$, target material n and the asymmetry $\frac{\Delta\sigma}{\sigma}$ itself (which we want to extract). All factors outside of the brackets except cell acceptances can be eliminated by constructing a double ratio R_A of the event rates:

$$R_A \equiv \frac{N^-_u N^-_d}{N^+_u N^+_d} = \frac{\epsilon^-_u \epsilon^-_d}{\epsilon^+_u \epsilon^+_d} \frac{(1 - P_{b2}P^-_{tu} f\frac{\Delta\sigma}{\sigma})(1 - P_{b1}P^-_{td} f\frac{\Delta\sigma}{\sigma})}{(1 - P_{b1}P^+_{tu} f\frac{\Delta\sigma}{\sigma})(1 - P_{b2}P^+_{td} f\frac{\Delta\sigma}{\sigma})} \tag{4.11}$$

Now the assumption is made, that the ratio of cell acceptances ϵ_u/ϵ_d does not change from run to run:

$$\epsilon_{ud} \equiv \frac{\epsilon^-_u}{\epsilon^+_d} = \frac{\epsilon^+_u}{\epsilon^-_d} \tag{4.12}$$

and a single equation for the $\frac{\Delta\sigma}{\sigma}$ asymmetry calculation is obtained:

$$\frac{N^-_u N^-_d}{N^+_u N^+_d} = \frac{(1 - P_{b2}P^-_{tu} f\frac{\Delta\sigma}{\sigma})(1 - P_{b1}P^-_{td} f\frac{\Delta\sigma}{\sigma})}{(1 - P_{b1}P^+_{tu} f\frac{\Delta\sigma}{\sigma})(1 - P_{b2}P^+_{td} f\frac{\Delta\sigma}{\sigma})} \tag{4.13}$$

This quadratic equation on the cross section asymmetry $\frac{\Delta\sigma}{\sigma}$ can be (and has been for the asymmetry measurement) solved exactly. But one can derive an approximate formula for $\frac{\Delta\sigma}{\sigma}$ if a few more assumptions are made. Let us assume that

$$|P_b P_t f \frac{\Delta\sigma}{\sigma}| \ll 1 \tag{4.14}$$

In this case Equation 4.13 can be rewritten:

$$\frac{N^-_u N^-_d}{N^+_u N^+_d} \approx 1 + (P_{b1}P^+_{tu} + P_{b2}P^+_{td} - P_{b2}P^-_{tu} - P_{b1}P^-_{td}) f \frac{\Delta\sigma}{\sigma} \tag{4.15}$$

So by measuring the four event rates $N^{\pm}_{ud}$ and with the knowledge of the target dilution factor f and polarizations of the beam P_b and the target P_t the cross section asymmetry can be extracted:

$$\frac{\Delta\sigma}{\sigma} = \left(\frac{N^-_u N^-_d}{N^+_u N^+_d} - 1\right) / (P_{b1}P^+_{tu} + P_{b2}P^+_{td} - P_{b2}P^-_{tu} - P_{b1}P^-_{td}) f \tag{4.16}$$

Gamma-nucleon cross section asymmetry

So far nothing was said about the beam particle, the only used information was the polarisation P_b. For the photon-nucleon cross section asymmetry $A^{\gamma^* N \to c\bar{c}}$ calculation, the virtual photon polarization is calculated from the muon polarization (see subsection 2.1.1) by means of the depolarization factor D, see Equation 3.16 and Equation 3.15. The Equation 4.16 (and all other equations where P_b was used) should be changed accordingly:

$$A^{\gamma^* N \to X} = \left(\frac{N_u^- N_d^-}{N_u^+ N_d^+} - 1 \right) / (P_{b1} P_{t_u}^+ + P_{b2} P_{t_d}^+ - P_{b2} P_{t_u}^- - P_{b1} P_{t_d}^-) D f \tag{4.17}$$

The results presented in subsection 4.2.3 were obtained not with this approximate formula, but with an exact solution of the qudratic equation.

Double ratio for cell acceptances

In addition to the double ratio of event rates, Equation 4.11, another one can be formed, where the asymmetry terms are canceled and the cell acceptance ratio ϵ_{ud} enters (the assumptions 4.12, 4.14 were used again):

$$R_\epsilon \equiv \frac{N_u^+ N_u^-}{N_d^+ N_d^-} \approx \epsilon_{ud}^2 \tag{4.18}$$

4.2.3 Results on Spin Asymmetries

The cross section spin asymmetry $A^{\gamma^* N \to X}$ calculation is based on the same event selection which was explained in the subsection 4.1.1. To increase the statistical precision of the asymmetry extraction, all the data from 2002-2006 corresponding to the four different target cell spin configurations (see subsection 4.2.2) were summarized. The spin asymmetry was calculated for the signals coming from:

- D^0 mesons with the $D^{*\pm}$ tag;
- D^0 mesons without the $D^{*\pm}$ tag;
- $K_2^*(1430)^0$ meson;
- background.

The *background* spin asymmetry was used to check for *false* asymmetry. Assuming that asymmetry can be only due to signal, any measurement of background asymmetry not compatible with zero value would be an indication of a possible systematic effect [5].

[5] The assumption (quite usual) that the background cannot have any asymmetry is not very convincing. For example a background may be partially formed by some overlapping wide resonances, which are very difficult to take into account. However, in the present analysis all background asymmetries were compatible with zero, so there was no need of any further investigation of a background asymmetry.

Asymmetries are calculated for $K^-\pi^+$ and $K^+\pi^-$ systems combined and separately for $K^-\pi^+$ and $K^+\pi^-$ combinations. All asymmetries were calculated as a function of variable x_{Bj} and also as a function of energy and transverse momentum (E, p_T) of the $K\pi$ system (the same dependencies as for the particle-antiparticle asymmetries, see subsection 4.1.7). The results are presented in the tables Table 4.16 - Table 4.21 and figures Figure 4.22 - Figure 4.32.

All computed background asymmetres are compatible with zero, so no systematic effects are seen with the present data analysis. Also no significant spin asymmetries are observed for D^* and D^0 (without the D^* tag) mesons. This zero-compatible cross section asymmetry $A^{\gamma^* N \to c\bar{c}}$ means that from Equation 3.13 any extracted value of $\Delta G/G$ will be also compatible with zero.

The only non-zero value (3-sigma effect) of the cross section spin asymmetry is observed for the $K_2^*(1430)^0 \to K^+\pi^-$ system, see the *weighted average* value of the asymmetry $A^K(K^+\pi^-)$ in Table 4.20 and Table 4.21. Moreover, looking at Figure 4.32 one can see a possible trend in the x_{Bj} dependence of the $\overline{K_2^*}(1430)^0 \to K^-\pi^+$ asymmetry. Despite the huge number of registered $K_2^*(1430)^0$ mesons (about one million) it is difficult to study this promising asymmetry deeper.

The $K_2^*(1430)^0$ contains $d\bar{s}$ quarks (see Appendix A), and one way of interpretation of the observed $K_2^*(1430)^0$ asymmetry would be to claim that the $\bar{s}$ or d-quark is polarized at these small values of x_{Bj}.

Table 4.16: The cross section spin asymmetry $A^{D^*} = A^{\gamma^* N \to D^* X}$ for the D^*-tagged D^0 mesons. The asymmetry is calculated for $D^{*\pm}$ mesons combined (the table column $A^{D^{*\pm}}$) and separately for D^{*+} and D^{*-} mesons (the table columns $A^{D^{*+}}(K^-\pi^+\pi^+)$ and $A^{D^{*-}}(K^+\pi^-\pi^-)$). The background asymmetry (false asymmetry check) is also computed for the $K^-\pi^+\pi^+$ and $K^+\pi^-\pi^-$ systems combined and separated (the table columns A^{bkg}, $A^{bkg}(K^+\pi^-\pi^-)$, $A^{bkg}(K^+\pi^-\pi^-)$). The asymmetries are calculated as a function of energy E and transverse momentum p_T of the $K\pi$ system. The Figure 4.22 and the Figure 4.23 are graphical presentations of the table content.

bin	P_T [GeV/c]	E [GeV]	A^{D^*}	$A^{D^*}(K^-\pi^+)$	$A^{D^*}(K^+\pi^-)$	A^{bkg}	$A^{bkg}(K^-\pi^+)$	$A^{bkg}(K^+\pi^-)$
1	$0.0-0.3$	$0-30$	-0.892 ± 1.057	-1.551 ± 1.688	$+0.426 \pm 1.520$	$+0.098 \pm 0.121$	$+0.264 \pm 0.192$	$+0.102 \pm 0.168$
2	$0.0-0.3$	$30-50$	$+0.485 \pm 0.904$	$+0.791 \pm 1.339$	-0.051 ± 1.122	-0.163 ± 0.111	-0.206 ± 0.158	-0.084 ± 0.153
3	$0.0-0.3$	$50-160$	-1.153 ± 1.208	$+1.959 \pm 4.402$	-1.950 ± 2.102	$+0.064 \pm 0.195$	-0.102 ± 0.299	$+0.091 \pm 0.296$
4	$0.3-0.7$	$0-30$	-0.019 ± 0.710	-0.057 ± 1.050	$+0.584 \pm 0.966$	$+0.090 \pm 0.075$	$+0.056 \pm 0.110$	$+0.049 \pm 0.101$
5	$0.3-0.7$	$30-50$	$+0.421 \pm 0.414$	-0.029 ± 0.602	$+0.906 \pm 0.579$	$+0.028 \pm 0.063$	-0.068 ± 0.091	$+0.043 \pm 0.088$
6	$0.3-0.7$	$50-160$	$+0.057 \pm 0.492$	$+0.807 \pm 0.819$	-0.894 ± 0.729	-0.257 ± 0.123	-0.279 ± 0.185	-0.114 ± 0.179
7	$0.7-1.0$	$0-30$	$+0.295 \pm 0.691$	$+0.153 \pm 1.114$	$+0.008 \pm 1.037$	-0.182 ± 0.106	-0.121 ± 0.160	-0.254 ± 0.146
8	$0.7-1.0$	$30-50$	-0.240 ± 0.365	-0.830 ± 0.557	-0.260 ± 0.533	-0.054 ± 0.089	-0.119 ± 0.132	$+0.028 \pm 0.123$
9	$0.7-1.0$	$50-160$	$+0.823 \pm 0.533$	$+0.552 \pm 0.966$	$+2.248 \pm 0.705$	-0.037 ± 0.172	-0.153 ± 0.238	-0.146 ± 0.256
10	$1.0-1.5$	$0-30$	-0.909 ± 0.584	$+0.054 \pm 0.997$	-1.802 ± 0.843	-0.198 ± 0.153	-0.348 ± 0.232	$+0.043 \pm 0.213$
11	$1.0-1.5$	$30-50$	-0.115 ± 0.316	-0.308 ± 0.482	$+0.217 \pm 0.420$	$+0.071 \pm 0.116$	$+0.071 \pm 0.175$	$+0.056 \pm 0.161$
12	$1.0-1.5$	$50-160$	-0.422 ± 0.416	-0.607 ± 0.780	-0.188 ± 0.604	-0.132 ± 0.243	-0.315 ± 0.343	-0.269 ± 0.335
13	$1.5-5.0$	$0-30$	$+0.138 \pm 1.310$	$+0.704 \pm 3.321$	$+1.401 \pm 2.025$	$+0.088 \pm 0.436$	$+0.009 \pm 0.700$	$+0.039 \pm 0.719$
14	$1.5-5.0$	$30-50$	$+0.510 \pm 0.382$	-0.783 ± 0.622	$+1.523 \pm 0.595$	$+0.023 \pm 0.274$	$+0.138 \pm 0.424$	-0.117 ± 0.377
15	$1.5-5.0$	$50-160$	$+0.067 \pm 0.490$	$+0.283 \pm 0.959$	$+0.386 \pm 0.751$	-0.182 ± 0.449	-0.283 ± 0.599	-0.493 ± 0.607
weighted average			$+0.017 \pm 0.131$	-0.219 ± 0.213	$+0.297 \pm 0.187$	-0.026 ± 0.030	-0.071 ± 0.045	-0.011 ± 0.042

Figure 4.22: A graphical presentation of the D^* cross section asymmetry $A^{\gamma^* N \to D^* X}$ from the Table 4.16. The asymmetry of $K^-\pi^+\pi^+$ system is plotted with blue boxes, $K^+\pi^-\pi^-$ with red triangles and the combined asymmetry is plotted with filled black circles.

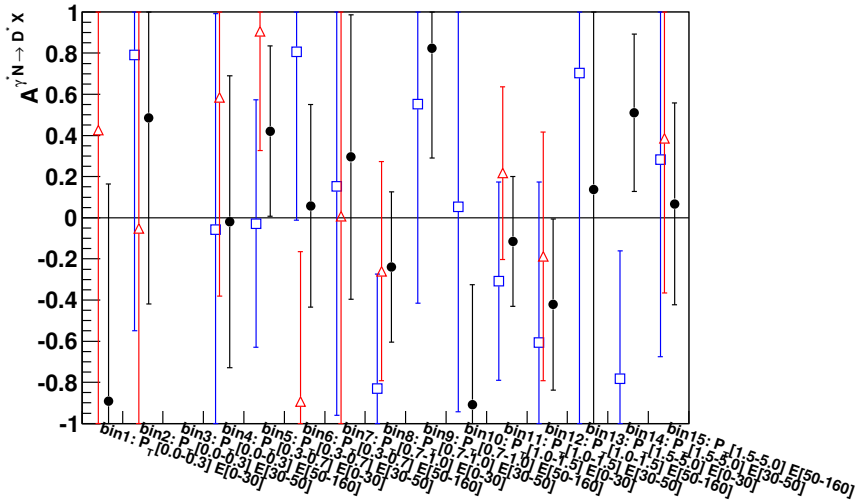

Figure 4.23: A graphical presentation of the background asymmetry A^{bkg} from the Table 4.16. The asymmetry of $K^-\pi^+\pi^+$ system is plotted with blue boxes, $K^+\pi^-\pi^-$ with red triangles and the combined asymmetry is plotted with filled black circles.

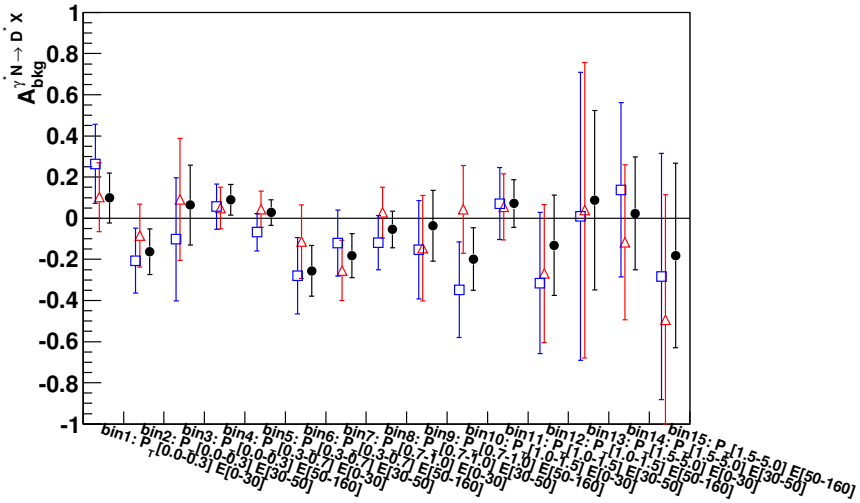

Table 4.17: The same as Table 4.16 but as a function of x_{Bj}: the cross section spin asymmetry $A^{D^*} = A^{\gamma^* N \to D^* X}$ for the D^*-tagged D^0 mesons. The asymmetry is calculated for $D^{*\pm}$ mesons combined (the table column $A^{D^{*\pm}}$) and separately for D^{*+} and D^{*-} mesons (the table columns $A^{D^{*+}}(K^-\pi^+\pi^+)$ and $A^{D^{*-}}(K^+\pi^-\pi^-)$). The background asymmetry (false asymmetry check) is also computed for the $K^-\pi^+\pi^+$ and $K^+\pi^-\pi^-$ systems combined and separated (the table columns A^{bkg}, $A^{bkg}(K^+\pi^-\pi^-)$, $A^{bkg}(K^+\pi^-\pi^-)$). The asymmetries are calculated as a function of energy x_{Bj}. The Figure 4.24 and the Figure 4.25 are graphical presentations of the table content. There are too little events in the bin 1 to extract the cross section asymmetry, see Table 4.11.

bin	$log_{10}(x_{Bj})$	A^{D^*}	$A^{D^*}(K^-\pi^+)$	$A^{D^*}(K^+\pi^-)$	A^{bkg}	$A^{bkg}(K^-\pi^+)$	$A^{bkg}(K^+\pi^-)$
1	$> 10^{-1}$	-13.400 ± 0.000	$+10.510 \pm 6.503$	-12.020 ± 0.000	$+0.305 \pm 2.425$	$+0.263 \pm 3.615$	-0.242 ± 4.012
2	$10^{-2} - 10^{-1}$	$+0.227 \pm 0.480$	$+0.406 \pm 0.765$	$+0.330 \pm 0.679$	-0.108 ± 0.163	-0.121 ± 0.256	-0.120 ± 0.227
3	$10^{-3} - 10^{-2}$	$+0.159 \pm 0.258$	-0.016 ± 0.384	$+0.304 \pm 0.340$	$+0.022 \pm 0.056$	$+0.034 \pm 0.082$	$+0.030 \pm 0.077$
4	$10^{-4} - 10^{-3}$	-0.249 ± 0.225	-0.838 ± 0.329	$+0.198 \pm 0.297$	$+0.022 \pm 0.038$	$+0.055 \pm 0.056$	-0.006 ± 0.053
5	$< 10^{-5}$	$+0.173 \pm 0.521$	$+0.377 \pm 1.176$	$+0.132 \pm 0.668$	-0.191 ± 0.100	-0.275 ± 0.152	-0.115 ± 0.142
weighted average		-0.022 ± 0.153	-0.359 ± 0.233	$+0.241 \pm 0.202$	-0.001 ± 0.030	$+0.017 \pm 0.044$	-0.009 ± 0.041

Figure 4.24: A graphical presentation of the D^* cross section asymmetry $A^{\gamma^* N \to D^* X}$ from the Table 4.17. The asymmetry of $K^-\pi^+\pi^+$ system is plotted with blue boxes, $K^+\pi^-\pi^-$ with red triangles and the combined asymmetry is plotted with filled black circles.

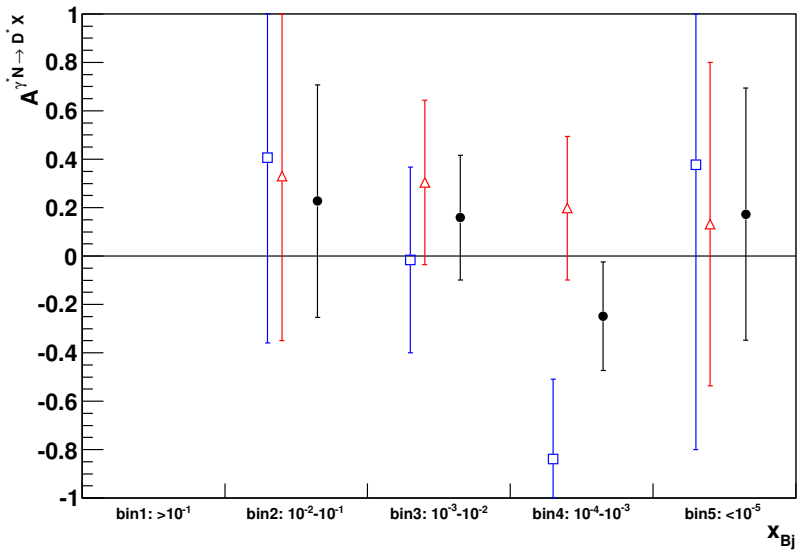

Figure 4.25: A graphical presentation of the background asymmetry A^{bkg} from the Table 4.17. The asymmetry of $K^-\pi^+\pi^+$ system is plotted with blue boxes, $K^+\pi^-\pi^-$ with red triangles and the combined asymmetry is plotted with filled black circles.

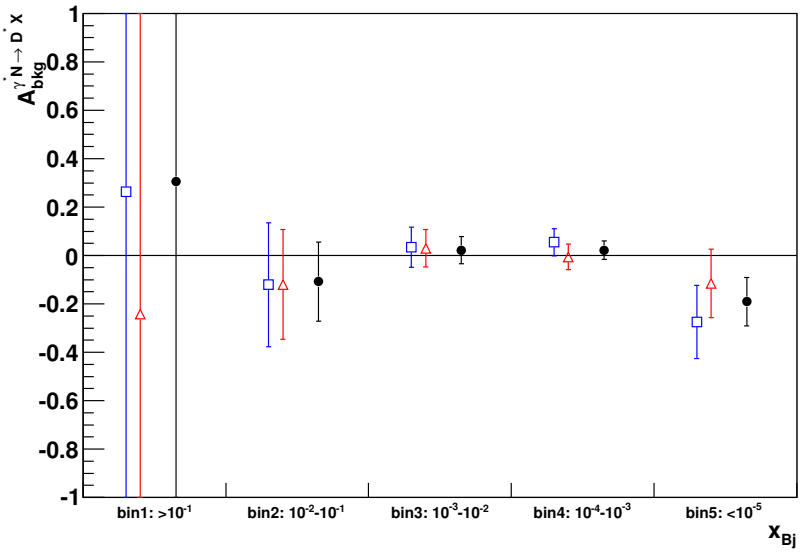

Table 4.18: The cross section spin asymmetry $A^{D^0} = A^{\gamma^* N \to D^0 X}$ for the D^0 mesons without the D^* tag. The asymmetry is calculated for D^0 and $\overline{D^0}$ mesons combined (the table column $A^{D^0+\overline{D^0}}$) and separately for D^0 and $\overline{D^0}$ mesons (the table columns $A^{D^0}(K^-\pi^+)$ and $A^{\overline{D^0}}(K^+\pi^-)$). The background asymmetry (false asymmetry check) is also computed for the $K^-\pi^+$ and $K^+\pi^-$ systems combined and separated (the table columns A^{bkg}, $A^{bkg}(K^+\pi^-)$, $A^{bkg}(K^+\pi^-)$). The asymmetries are calculated as a function of energy E and transverse momentum p_T of the $K\pi$ system. The Figure 4.26 and the Figure 4.27 are graphical presentations of the table content.

bin	P_T [GeV/c]	E [GeV]	A^{D^0}	$A^{D^0}(K^-\pi^+)$	$A^{D^0}(K^+\pi^-)$	A^{bkg}	$A^{bkg}(K^-\pi^+)$	$A^{bkg}(K^+\pi^-)$
1	$0.0-0.3$	$0-30$	$+0.684 \pm 1.857$	-0.001 ± 2.613	$+0.157 \pm 2.016$	-0.045 ± 0.025	-0.030 ± 0.038	-0.058 ± 0.035
2	$0.0-0.3$	$30-50$	-0.331 ± 1.641	$+2.204 \pm 1.315$	-0.413 ± 2.056	-0.024 ± 0.019	-0.008 ± 0.028	-0.036 ± 0.026
3	$0.0-0.3$	$50-160$	$+0.294 \pm 2.851$	-1.570 ± 2.601	$+1.546 \pm 3.173$	$+0.004 \pm 0.025$	$+0.010 \pm 0.037$	-0.005 ± 0.033
4	$0.3-0.7$	$0-30$	$+2.739 \pm 1.057$	$+0.040 \pm 1.341$	$+2.586 \pm 1.881$	$+0.022 \pm 0.015$	$+0.016 \pm 0.023$	$+0.023 \pm 0.020$
5	$0.3-0.7$	$30-50$	-0.645 ± 0.909	-0.336 ± 0.981	-0.993 ± 1.209	-0.012 ± 0.012	-0.027 ± 0.018	-0.001 ± 0.016
6	$0.3-0.7$	$50-160$	-0.508 ± 1.554	-2.038 ± 2.529	-0.225 ± 1.405	$+0.014 \pm 0.018$	$+0.021 \pm 0.026$	$+0.011 \pm 0.024$
7	$0.7-1.0$	$0-30$	-0.735 ± 1.255	$+0.591 \pm 1.467$	-2.966 ± 1.578	$+0.035 \pm 0.020$	$+0.038 \pm 0.030$	$+0.033 \pm 0.027$
8	$0.7-1.0$	$30-50$	$+0.390 \pm 3.246$	$+0.144 \pm 1.092$	$+1.309 \pm 1.169$	$+0.015 \pm 0.014$	$+0.027 \pm 0.022$	$+0.005 \pm 0.020$
9	$0.7-1.0$	$50-160$	$+0.184 \pm 1.055$	$+1.614 \pm 1.190$	-1.101 ± 1.562	-0.002 ± 0.022	$+0.061 \pm 0.034$	-0.048 ± 0.030
10	$1.0-1.5$	$0-30$	-2.018 ± 1.291	-3.171 ± 1.641	$+0.688 \pm 1.686$	$+0.047 \pm 0.027$	$+0.059 \pm 0.033$	$+0.020 \pm 0.032$
11	$1.0-1.5$	$30-50$	$+0.296 \pm 0.605$	-0.020 ± 0.850	$+0.549 \pm 0.673$	-0.002 ± 0.017	$+0.001 \pm 0.026$	-0.001 ± 0.025
12	$1.0-1.5$	$50-160$	$+1.904 \pm 0.787$	$+0.974 \pm 1.286$	$+2.687 \pm 0.927$	$+0.010 \pm 0.028$	-0.021 ± 0.041	$+0.030 \pm 0.044$
13	$1.5-5.0$	$0-30$	$+0.732 \pm 1.407$	-1.384 ± 1.421	-0.842 ± 2.404	$+0.067 \pm 0.050$	$+0.129 \pm 0.077$	$+0.062 \pm 0.067$
14	$1.5-5.0$	$30-50$	$+0.354 \pm 0.616$	$+0.576 \pm 0.681$	$+0.274 \pm 0.782$	-0.037 ± 0.033	$+0.032 \pm 0.054$	-0.079 ± 0.049
15	$1.5-5.0$	$50-160$	$+1.048 \pm 0.605$	$+0.245 \pm 0.928$	$+1.549 \pm 0.781$	-0.044 ± 0.048	$+0.026 \pm 0.066$	-0.110 ± 0.062
weighted average			$+0.517 \pm 0.252$	$+0.200 \pm 0.304$	$+0.629 \pm 0.305$	$+0.004 \pm 0.005$	$+0.011 \pm 0.008$	-0.002 ± 0.007

Figure 4.26: A graphical presentation of the D^0 cross section asymmetry $A^{\gamma^* N \to D^0 X}$ from the Table 4.18. The asymmetry of $K^-\pi^+$ system is plotted with blue boxes, $K^+\pi^-$ with red triangles and the combined asymmetry is plotted with filled black circles.

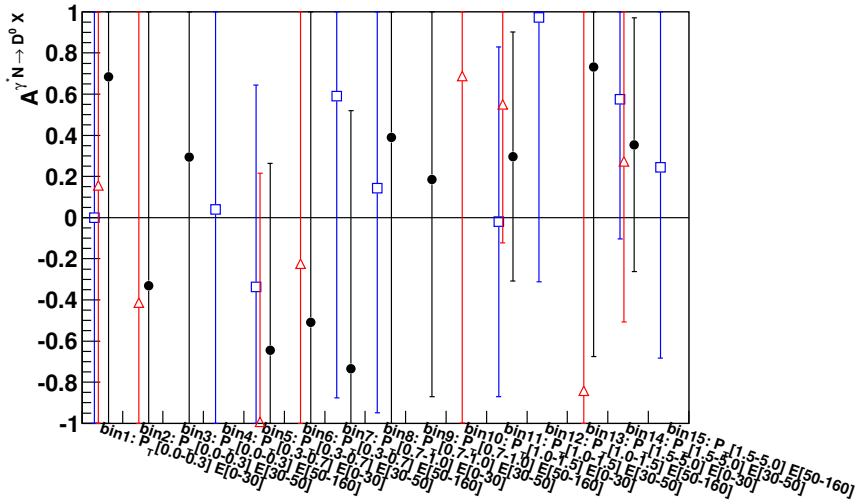

Figure 4.27: A graphical presentation of the background asymmetry A^{bkg} from the Table 4.18. The asymmetry of $K^-\pi^+$ system is plotted with blue boxes, $K^+\pi^-$ with red triangles and the combined asymmetry is plotted with filled black circles.

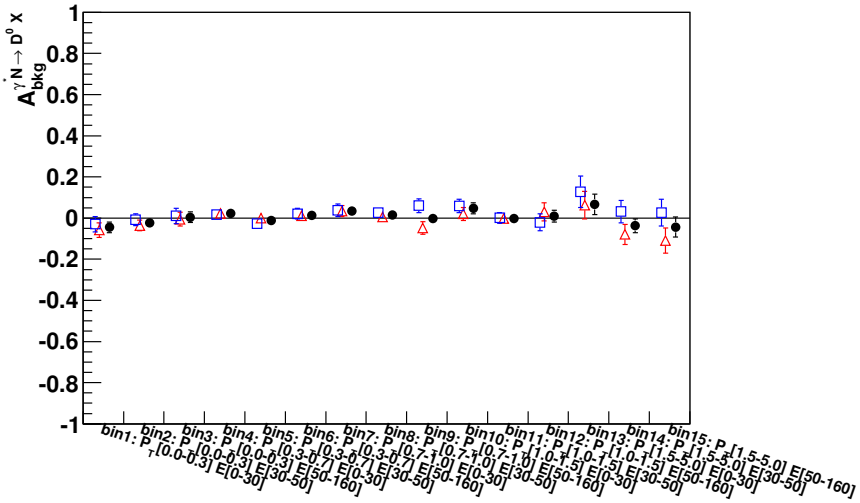

Table 4.19: The same as Table 4.18 but as a function of x_{Bj}: the cross section spin asymmetry $A^{D^0} = A^{\gamma^* N \to D^0 X}$ for the D^0 mesons without the D^* tag. The asymmetry is calculated for D^0 and $\overline{D^0}$ mesons combined (the table column $A^{D^0+\overline{D^0}}$) and separately for D^0 and $\overline{D^0}$ mesons (the table columns $A^{D^0}(K^-\pi^+)$ and $A^{\overline{D^0}}(K^+\pi^-)$). The background asymmetry (false asymmetry check) is also computed for the $K^-\pi^+$ and $K^+\pi^-$ systems combined and separated (the table columns A^{bkg}, $A^{bkg}(K^+\pi^-)$, $A^{bkg}(K^+\pi^-)$). The asymmetries are calculated as a function of x_{Bj}. The Figure 4.28 and the Figure 4.29 are graphical presentations of the table content.

bin	$log_{10}(x_{Bj})$	A^{D^0}	$A^{D^0}(K^-\pi^+)$	$A^{D^0}(K^+\pi^-)$	A^{bkg}	$A^{bkg}(K^-\pi^+)$	$A^{bkg}(K^+\pi^-)$
1	$> 10^{-1}$	$+5.349 \pm 5.920$	-13.830 ± 0.000	$+3.146 \pm 6.235$	$+0.245 \pm 0.174$	$+0.396 \pm 0.270$	$+0.302 \pm 0.221$
2	$10^{-2} - 10^{-1}$	$+1.142 \pm 0.760$	$+0.135 \pm 1.099$	$+1.835 \pm 0.969$	-0.002 ± 0.027	-0.009 ± 0.040	$+0.001 \pm 0.029$
3	$10^{-3} - 10^{-2}$	$+0.400 \pm 0.577$	$+0.820 \pm 0.763$	-0.598 ± 0.732	$+0.000 \pm 0.010$	$+0.018 \pm 0.015$	-0.015 ± 0.013
4	$10^{-4} - 10^{-3}$	$+0.639 \pm 0.651$	$+0.392 \pm 0.742$	$+0.626 \pm 0.954$	$+0.010 \pm 0.007$	$+0.013 \pm 0.010$	$+0.006 \pm 0.009$
5	$< 10^{-5}$	$+2.424 \pm 1.280$	$+1.283 \pm 1.703$	$+2.576 \pm 2.172$	$+0.010 \pm 0.015$	$+0.012 \pm 0.023$	$+0.001 \pm 0.024$
weighted average		$+0.817 \pm 0.360$	$+0.568 \pm 0.461$	$+0.504 \pm 0.484$	$+0.007 \pm 0.005$	$+0.013 \pm 0.008$	$+0.000 \pm 0.007$

Figure 4.28: A graphical presentation of the D^0 cross section asymmetry $A^{\gamma^* N \to D^0 X}$ from the Table 4.19. The asymmetry of $K^-\pi^+$ system is plotted with blue boxes, $K^+\pi^-$ with red triangles and the combined asymmetry is plotted with filled black circles.

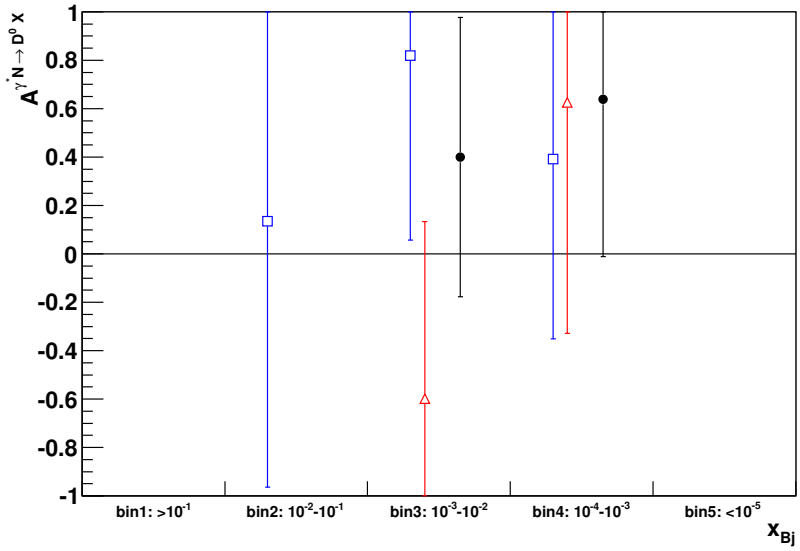

Figure 4.29: A graphical presentation of the background asymmetry A^{bkg} from the Table 4.19. The asymmetry of $K^-\pi^+$ system is plotted with blue boxes, $K^+\pi^-$ with red triangles and the combined asymmetry is plotted with filled black circles.

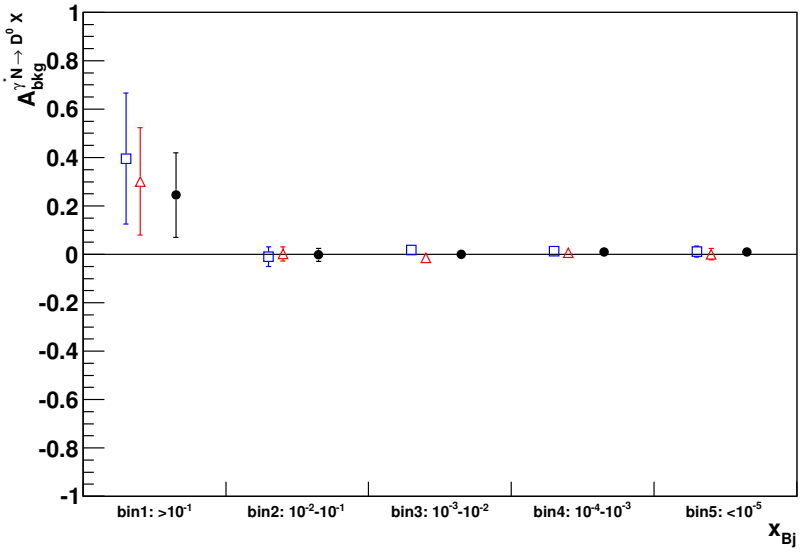

Table 4.20: The cross section spin asymmetry $A^K = A^{\gamma^* N \to K_2^*(1430)^0 X}$ for the $K_2^*(1430)^0$ mesons. The asymmetry is calculated for $K_2^*(1430)^0$ and $\overline{K_2^*}(1430)^0$ mesons combined (the table column A^K) and separately for $K_2^*(1430)^0$ and $\overline{K_2^*}(1430)^0$ mesons (the table columns $A^K(K^-\pi^+)$ and $A^K(K^+\pi^-)$). The background asymmetry (false asymmetry check) is also computed for the $K^-\pi^+$ and $K^+\pi^-$ systems combined and separated (the table columns A^{bkg}, $A^{bkg}(K^+\pi^-)$, $A^{bkg}(K^+\pi^-)$). The asymmetries are calculated as a function of energy E and transverse momentum p_T of the $K\pi$ system. The Figure 4.30 and the Figure 4.31 are graphical presentations of the table content.

bin	P_T [GeV/c]	E [GeV]	A^K	$A^K(K^-\pi^+)$	$A^K(K^+\pi^-)$	A^{bkg}	$A^{bkg}(K^-\pi^+)$	$A^{bkg}(K^+\pi^-)$
1	$0.0-0.3$	$0-30$	$+0.352 \pm 0.170$	$+0.372 \pm 0.270$	$+0.329 \pm 0.216$	-0.041 ± 0.025	-0.028 ± 0.038	-0.051 ± 0.035
2	$0.0-0.3$	$30-50$	$+0.304 \pm 0.201$	$+0.115 \pm 0.303$	$+0.446 \pm 0.267$	-0.022 ± 0.019	-0.006 ± 0.028	-0.035 ± 0.026
3	$0.0-0.3$	$50-160$	-0.358 ± 0.482	-0.413 ± 0.722	-0.180 ± 0.633	$+0.002 \pm 0.026$	$+0.006 \pm 0.037$	-0.005 ± 0.033
4	$0.3-0.7$	$0-30$	$+0.042 \pm 0.095$	-0.122 ± 0.142	$+0.167 \pm 0.128$	$+0.021 \pm 0.015$	$+0.015 \pm 0.022$	$+0.024 \pm 0.021$
5	$0.3-0.7$	$30-50$	$+0.091 \pm 0.100$	$+0.064 \pm 0.153$	$+0.108 \pm 0.121$	-0.012 ± 0.012	-0.027 ± 0.018	-0.002 ± 0.016
6	$0.3-0.7$	$50-160$	$+0.089 \pm 0.178$	-0.226 ± 0.235	$+0.327 \pm 0.235$	$+0.015 \pm 0.018$	$+0.024 \pm 0.027$	$+0.012 \pm 0.025$
7	$0.7-1.0$	$0-30$	-0.071 ± 0.146	-0.305 ± 0.218	$+0.104 \pm 0.195$	$+0.034 \pm 0.020$	$+0.036 \pm 0.030$	$+0.036 \pm 0.027$
8	$0.7-1.0$	$30-50$	$+0.108 \pm 0.103$	-0.068 ± 0.155	$+0.244 \pm 0.137$	$+0.014 \pm 0.015$	$+0.026 \pm 0.022$	$+0.007 \pm 0.020$
9	$0.7-1.0$	$50-160$	$+0.141 \pm 0.212$	-0.116 ± 0.307	$+0.211 \pm 0.281$	-0.004 ± 0.022	$+0.057 \pm 0.030$	-0.051 ± 0.030
10	$1.0-1.5$	$0-30$	-0.022 ± 0.358	-0.140 ± 0.373	$+0.397 \pm 0.437$	$+0.048 \pm 0.027$	$+0.062 \pm 0.037$	$+0.013 \pm 0.034$
11	$1.0-1.5$	$30-50$	-0.037 ± 0.130	$+0.013 \pm 0.194$	-0.115 ± 0.237	-0.003 ± 0.017	$+0.001 \pm 0.026$	-0.004 ± 0.025
12	$1.0-1.5$	$50-160$	$+0.005 \pm 0.308$	$+0.205 \pm 0.489$	-0.163 ± 0.550	$+0.013 \pm 0.027$	-0.016 ± 0.042	$+0.033 \pm 0.043$
13	$1.5-5.0$	$0-30$	-0.088 ± 1.120	-0.585 ± 1.553	-0.021 ± 1.551	$+0.064 \pm 0.050$	$+0.124 \pm 0.077$	$+0.055 \pm 0.067$
14	$1.5-5.0$	$30-50$	$+0.385 \pm 0.276$	$+0.293 \pm 0.524$	$+0.379 \pm 0.512$	-0.035 ± 0.033	$+0.032 \pm 0.054$	-0.078 ± 0.049
15	$1.5-5.0$	$50-160$	$+0.475 \pm 0.558$	-0.517 ± 0.750	$+1.713 \pm 0.809$	-0.048 ± 0.049	$+0.011 \pm 0.073$	-0.108 ± 0.060
weighted average			$+0.087 \pm 0.042$	-0.048 ± 0.063	$+0.188 \pm 0.057$	$+0.003 \pm 0.005$	$+0.011 \pm 0.008$	-0.002 ± 0.007

Figure 4.30: A graphical presentation of the $K_2^*(1430)^0$ cross section asymmetry $A^{\gamma^* N \to K_2^* X}$ from the Table 4.20. The asymmetry of $K^-\pi^+$ system is plotted with blue boxes, $K^+\pi^-$ with red triangles and the combined asymmetry is plotted with filled black circles.

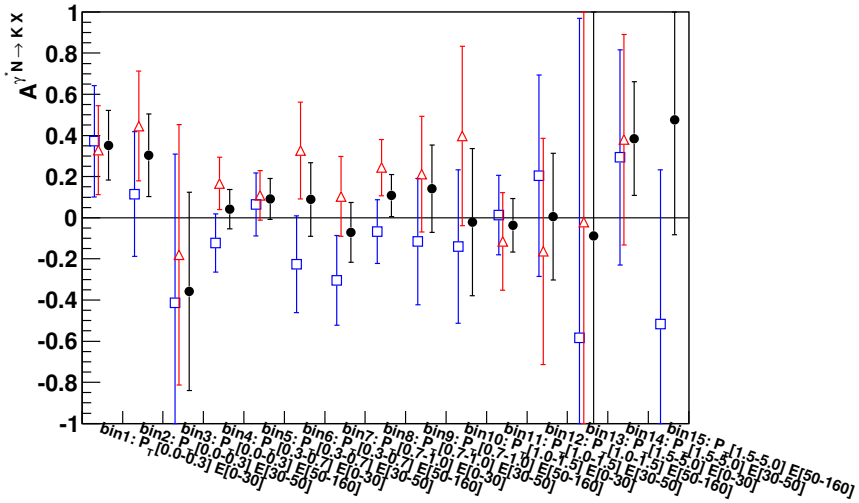

Figure 4.31: A graphical presentation of the background asymmetry A^{bkg} from the Table 4.20. The asymmetry of $K^-\pi^+$ system is plotted with blue boxes, $K^+\pi^-$ with red triangles and the combined asymmetry is plotted with filled black circles.

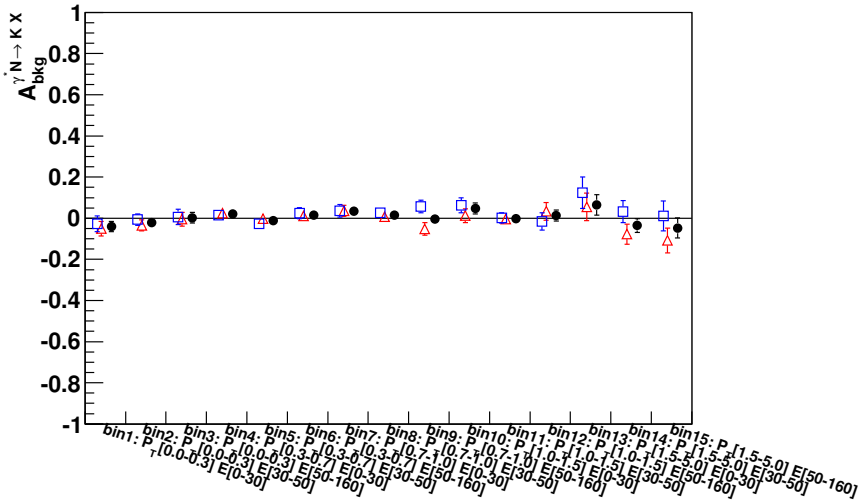

Table 4.21: The same as Table 4.20 but as a function of x_{Bj}: the cross section spin asymmetry $A^K = A^{\gamma^* N \to K_2^*(1430)^0 X}$ for the $K_2^*(1430)^0$ mesons. The asymmetry is calculated for $K_2^*(1430)^0$ and $\overline{K_2^*}(1430)^0$ mesons combined (the table column A^K) and separately for $K_2^*(1430)^0$ and $\overline{K_2^*}(1430)^0$ mesons (the table columns $A^K(K^-\pi^+)$ and $A^K(K^+\pi^-)$). The background asymmetry (false asymmetry check) is also computed for the $K^-\pi^+$ and $K^+\pi^-$ systems combined and separated (the table columns A^{bkg}, $A^{bkg}(K^+\pi^-)$, $A^{bkg}(K^+\pi^-)$). The asymmetries are calculated as a function of x_{Bj}. The Figure 4.32 and the Figure 4.33 are graphical presentations of the table content.

bin	$log_{10}(x_{Bj})$	A^K	$A^K(K^-\pi^+)$	$A^K(K^+\pi^-)$	A^{bkg}	$A^{bkg}(K^-\pi^+)$	$A^{bkg}(K^+\pi^-)$
1	$> 10^{-1}$	-1.080 ± 1.729	-1.357 ± 1.797	-0.773 ± 5.479	$+0.227 \pm 0.200$	$+0.355 \pm 0.242$	$+0.275 \pm 0.773$
2	$10^{-2} - 10^{-1}$	$+0.146 \pm 0.265$	$+0.152 \pm 0.598$	$+0.087 \pm 0.423$	-0.003 ± 0.018	-0.008 ± 0.040	$+0.004 \pm 0.032$
3	$10^{-3} - 10^{-2}$	$+0.002 \pm 0.128$	-0.390 ± 0.193	$+0.298 \pm 0.144$	$+0.001 \pm 0.010$	$+0.018 \pm 0.015$	-0.014 ± 0.013
4	$10^{-4} - 10^{-3}$	$+0.077 \pm 0.056$	-0.048 ± 0.084	$+0.179 \pm 0.075$	$+0.010 \pm 0.007$	$+0.013 \pm 0.010$	$+0.007 \pm 0.009$
5	$< 10^{-5}$	$+0.142 \pm 0.112$	$+0.192 \pm 0.173$	$+0.125 \pm 0.148$	$+0.010 \pm 0.015$	$+0.012 \pm 0.023$	-0.001 ± 0.021
weighted average		$+0.079 \pm 0.046$	-0.053 ± 0.070	$+0.189 \pm 0.060$	$+0.007 \pm 0.005$	$+0.013 \pm 0.007$	$+0.000 \pm 0.007$

Figure 4.32: A graphical presentation of the $K_2^*(1430)^0$ cross section asymmetry $A^{\gamma^* N \to K_2^* X}$ from the Table 4.21. The asymmetry of $K^-\pi^+$ system is plotted with blue boxes, $K^+\pi^-$ with red triangles and the combined asymmetry is plotted with filled black circles.

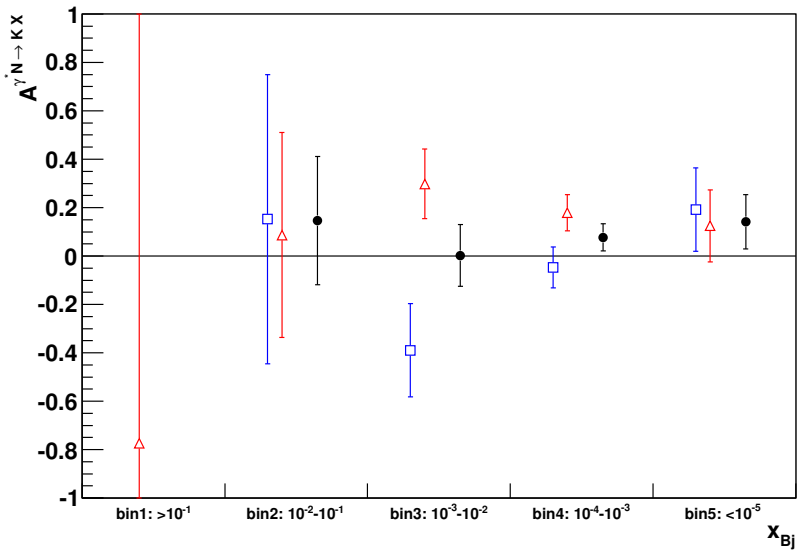

Figure 4.33: A graphical presentation of the background asymmetry A^{bkg} from the Table 4.21. The asymmetry of $K^-\pi^+$ system is plotted with blue boxes, $K^+\pi^-$ with red triangles and the combined asymmetry is plotted with filled black circles.

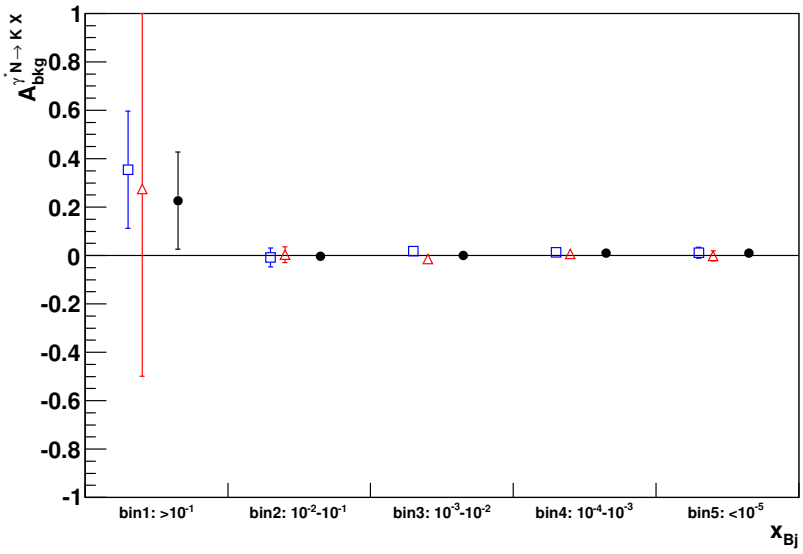

Chapter 5

Conclusion and Outlook

The total visible cross section of $1.8 \pm 0.4\ nb$ for the production of D^{*+} and D^{*-} in inelastic muon nucleon interactions at 160 GeV incident muon energy agrees with the range of values expected if the dominant process is photon-gluon fusion to open $c\bar{c}$.

The detailed comparison of acceptance-corrected kinematical distributions of D^0 and $\overline{D^0}$ from D^* decays with the distributions expected from theory has shown a remarkable agreement, given the fact that the distributions of D mesons are quite different in shape compared to those of the background and the neighbouring $K_2^*(1430)^0$ resonance.

The significant difference between D^{*+} and D^{*-} production at the level of 20 percent, however, is only partially predicted by the theory (AROMA). This indicates that the fragmentation of the quarks is not independent or other processes than PGF contribute by a larger amount than assumed in the theoretical model which was the basis for the generation (AROMA-Monte-Carlo) of the theoretical distributions. These distributions show differences of the same sign as observed but they are much smaller.

The dependence of the differences on various variables, in particular on the photon energy and the scaling variable z, may indicate which processes are responsible. Clearly, different thresholds for D^{*+} and D^{*-} production are exhibited by the distributions shown as a function of photon energy. This observation suggests that the associated production of D^{*-} along with a charmed baryon plays a dominant role at low photon energy. However, over the full photon energy range an almost constant difference of rates is observed, suggesting that this process persists at higher energies or other processes enter the scene.

As a function of z, the most pronounced differences are seen at large values of z, whereas at z values lower than 0.5, the production rates are nearly equal. Since values of z larger 0.5 indicate an asymmetric sharing of the energies between a D meson and its associated partner of opposite charm content, and the D^{*-}, which contains down and anticharm valence quark, wins with increasing z, this observation suggests a process favouring this kind of configuration. Again, associated production is a candidate. Alternatively, since the D^{*-} also contains a valence quark of the nucleon whereas the D^{*+} does not, one may think of other processes than associated production, inolving valence quarks of the nucleon.

The particle-antiparticle asymmetries observed for $D^{*\pm}$ mesons are also seen for D^0 mesons without the D^* tag and for the nearby $K_2^*(1430)^0$ resonance. The weighted aver-

ages of asymmetries $(N(K^-\pi^+) - N(K^+\pi^-)) / (N(K^-\pi^+) + N(K^+\pi^-))$ for all the three mesons (with $K^+\pi-$ and $K^-\pi^+$ decay products) are around ≈ -0.11.

The cross section spin asymmetries has been studied for D^* mesons D^{*+}, D^{*-} and $D^{*+} + D^{*-}$; for D^0 mesons without the D^* tag D^0, $\overline{D^0}$; and for the kaon resonance $K_2^*(1430)^0$,$\overline{K_2^*}(1430)^0$ and $K_2^*(1430)^0$+$\overline{K_2^*}(1430)^0$. No signifcant cross section spin asymmetry is observed for $D^{*\pm}$ and D^0 mesons. The $\Delta G/G$ value computed from such asymmetry will be also compatible with zero. But for the $K_2^*(1430)^0$ meson decaying to $K^+\pi^-$ system, a statistically significant (three sigma effect) cross section spin asymmetry is observed. For the $\overline{K_2^*}(1430)^0$ a possible dependence of the cross section spin asymmetry as a function of x_{Bj} variable is seen.

Appendix A

Particle Properties

The section contains references of basic particle properties relevant for the thesis, more details can be found in [3].

Table A.1: $\pi^{\pm}$

Spin and parity J^P:	0^-				
Quarks content:	$\pi^- : \bar{u}d$		$\pi^+ : u\bar{d}$		
Mass:	139.57018	$\pm$	0.00035	MeV	
Mean life τ:	(2.6033	$\pm$	0.0005	) $\times 10^{-8}$ s	
Decay mode for muon beam					
channel	branching ratio				
$\pi^+ \to \mu^+\nu_\mu$ $\pi^- \to \mu^-\bar{\nu}_\mu$	(99.98770	$\pm$	0.00004	)%	

Table A.2: $K^{\pm}$

Spin and parity J^P:	0^-				
Quarks content:	$K^- : \bar{u}s$		$K^+ : u\bar{s}$		
Mass:	493.677	$\pm$	0.016	MeV	
Mean life τ:	(1.2380	$\pm$	0.0021	) $\times 10^{-8}$ s	
Decay mode for muon beam					
channel	branching ratio				
$K^+ \to \mu^+\nu_\mu$ $K^- \to \mu^-\bar{\nu}_\mu$	(63.55	$\pm$	0.11	)%	

Table A.3: $K^*(892)^0$

Spin and parity J^P:	1^-			
Quarks content:	$K^*(892)^0 : d\bar{s}$		$\overline{K^*}(892)^0 : \bar{d}s$	
Mass:	895.94	$\pm$	0.22	MeV
Width:	48.7	$\pm$	0.8	MeV
Selected decay modes				
channel	branching ratio			
$K^*(892)^0 \to K^+\pi^-$ $\overline{K^*}(892)^0 \to K^-\pi^+$	$\approx 100\%$			

Table A.4: $K_2^*(1430)^0$

Spin and parity J^P:	2^+			
Quarks content:	$K_2^*(1430)^0 : d\bar{s}$		$\overline{K_2^*}(1430)^0 : \bar{d}s$	
Mass:	1432.4	$\pm$	1.3	MeV
Width:	109	$\pm$	5	MeV
Selected decay modes				
channel	branching ratio			
$K_2^*(1430)^0 \to K^+\pi^-$ $\overline{K_2^*}(1430)^0 \to K^-\pi^+$	(49.9	$\pm$	1.2	)%

Table A.5: $K_3^*(1780)^0$

Spin and parity J^P:	3^-			
Quarks content:	$K_3^*(1780)^0 : d\bar{s}$		$\overline{K_3^*}(1780)^0 : \bar{d}s$	
Mass:	1776	$\pm$	7	MeV
Width:	159	$\pm$	21	MeV
Selected decay modes				
channel	branching ratio			
$K_3^*(1780)^0 \to K^+\pi^-$ $\overline{K_3^*}(1780)^0 \to K^-\pi^+$	(18.8	$\pm$	1.0	)%

Table A.6: D^0

Spin and parity J^P:	0^-				
Quarks content:	$D^0 : c\bar{u}$		$\overline{D^0} : \bar{c}u$		
Mass:	1864.83	$\pm$	0.14	MeV	
Mean life τ:	(410.1	$\pm$	1.5	) $\times 10^{-15}$ s	
Selected decay modes					
channel			branching ratio		
$D^0 \to K^-\pi^+$ $\overline{D^0} \to K^+\pi^-$	(3.89	$\pm$	0.05	)%	
Further decay modes seen					
channel			branching ratio		
$D^0 \to K^-\pi^+(\pi^0)$ $\overline{D^0} \to K^+\pi^-(\pi^0)$	(13.9	$\pm$	0.05	)%	

Table A.7: $D^{*\pm}$

Spin and parity J^P:	1^-			
Quarks content:	$D^{*+} : c\bar{d}$		$D^{*-} : \bar{c}d$	
Mass:	2010.25	$\pm$	0.14	MeV
Width:	96	$\pm$	22	keV
Selected decay modes				
channel			branching ratio	
$D^{*+} \to D^0\pi^+$ $D^{*-} \to \overline{D^0}\pi^-$	(67.7	$\pm$	0.5	)%

Appendix B

Invariant $K\pi$ mass fit functions

The appendix explains fit functions used for fitting $K\pi$ invariant mass spectra shown in Figure 4.6(a),(c).

As it was mentioned already in subsection 4.1.1, two functions are used in the fit: one for the D^* sample and another one for the D^0 sample (and also for the combined D^* and D^0 samples):

$$F_{D^*}(m) = N_{bkg}E(m;b) + N_{D^0}G(m;M_{D^0},W_{D^0}) + N_{3b}S_{3b}(m) \quad \text{(B.1)}$$

$$F_{D^0}(m) = N_{bkg}E(m;b) + N_{D^0}G(m;M_{D^0},W_{D^0}) + N_{3b}S_{3b}(m) + N_{K_2}BW(m;M_{K_2},G_{K_2}) + N_{K_3}BW(m;M_{K_3},G_{K_3}) \quad \text{(B.2)}$$

where:

- m - $K\pi$ system invariant mass;
- $E(m;b) = \exp(mb)$ - exponential background;
- $G(m;M,W) = \exp(-\frac{(m-M)^2}{2W^2})/W\sqrt{2\pi}$ - Gaussian distribution to describe the main $D^0 \to K\pi$ peak shape;
- $S_{3b}(m)$ - special shape shown in Table B.1 obtained from a MC simulation to describe the peak from the 3-body decay $D^0 \to K\pi\pi^0$ (see Appendix A Table A.6) which is seen in the $K\pi$ mass spectrum (with undetected π^0);
- $BW(m;M,G) = M^2G^2/((m^2-M^2)^2+M^2G^2)$ - relativistic Breit-Wigner distribution for the $K_2^*(1430)^0$ and $K_3^*(1780)^0$ peaks.

Table B.1: The MC signal shape S_{3b} from a 3-body decay $D^0 \to K\pi\pi^0$ with an undetected π^0, the peak is seen the $K\pi$ spectrum. The shape is given by a tabulated function with 16 equidistant points in the mass range: $m_1 = 1200\ MeV$, $m_{16} = 1800\ MeV$

point	1	2	3	4	5	6	7	8	9	10	11	12	13	14	15	16
N	0.0	0.5	1.0	2.0	3.4	9.1	15.2	21.6	31.2	51.6	67.4	75.7	60.1	20.0	0.7	0.0

Table B.2: Parameter range for the fit functions $F_{D^*}(m)$ and $F_{D^0}(m)$ (Equation B.1 and Equation B.2) used for fitting the $K\pi$ invariant mass m spectrum. For a parameter p, an expression $p = a \pm b$ means that the starting parameter value in the fit is a and the allowed range is $[a - b, a + b]$.

Function	background	$D^0 \to K\pi$ peak	$D^0 \to K\pi\pi^0$ peak	$K_2^*(1430)^0$ peak	$K_3^*(1780)^0$ peak
$F_{D^*}(m)$	$E(m;b)$	$G(m;M_{D^0},W_{D^0})$ $M_{D^0} : 1865 \pm 10$ $W_{D^0} : 25 \pm 7$	$S_{3b}(m)$		
$F_{D^0}(m)$	$E(m;b)$	$G(m;M_{D^0},W_{D^0})$ $M_{D^0} : 1865 \pm 20$ $W_{D^0} : 25 \pm 7$	$S_{3b}(m)$	$BW(m;M_{K_2},G_{K_2})$ $M_{K_2} : 1426 \pm 20$ $G_{K_2} : 102 \pm 50$	$BW(m;M_{K_3},G_{K_3})$ $M_{K_3} : 1776 \pm 20$ $G_{K_2} : 159 \pm 50$

Appendix C

Signal Extraction

The signal extraction methods by signal fit (Signal Extraction by Fit (SEF)) and side bins subtraction (Signal Extraction by Side Bins Subtraction (SES)) were already introduced in subsection 4.1.2. In the present appendix some more details on the methods are provided.

Usually, after all cuts are applied on an event sample, the signal events are still contaminated with background. On a single event basis it is not possible to distinguish between signal and background event [1]. But statistical methods can be used for a sample of events to extract the pure signal distribution, without its background contamination. In this part of the thesis the two methods of signal extraction are explained and compared.

C.1 Signal Extraction by Side Bins Subtraction

The Signal Extraction by Side Bins Subtraction (SES) relies on a few simple assumptions about the background event behavior. In the invariant mass distribution (plot Figure C.1) the signal peak and the background shape are easily identified. First of all, from the full set of events two event subsamples are defined by choosing different regions in the invariant mass plot. The first subsample (SB) contains events where both signal and background events are present. And there are only background events in the second subsample (B).

For a variable x (like energy E, transverse momentum squared p_T^2 etc.) a distribution dN_{SB}/dx contains information both from signal and background events, while dN_B/dx is the background events distribution.

Assuming that:

- the distribution of background events for the variable x in the event subsamples (SB) and (B) are the same;
- the number of background events in the (SB) and (B) subsamples are the same;

[1] In some analysis for a single event it is possible to calculate the *probability* that an event is signal or background.

one can extract the distribution of signal events:

$$\frac{dN_S}{dx} = \frac{dN_{SB}}{dx} - \frac{dN_B}{dx} \tag{C.1}$$

It is not always possible to select *a priori* events subsamples (SB) and (B) such, that the amount of background is the same in both subsamples. But the number of background events in the subsamples (SB) and (B) can be calculated afterwards. This is done by fitting the invariant mass m spectrum of events by a fit function $f(m)$:

$$f(m) = S(m) + B(m) \tag{C.2}$$

where: $S(m)$ and $B(m)$ are functions which describe signal and background shapes. After that the ratio of background events in the (SB) and (B) subsamples can be computed:

$$r = \frac{\int_{(SB)} B(m)dm}{\int_{(B)} B(m)dm} \tag{C.3}$$

and the Equation C.1 is modified:

$$\frac{dN_S}{dx} = \frac{dN_{SB}}{dx} - r \cdot \frac{dN_B}{dx} \tag{C.4}$$

Figure C.1: Definition of signal (SB) and background (B=Bl+Br) bins for the side bins subtraction method applied for D^0 and D^* samples.

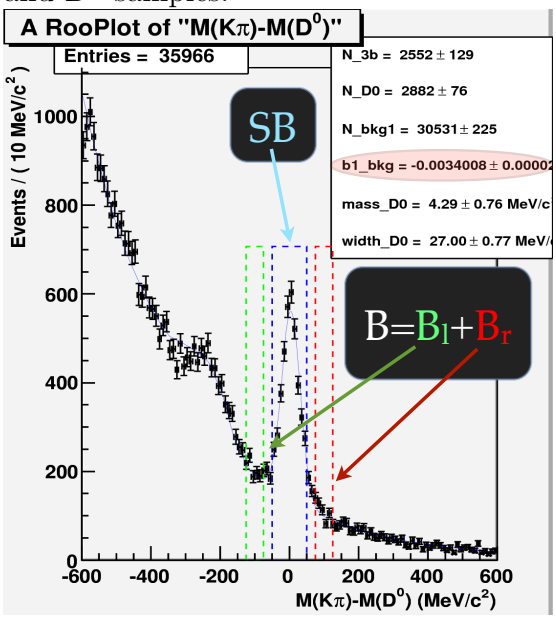

The Figure C.1 demonstrates the choice of the signal (SB) and the side bins (B) for extraction of the D^0 meson kinematical distributions. The factor r is ≈ 0.95 for the given data sample. Thus the SES method with the precise correction for the number of background events in the (SB) sample adopts the same fit function as described in section C.2, but only for the integrated $K\pi$ mass spectrum and only for the background behavior.

C.2 Signal Extraction With Mass Fit

The method relies on the assumption that an invariant mass distribution can be approximately parametrized by a function:

$$f(m) = N^S S(m) + N^B B(m) \tag{C.5}$$

where:

$f(m)$ - fit function for the mass distribution;

$S(m)$,$B(m)$ - probability density functions for signal and background events;

N^S,N^B - number of signal and background events.

To get the distribution of signal events dN/dx as a function of some variable x, the x variable range is divided into several bins Δx_i. For every bin i the invariant mass spectrum is fitted by the fit function C.5. Thus in every bin i the number of signal events ΔN_i^S (and ΔN_i^B for background events) is determined. These numbers $\Delta N_i^S/\Delta x_i$ give the desired signal distribution.

C.3 Comparison of the Signal Extraction Methods

This section contains results of the comparison of the signal extraction methods by SES (section C.1) and SEF (section C.2). The methods were applied for the D^0-*sample* (with a ratio of signal to background events $\approx 1:10$, see Figure 4.6(a)) and for the D^*-*sample* (with a ratio of signal to background events $\approx 1:1$, see Figure 4.6(c)). The signal extraction was checked for the four distributions shown in the section 4.1 as a function of ν, E, p_T^2, z.

The signal extraction method comparison is shown in Figure C.2 and Figure C.3. The results on signal extraction were found to be in agreement with each other. There were few systematic differences between the spectra obtained with the two methods.

First of all it was noticed that the SES method gives slightly less signal ($\approx 5\%$). The explanaition of this signal *leakage* was that the signal bin (SB) (see Figure C.1) does not contain *all* signal events. The signal distribution has left and right tails which are escaping the (SB) bin. Moreover if signal tails are propagated to the side bins (B) (see B_l and B_r bins in Figure C.1), they will be *subtracted* from the signal, resulting that part of the signal is subtracted from the signal. As it was mentioned early, the effect is small for the D^0 signals - the invariant mass distribution is described well by a narrow gaussian shape (the natural D^0 width itself is negligibly small, compared to the spectrometer mass resolution). On the contrary, the $K_2^*(1430)^0$ is wide (see Appendix A) and the spectrometer sees the Breit-Wigner shape of the resonance, which is much wider than the gaussian. It was not possible to define efficiently the signal and background bins. The signal bin needs to be very wide and, as a consequence, the background bin (or bins) has to sit too far from the $K_2^*(1430)^0$ peak. Moreover the side bins contained a significant part of the signal events, which lead to a non-negligable subtraction of signal from signal. As a result of this, the SES method was not applied for the $K_2^*(1430)^0$ meson.

The second systematic difference between the methods is due to the choice of fit function to describe the invariant mass distribution Figure 4.6(a) or Figure 4.6(c). If the fit function does not describe the distribution correctly, the two signal extration methods start to disagree. Originally, to fit the Figure 4.6(a) invariant mass spectrum, three functions were used in the fit. They were exponential for background, a relativistic Breit-Wigner function for the $K_2^*(1430)^0$ meson and a Gaussian distribution for the D^0 meson. There was an agreement between the SES and SEF signal extraction methods for most of the kinematic

distributions, but the results were diverging for the z scaling variable at values $z > 0.8$. To understand this, the seria of plots Figure 4.7(a)-(f) were produced which yield to the conclusion that another resonance ($K_3^*(1780)$) must be added to the fit function. After adding it, the discrepancy of signals extracted at high z values by the two methods were gone, see Figure C.3(d).

In addition to this high-z region problem (which has been successfully fixed in the analysis), it was observed that the chosen shape of the fit function did not describe data well for $E_D < 35\ GeV$ (Figure C.3(b)) and also for $z < 0.35$ Figure C.3(d). Further investigation of these regions possibly may lead to improvements of the signal shape. There are other K resonances present in the $K\pi$ mass spectrum in the vicinity of the D^0 meson. By adding these resonances or/and taking into account a possible interference among them, one may gain in precison of the SEF. But for the present thesis it was decided to exclude the doubtful regions of E_D and z variables, see Figure 4.8(d),(f).

Figure C.2: Comparison of signal extraction for D^0 meson from the D^*-sample (see Figure 4.6(c)): blue circles - signal extraction with the *side bins subtraction* method; red triangles - *the signal fit* method. The *side bins subtraction* method gives slightly less signal. This happens because not all signal events are contained in the *signal* bin - the signal tails (left and right from the central bin) are lost. The leakage is reasonably small for the D^0 signal - it is below 10 %.

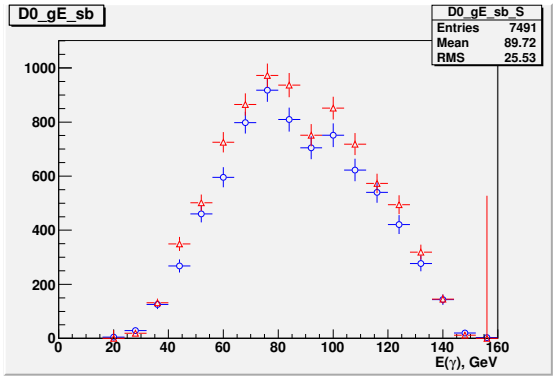

(a) Signal extraction as a function of gamma energy ν

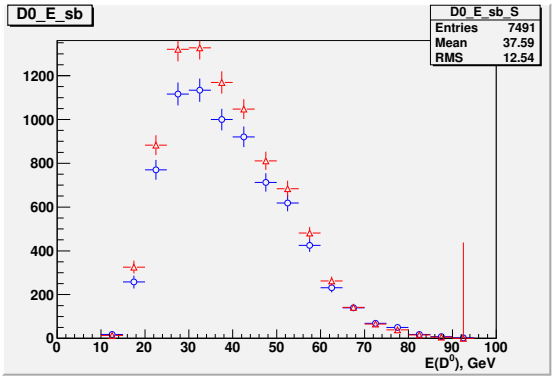

(b) Signal extraction as a function of D^0 energy E

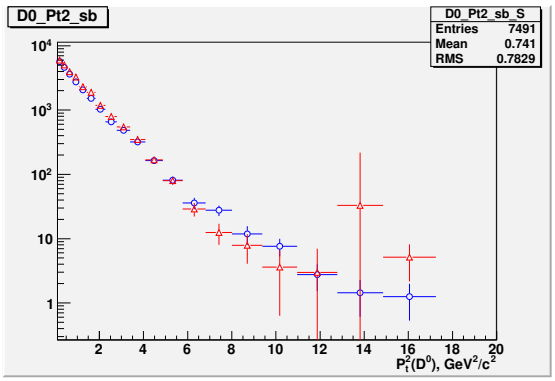

(c) Signal extraction as a function of D^0 squared transverse momentum p_T^2

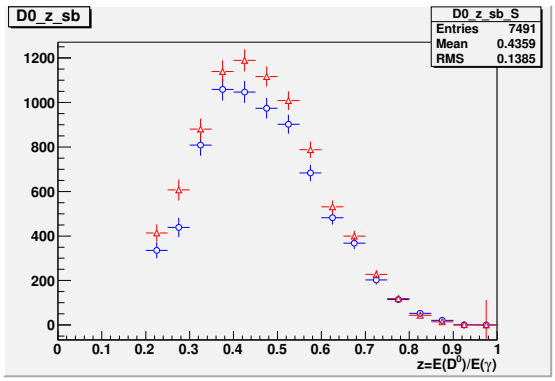

(d) Signal extraction as a function of D^0 energy fraction $z = E/\nu$

Figure C.3: Comparison of signal extraction for D^0 meson from the D^0-sample (see Figure 4.6(a)): blue circles - signal extraction with the *side bins subtraction* method; red triangles - *the signal fit* method. Because of a bad signal to background ratio $\approx 1:10$, some systematic effects start to appear.

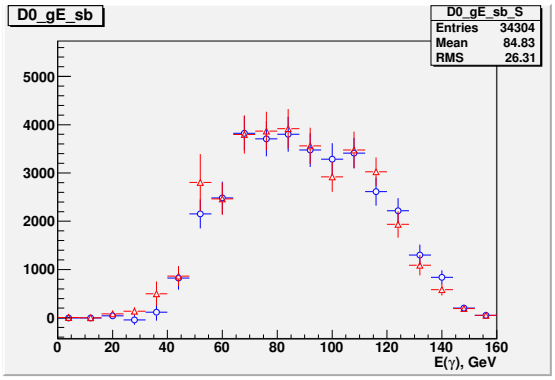

(a) Signal extraction as a function of gamma energy ν

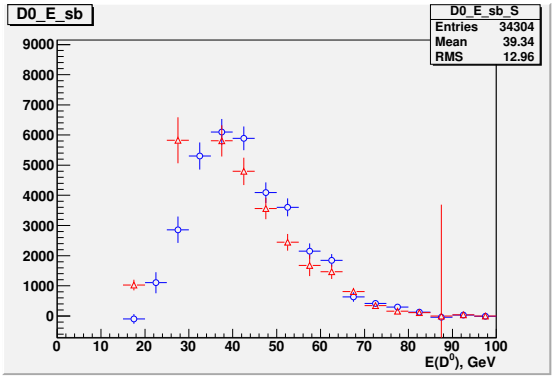

(b) Signal extraction as a function of D^0 energy E

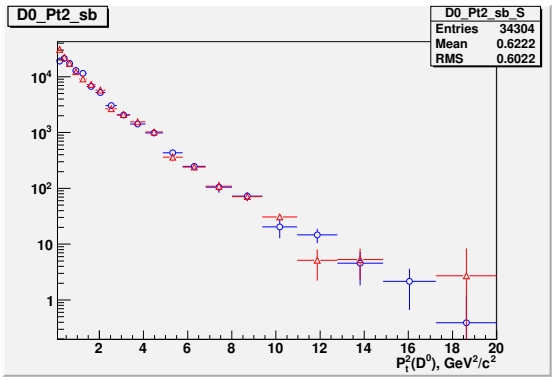

(c) Signal extraction as a function of D^0 squared transverse momentum p_T^2

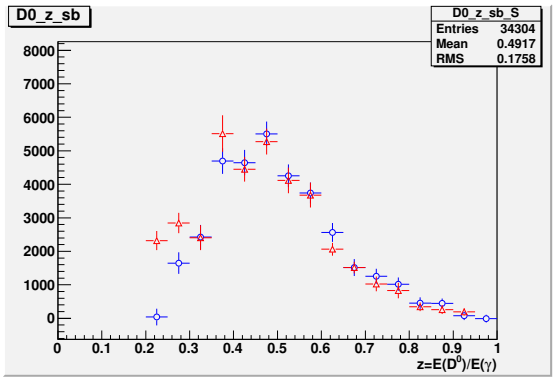

(d) Signal extraction as a function of D^0 energy fraction $z = E/\nu$

Appendix D

Trigger Acceptances and Integrated Luminosity

D.1 Integrated Luminosity Extraction

The number of events N registered in an inclusive muon-nucleon scattering experiment can be presented by the formula:

$$\frac{dN(x,y)}{dx\ dy} = \mathcal{L} \cdot A(x,y) \cdot \frac{d\sigma^{\mu N \to \mu' X}(x,y)}{dx\ dy} \tag{D.1}$$

where x,y is the x-Bjorken and y variable introduced in the chapter 3, $\mathcal{L}$ is the integrated luminosity, $A(x,y)$ is the muon acceptance of the experiment and $d\sigma(x,y)/(dx\ dy)$ is the inclusive muon differential cross section. The latter is connected with the 1-photon exchange cross section via a radiative correction factor $\eta(x,y)$:

$$\sigma^{\mu N \to \mu' X}(x,y) = \frac{\sigma_{1y}(x,y)}{\eta(x,y)} \tag{D.2}$$

and the one photon exchange cross section which is usually written in the form:

$$\frac{d^2\sigma_{1\gamma}(x,y)}{dx\ dy} = (\hbar c)^2 \frac{4\pi\alpha^2}{xyQ^2}\left(1 - y - \frac{Q^2}{4E^2} + \frac{(1-2m^2/Q^2)(y^2+Q^2/E^2)}{2(1+R(x,Q^2))}\right) F_2(x,Q^2) \tag{D.3}$$

The factor $R(x,Q^2)$ is the so-called virtual photon absorption cross section ratio, i.e. the ratio of the longitudinally over the transversely polarized cross section of the virtual photon:

$$R(x,Q^2) = \frac{\sigma_L}{\sigma_T} \tag{D.4}$$

and $F_2(x,Q^2)$ is a structure function which has been measured and parametrized by the New Muon Collaboration (NMC) experiment, see [40]. The Equation D.1 can now be rewritten in a form suitable for an extraction of the integrated luminosity:

$$\mathcal{L} = \frac{dN(x,y)/(dx\ dy)}{A(x,y) \cdot d\sigma^{\mu N \to \mu' X}(x,y)/(dx\ dy)} \tag{D.5}$$

Despite the fact that all terms present on the right hand side of the Equation D.5 depend on (x, y), their product (integrated luminosity) cannot be a function of (x, y). This fact can be used to check the correctness of the muon acceptance $A_\mu(x, y)$ calculation and integrated luminosity $\mathcal{L}$ extraction. Moreover, the integrated luminosity calculated for different triggers (see section 2.2) must be the same, unless triggers were changed during the data taking period.

D.2 Calculated Trigger Acceptances and Integrated Luminosity

The section contains results on acceptence calculations for various triggers, and extracted integral luminosity (data from the year 2004).

The measured number of COMPASS muon events in the year 2004 is shown in Figure D.1. Part of the events located at $x_{Bj} = \frac{m_e}{m_p} \approx 10^{-3.26}$ (m_e is the electron and m_p is the proton masses) correspond to the elastic muon-electron scattering. These no-muon-nucleon scattering events are removed with the cut: $10^{-3.35} < x_{Bj} < 10^{-3.15}$.

The Figure D.2(a) shows the generated (AROMA [31]) distribution ΔN_{gen} of muon events (every event contains a D^{*+} or D^{*-} meson). The Figure D.2(b) shows the cross section:

$$\sigma = \frac{d\sigma^{\mu N \to \mu' X}(x, y)}{dx\ dy} \Delta x \Delta y \tag{D.6}$$

Figure D.3-Figure D.8 demonstrate the COMPASS muon acceptance, data and integrated luminosity extracted for different triggers (see section 2.2). The reconstructed spectrum ΔN_{rec} of MC events is shown in subfigures (a), the resulting acceptance $A(x \pm \frac{\Delta x}{2}, y \pm \frac{\Delta y}{2}) = \Delta N_{rec}/\Delta N_{gen}$ in (b), the real data ΔN_{data} in (c). The integrated lumonosity $\Delta N_{lum} = \Delta N_{data}/(A(x \pm \frac{\Delta x}{2}, y \pm \frac{\Delta y}{2}) \cdot \sigma)$ in units of inverse femtobarns is shown twice: once as a color plot (d) and the second time with numbers (e). The calculation of the COMPASS integrated luminosity for the year 2004 which is based on the muon flux and target material (a direct integrated luminosity calculation) yielded a value of $\mathcal{L} = 0.707\ fb^{-1}$. Deviations from uniformity and the deviation from this expected value may reflect problems of the cross section extrapolation, of the acceptance or of a possible change of the trigger mix during data taking or, finally that the expected number 0.707 inverse femtobarns is not correct.

For all triggers except the calorimeter trigger, the extracted integrated luminosity is reasonably flat and values extracted for different triggers are compatable which each other, see Figure D.4(d),(e) - Figure D.7(d),(e). The relative error on the integrated luminosity extraction with this method is estimated to be $\approx 15\%$ and the agreement with $\mathcal{L} = 0.707\ fb^{-1}$is satisfactory. The figures demonstrate that the COMPASS spectrometer is understood and described in the software (for MC simulation) very well. The only problematic trigger is the *calorimeter* trigger, see Figure D.8(d),(e). Instabilities in energy thresholds for the HCAL2 cells (hardware level) and difficulties in propagation of these

thresholds to the MC simulation of the trigger (software level) lead to these inconsistent results. The fraction of events triggered *only* by the *calorimeter* trigger is relatively small. Most of the time, events are triggered by several triggers simultaneously, so the systematic differences among triggers are smoothed. This can be seen on Figure D.3(d),(e) where analysis was done on all sets of events, independently of their trigger type.

Figure D.1: Event distribution from the year 2004 data and the muon-electron scattering.

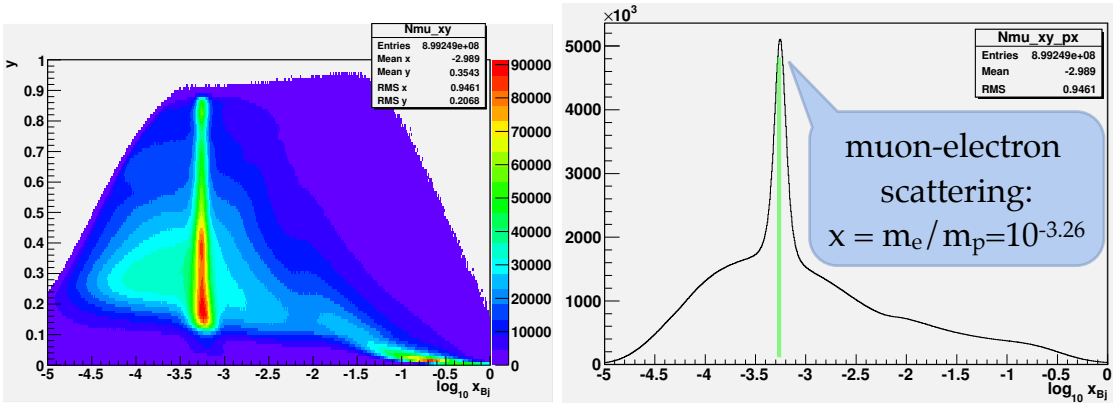

(a) Distribution of events as function of (x, y).

(b) Projection of the Figure D.1(a) distribution to the x_{Bj} axis. The peak corresponding to the muon-electron scattering is easily seen.

Figure D.2:

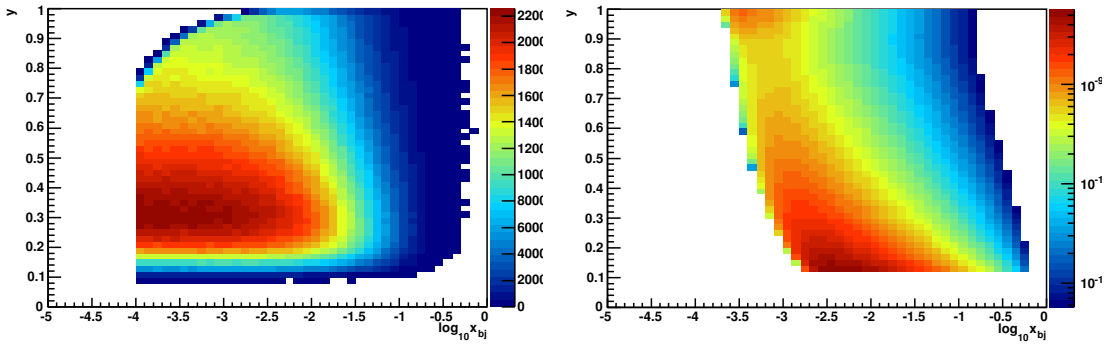

(a) Generated (with AROMA, see [31]) spectrum of muons ΔN_{gen} as a function of (x, y).

(b) Muon-nucleon cross section σ calculated with the Equation D.2 and Equation D.6.

Figure D.3: The **all** triggers (index ALL) acceptance, data and integrated luminosity.

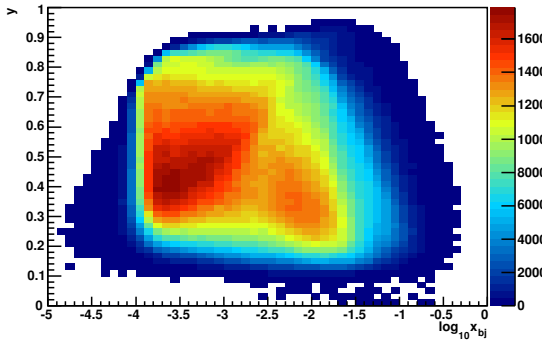

(a) Reconstructed spectrum of MC events for all triggers: ΔN_{rec}^{ALL}

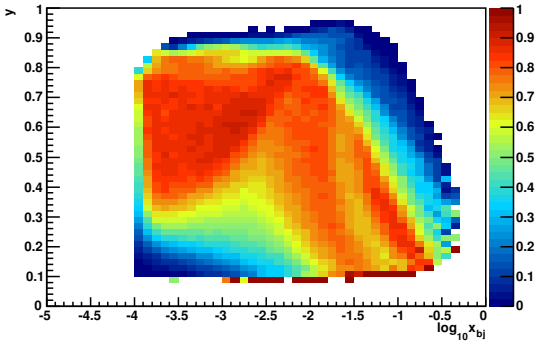

(b) Acceptance $A^{ALL} = \Delta N_{rec}^{ALL} / \Delta N_{gen}$

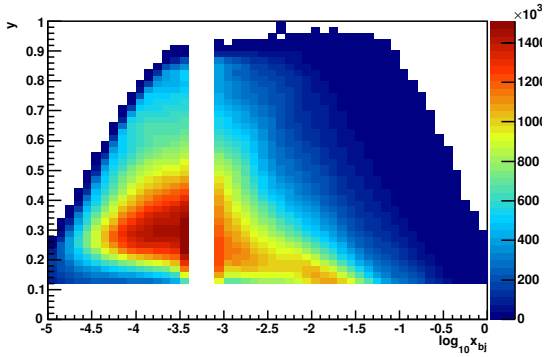

(c) Real data spectrum ΔN_{data}^{ALL} (with the x_{Bj} cut, see Figure D.1)

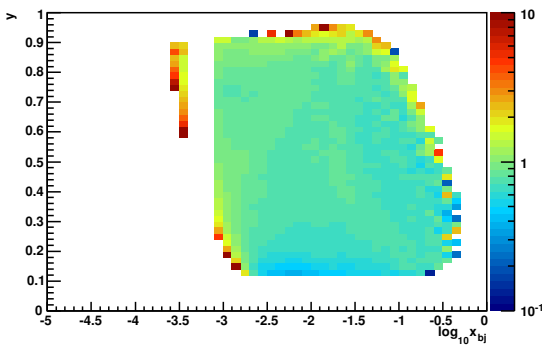

(d) Integrated luminosity: $\Delta N_{lum}^{ALL} = \Delta N_{data}^{ALL} / (A^{ALL} \cdot \sigma)$in units of inverse femtobarns.

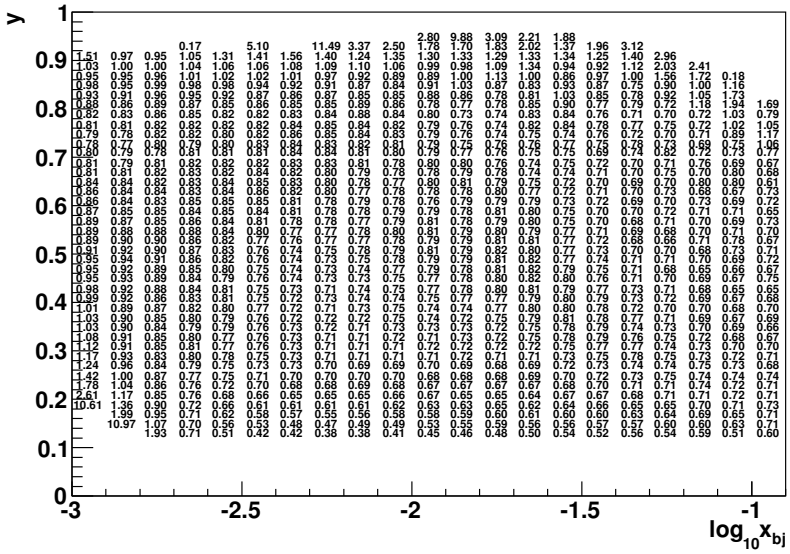

(e) Text view of the Figure D.3(d) subrange: the integrated luminosity: $\Delta N_{lum}^{ALL} = \Delta N_{data}^{ALL} / (A^{ALL} \cdot \sigma)$in units of inverse femtobarns

Figure D.4: The **inner** trigger (index I) acceptance, data and integrated luminosity.

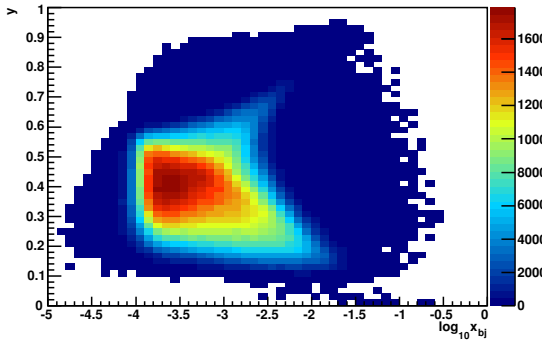

(a) Reconstructed spectrum of MC events for inner trigger: ΔN^I_{rec}

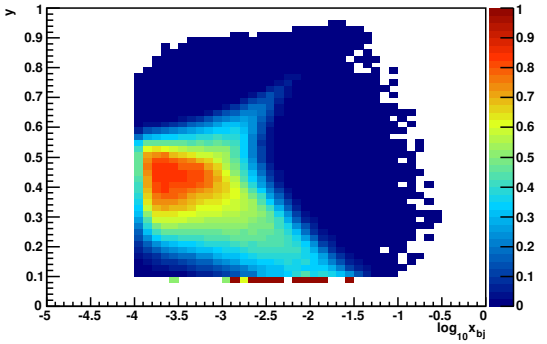

(b) Acceptance $A^I = \Delta N^I_{rec}/\Delta N_{gen}$

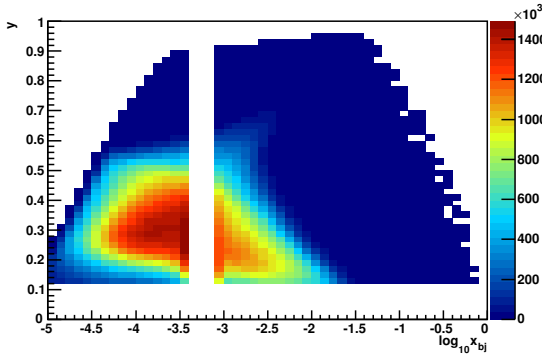

(c) Real data spectrum ΔN^I_{data} (with the x_{Bj} cut, see Figure D.1)

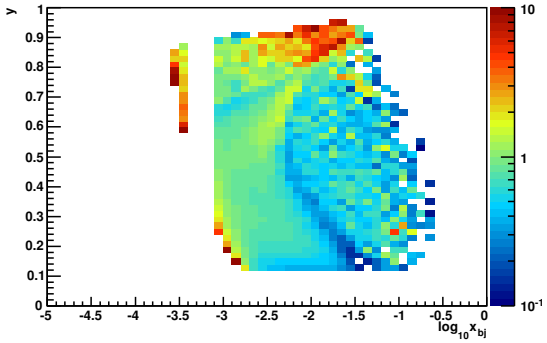

(d) Integrated luminosity: $\Delta N^I_{lum} = \Delta N^I_{data}/(A^I \cdot \sigma)$in units of inverse femtobarns.

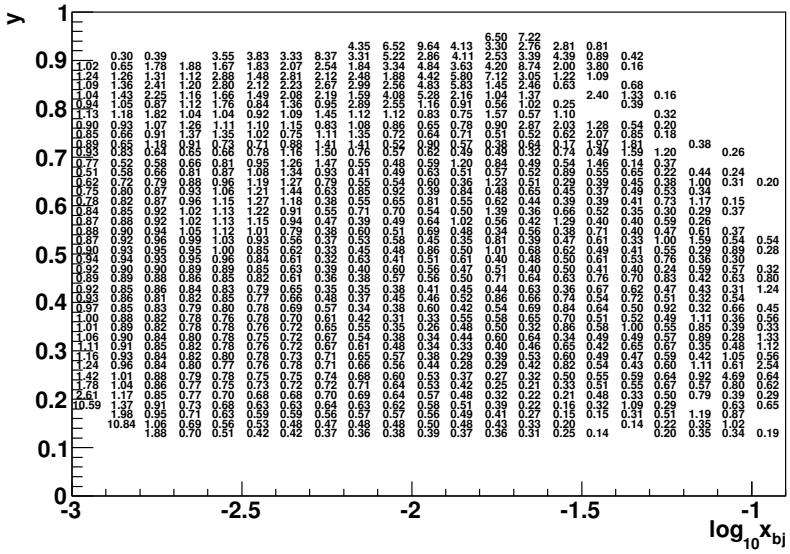

(e) Text view of the Figure D.4(d) subrange: the integrated luminosity: $\Delta N^I_{lum} = \Delta N^I_{data}/(A^I \cdot \sigma)$in units of inverse femtobarns

Figure D.5: The **ladder** trigger (index L) acceptance, data and integrated luminosity.

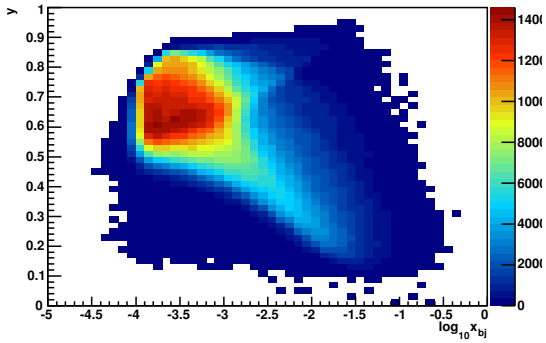

(a) Reconstructed spectrum of MC events for ladder trigger: ΔN^L_{rec}

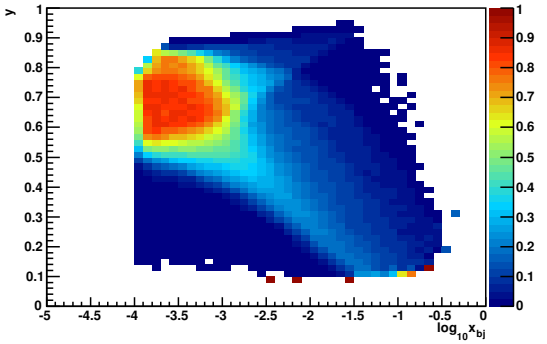

(b) Acceptance $A^L = \Delta N^L_{rec}/\Delta N_{gen}$

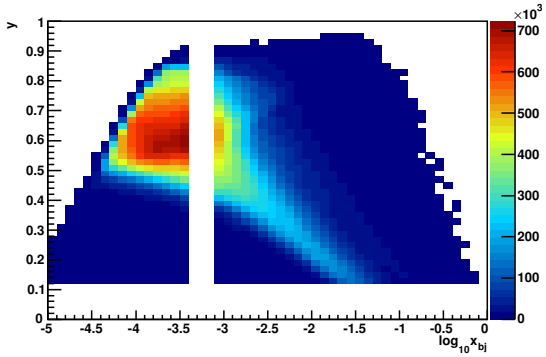

(c) Real data spectrum ΔN^L_{data} (with the x_{Bj} cut, see Figure D.1)

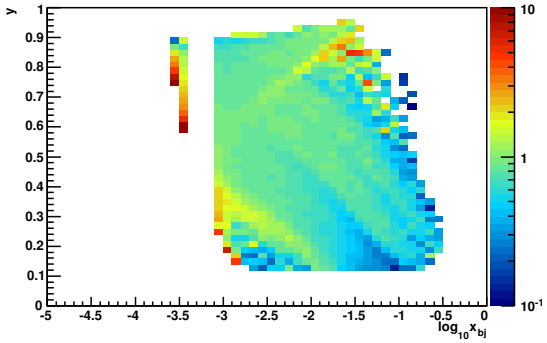

(d) Integrated luminosity: $\Delta N^L_{lum} = \Delta N^L_{data}/(A^L \cdot \sigma)$in units of inverse femtobarns.

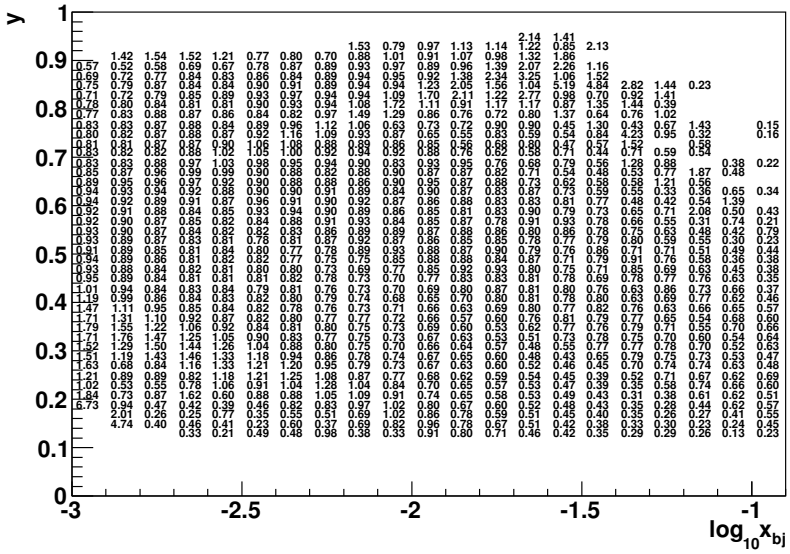

(e) Text view of the Figure D.5(d) subrange: the integrated luminosity: $\Delta N^L_{lum} = \Delta N^L_{data}/(A^L \cdot \sigma)$in units of inverse femtobarns

Figure D.6: The **inclusive middle** trigger (index IM) acceptance, data and integrated luminosity.

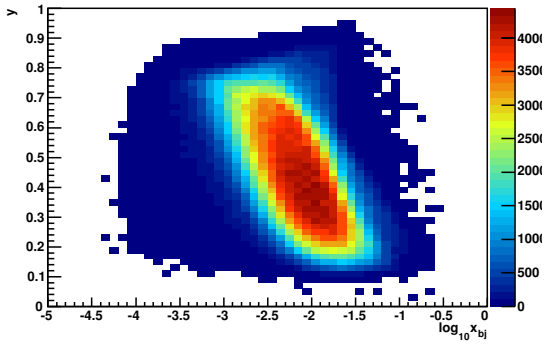

(a) Reconstructed spectrum of MC events for inclusive middle trigger: ΔN_{rec}^{IM}

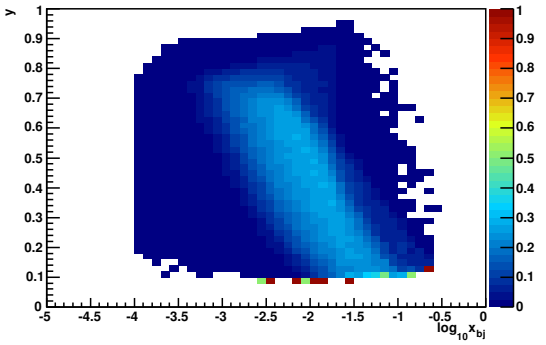

(b) Acceptance $A^{IM} = \Delta N_{rec}^{IM} / \Delta N_{gen}$

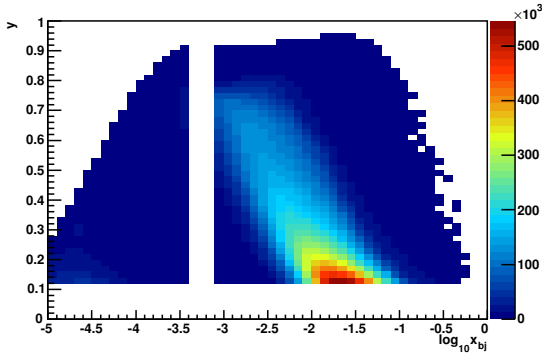

(c) Real data spectrum ΔN_{data}^{IM} (with the x_{Bj} cut, see Figure D.1)

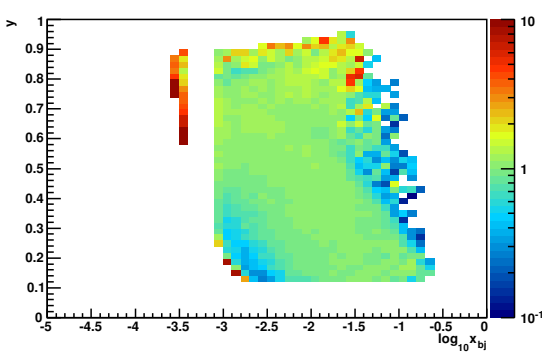

(d) Integrated luminosity: $\Delta N_{lum}^{IM} = \Delta N_{data}^{IM} / (A^{IM} \cdot \sigma)$in units of inverse femtobarns.

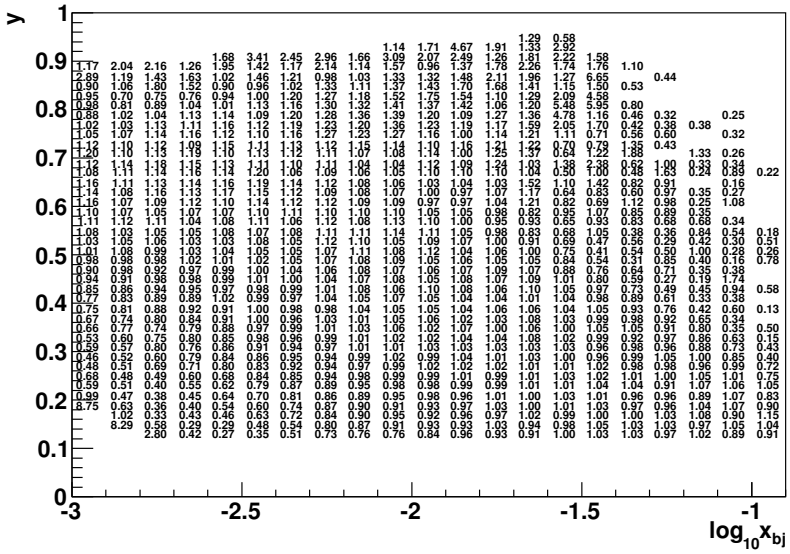

(e) Text view of the Figure D.6(d) subrange: the integrated luminosity: $\Delta N_{lum}^{IM} = \Delta N_{data}^{IM} / (A^{IM} \cdot \sigma)$in units of inverse femtobarns

Figure D.7: The **middle** trigger (index M) acceptance, data and integrated luminosity.

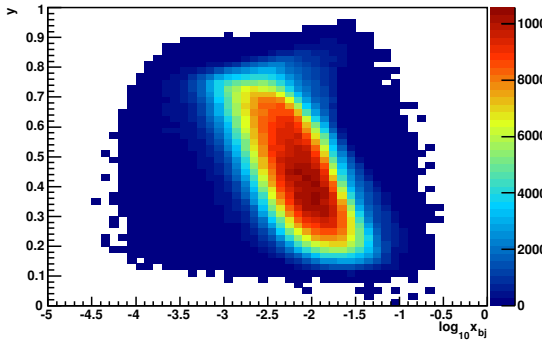

(a) Reconstructed spectrum of MC events for middle trigger: ΔN^M_{rec}

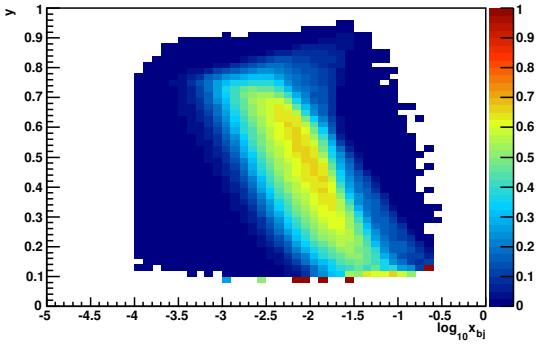

(b) Acceptance $A^M = \Delta N^M_{rec}/\Delta N_{gen}$

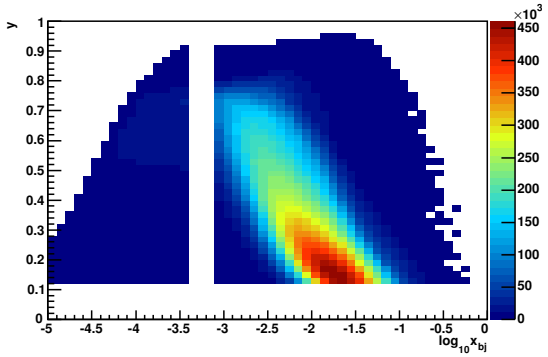

(c) Real data spectrum ΔN^M_{data} (with the x_{Bj} cut, see Figure D.1)

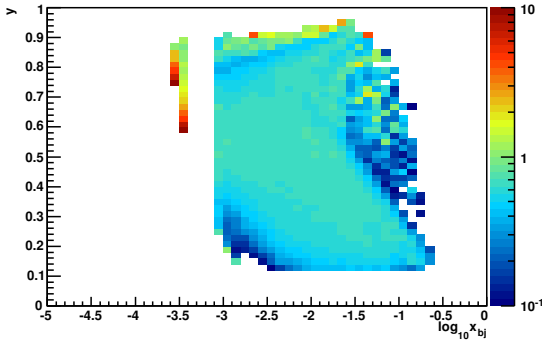

(d) Integrated luminosity: $\Delta N^M_{lum} = \Delta N^M_{data}/(A^M \cdot \sigma)$in units of inverse femtobarns.

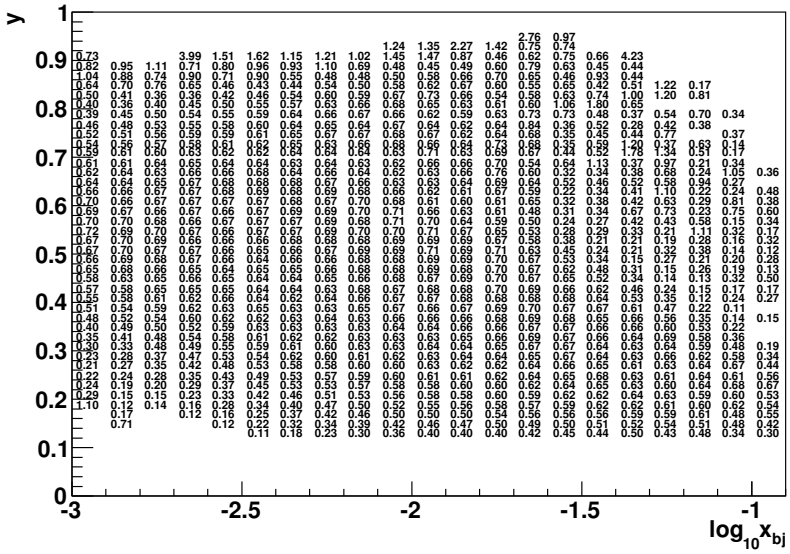

(e) Text view of the Figure D.7(d) subrange: the integrated luminosity: $\Delta N^M_{lum} = \Delta N^M_{data}/(A^M \cdot \sigma)$in units of inverse femtobarns

Figure D.8: The **calorimeter** trigger (index C) acceptance, data and integrated luminosity.

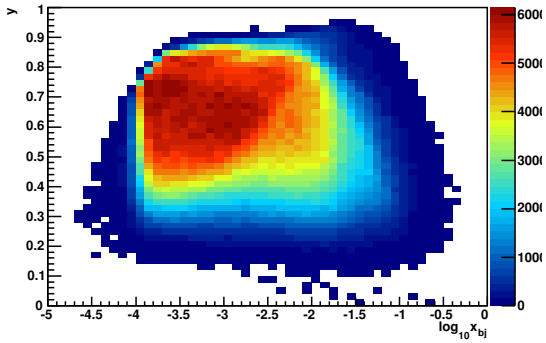

(a) Reconstructed spectrum of MC events for calorimeter trigger: ΔN^C_{rec}

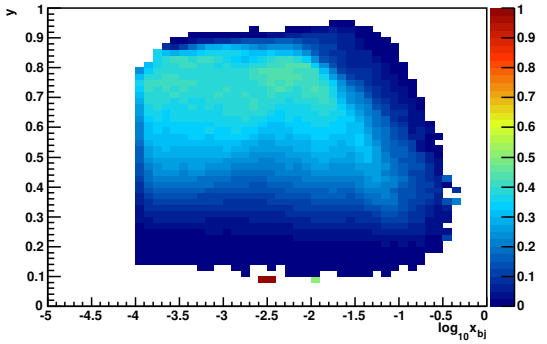

(b) Acceptance $A^C = \Delta N^C_{rec}/\Delta N_{gen}$

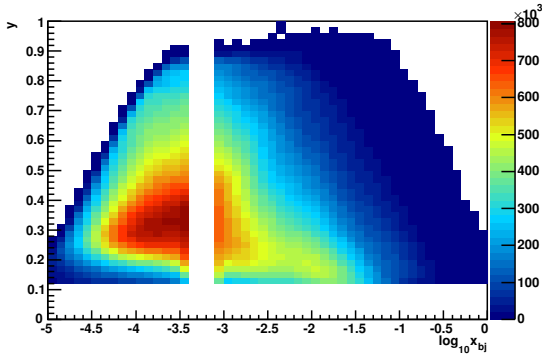

(c) Real data spectrum ΔN^C_{data} (with the x_{Bj} cut, see Figure D.1)

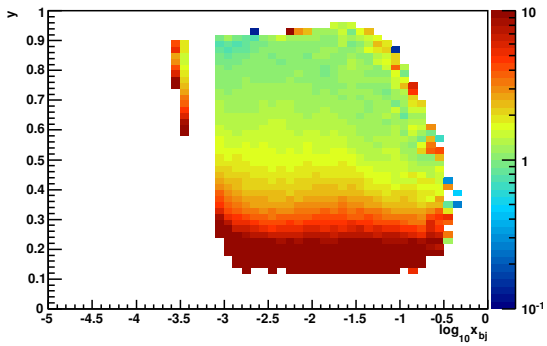

(d) Integrated luminosity: $\Delta N^C_{lum} = \Delta N^C_{data}/(A^C \cdot \sigma)$in units of inverse femtobarns.

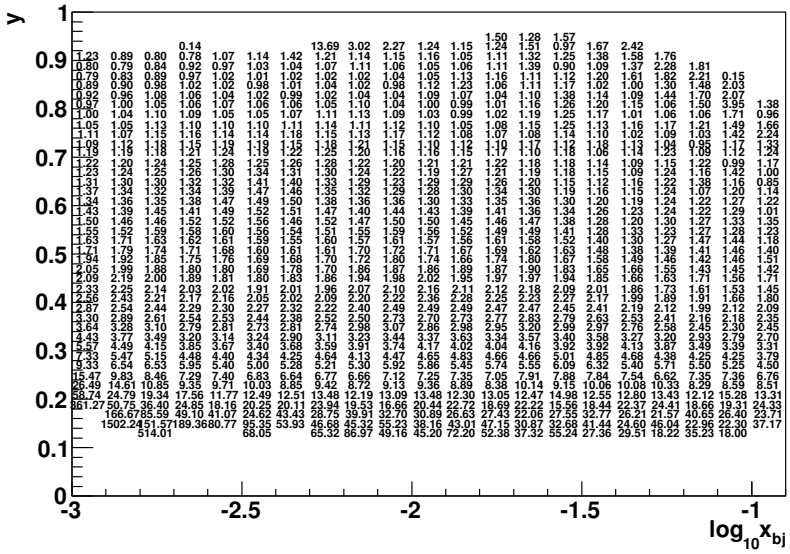

(e) Text view of the Figure D.8(d) subrange: the integrated luminosity: $\Delta N^C_{lum} = \Delta N^C_{data}/(A^C \cdot \sigma)$in units of inverse femtobarns

Appendix E

Motivation of binning (E, p_T)

Asymmetries presented in subsection 4.1.7 and subsection 4.2.3 are shown as a function of x_{Bj} and (E, p_T) of the $K\pi$ system. The choice of the x_{Bj} variable is a traditional presentation of asymmetries in DIS experiments. The (E, p_T) binning was chosen as in the COMPASS publication [2], where $\Delta G/G$ and longitudinal double spin asymmetries were published. As it was already mentioned in section 3.3, the measured photon-nucleon asymmetry divided by photon-gluon to charm meson analysing power $\hat{a}_{LL}$ gives $\Delta G/G$, see Equation 3.14.

It is convenient to introduce also the muon-gluon to charm meson analysing power a_{LL}, which is related to the photon-nucleon to charm meson $\hat{a}_{LL}$ through the depolarization factor $D(y)$, the same way as for the photon-nucleon and muon-nucleon asymmetries Equation 3.15:

$$a_{LL} = \hat{a}_{LL} \cdot D(y) \tag{E.1}$$

On the parton level the a_{LL} (and of course $\hat{a}_{LL}$ as well) depends on the center of mass energy of the muon-nucleon and angle of outgoing quark with respect to the collision axis. The observed D - meson (a result of the c quark fragmentation) variables energy E and transverse momentum p_T are related with these partonic variables. For every combination E, p_T an average a_{LL} can be estimated from a full MC simulation (AROMA). The value of a_{LL} may change sign in different regions of the phase space. In the case of COMPASS PGF events, the overall average of a_{LL} is close to zero, so there is no sensitivity in $\Delta G/G$ measurements if one would average over all events. Therefore, the binning in E, p_T is needed.

Figure E.1 shows (a) a_{LL} and (b) COMPASS D^* tagged data for events around the nominal D^0 mass. The best regions for $\Delta G/G$ extraction would be with $|a_{LL}| \approx 1$, that approximetely correspond to the point $E \approx 60\ GeV$ and $p_T \approx 0.3\ GeV$, see Figure E.1(a). The COMPASS D^* events peaked at $E \approx 30\ GeV$ and $p_T \approx 0.7\ GeV$, see Figure E.1(b). And unfortunetely, at this point a_{LL} is close to zero.

Finally, the chosen binning in E, p_T is the following:

- p_T $[0 : 0.03 : 0.07 : 0.1 : 1.5 : 5]$ GeV/c

- E $[0 : 30 : 50 : 160]$ GeV.

Figure E.1: The a_{LL} and COMPASS data as a function of energy E and transverse momentum p_T for the $K\pi$ system for the events in the window ± 70 MeV around the D^0 nominal mass for the D^* tagged events, the data of 2002-2006 were used. The green grid shown on the plots indicate the chosen binning in (E, p_T).

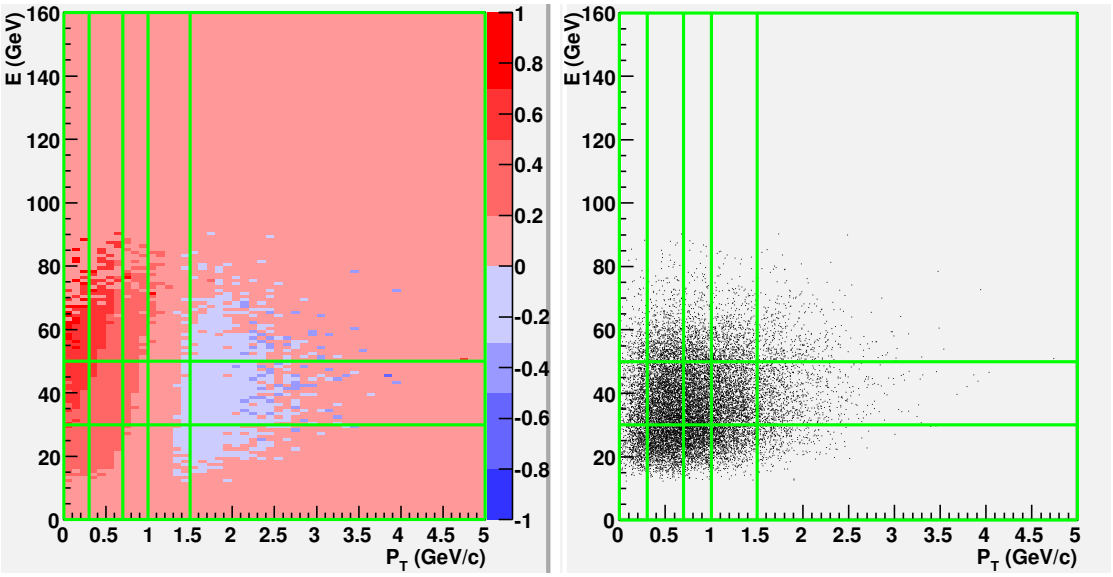

(a) Estimated muon-gluon to charm meson analysing power a_{LL}. For every event a_{LL} is calculated using the parameterizations of $D(y)$ and photon-gluon to charm meson analysing power $\hat{a}_{LL}$. The latter is obtained from a leading order QCD calculation of the cross sections.

(b) Distribution of events.

Glossary

AROMA A Monte Carlo Generator for Heavy Flavour Events in ep Collisions, see [31]. 52, 53, 55, 58, 59, 95, 110, 119

best primary vertex CORAL may reconstruct more than one primary vertex in a single event. In this case a *best* one is chosen, according to special criteria. 42

CORAL The COMPASS reconstruction program. Uses as input raw data (readout from detectors), geometry information, detector calibration constants and produces a DST. 11, 15, 26, 31, 121

dilution factor Fraction of polarizable material. It mainly depends on polarizable properties of nucleons in the material. 79

DST DST is an abbreviation for *Data Summary Tape*. Data in a format suitable for physics analysis. A DST event (contrary to a raw event) contains reconstructed particles, tracks, vertices, etc . 39, 40, 121

ECAL1 Electromagnetic calorimeter located after the magnet SM1. 9

ECAL2 Electromagnetic calorimeter located after the magnet SM2. 9

HCAL1 Hadron calorimeter located after the magnet SM1. 9

HCAL2 Hadron calorimeter located after the magnet SM2. 9, 11, 110

LO Leading order corrections in perturbative QCD calculations. 36

NLO Next to leading order corrections in perturbative QCD calculations. 3

open charm The *open charm* term is used to indicate that a hadron (meson) contains a single charm or anti-charm quark. And the *hidden charm* term would indicate the presence of $c\bar{c}$ pair. 2

raw event A collection of detector responses to some trigger(s). The raw event needs to be reconstructed to extract track momenta, coordinates, etc. 11, 121

RT-relation The relation between drift time (T) and track-to-wire distance (R) for drift detectors. Depends mainly on the gas mixture and electrical field. 15–17, 19, 22

SM1 First COMPASS magnet (part of LAS) with the integral field of 1.0 $T \cdot m$. 9–12, 121

SM2 Second COMPASS magnet (part of SAS) with the integral field of 4.4 $T \cdot m$. 9, 11, 12, 121

spill Particles accelerators usually deliver particles not uniformly in space/time but in "bunches", which are also called "spills". 7

Bibliography

[1] J. Ashman *et al.*, "An investigation of the spin structure of the proton in deep inelastic scattering of polarized muons on polarized protons," *Nucl. Phys.*, vol. B328, p. 1, 1989.

[2] M. Alekseev *et al.*, "Gluon polarisation in the nucleon and longitudinal double spin asymmetries from open charm muoproduction," *Phys. Lett.*, vol. B676, pp. 31–38, 2009.

[3] K. Nakamura and others (Particle Data Group), "The review of particle physics," *J. of Phys.*, vol. G37, 2010.

[4] M. G. Alekseev *et al.*, "Measurement of the Collins and Sivers asymmetries on transversely polarised protons," *Phys. Lett.*, vol. B692, pp. 240–246, 2010.

[5] A. D. Watson, "Spin Spin Asymmetries in Inclusive Muon Proton Charm Production," *Zeit. Phys.*, vol. C12, p. 123, 1982.

[6] W. Beenakker, H. Kuijf, W. L. van Neerven, and J. Smith, "QCD Corrections to Heavy Quark Production in $p\overline{p}$ Collisions," *Phys. Rev.*, vol. D40, pp. 54–82, 1989.

[7] R. K. Ellis and P. Nason, "QCD Radiative Corrections to the Photoproduction of Heavy Quarks," *Nucl. Phys.*, vol. B312, p. 551, 1989.

[8] J. Smith and W. L. van Neerven, "QCD corrections to heavy flavor photoproduction and electroproduction," *Nucl. Phys.*, vol. B374, pp. 36–82, 1992.

[9] S. Frixione, M. L. Mangano, P. Nason, and G. Ridolfi, "Heavy quark correlations in photon - hadron collisions," *Nucl. Phys.*, vol. B412, pp. 225–259, 1994.

[10] I. Bojak and M. Stratmann, "Photoproduction of heavy quarks in next-to-leading order QCD with longitudinally polarized initial states," *Nucl. Phys.*, vol. B540, pp. 345–381, 1999.

[11] P. Nason and C. Oleari, "A phenomenological study of heavy-quark fragmentation functions in e^+ e^- annihilation," *Nucl. Phys.*, vol. B565, pp. 245–266, 2000.

[12] S. Frixione *et al.*, "Heavy flavor production and fragmentation," *J. Phys.*, vol. G27, pp. 1111–1157, 2001.

[13] S. J. Brodsky and M. Karliner, "Intrinsic charm of vector mesons: A possible solution of the '$\rho\pi$ puzzle'," *Phys. Rev. Lett.*, vol. 78, pp. 4682–4685, 1997.

[14] R. Vogt and S. J. Brodsky, "Charmed Hadron Asymmetries in the Intrinsic Charm Coalescence Model," *Nucl. Phys.*, vol. B478, pp. 311–334, 1996.

[15] S. J. Brodsky, C. Peterson, and N. Sakai, "Intrinsic Heavy Quark States," *Phys. Rev.*, vol. D23, p. 2745, 1981.

[16] M. P. Rekalo and E. Tomasi-Gustafsson, "Associative charm photoproduction with circularly polarized photons," *Phys. Lett.*, vol. B541, pp. 101–107, 2002.

[17] A. Capella and J. Tran Thanh Van, "A New Parton Model Description of Soft Hadron-Nucleus Collisions," *Phys. Lett.*, vol. B93, p. 146, 1980.

[18] M. P. Alvarez *et al.*, "Study of charm photoproduction mechanisms," *Z. Phys.*, vol. C60, pp. 53–62, 1993.

[19] A. Aktas *et al.*, "Inclusive $D^{*\pm}$ meson and associated dijet production in deep-inelastic scattering at HERA," *Eur. Phys. J.*, vol. 51, pp. 271–287, 2007. 10.1140/epjc/s10052-007-0296-5.

[20] S. Chekanov *et al.*, "Inclusive jet cross sections and dijet correlations in $D^{*\pm}$ photoproduction at HERA," *Nucl. Phys.*, vol. B729, pp. 492–525, 2005.

[21] A. V. Lipatov and N. P. Zotov, "Charm photoproduction at HERA: k_T-factorization versus experimental data," *Phys. Rev.*, vol. D75, p. 014028, 2007.

[22] J. J. Aubert *et al.*, "D^0 production in deep inelastic muon scattering on hydrogen and deuterium," *Phys. Lett.*, vol. B167, p. 127, 1986.

[23] M. G. Alekseev *et al.*, "Quark helicity distributions from longitudinal spin asymmetries in muon-proton and muon-deuteron scattering," *Phys. Lett.*, vol. B693, pp. 227–235, 2010.

[24] P. Abbon *et al.*, "The COMPASS Experiment at CERN," *Nucl. Instrum. Meth.*, vol. A577, pp. 455–518, 2007.

[25] K. Kondo *et al.*, "Polarization measurement in the COMPASS polarized target," *Nucl. Instrum. Meth.*, vol. A526, pp. 70–75, 2004.

[26] C. Bernet *et al.*, "The COMPASS trigger system for muon scattering," *Nucl. Instrum. Meth.*, vol. A550, pp. 217–240, 2005.

[27] V. N. Bychkov *et al.*, "Construction and manufacture of large size straw-chambers of the COMPASS spectrometer tracking system," *Part. Nucl. Lett.*, vol. 111, pp. 64–73, 2002.

[28] V. N. Bychkov *et al.*, "The large size straw drift chambers of the COMPASS experiment," *Nucl. Instrum. Meth.*, vol. A556, pp. 66–79, 2006.

[29] J. C. Collins, "Hard scattering in QCD with polarized beams," *Nucl. Phys.*, vol. B394, pp. 169–199, 1993.

[30] A. Bravar, K. Kurek, and R. Windmolders, "POLDIS: A Monte Carlo for polarized (semi-inclusive) deep inelastic scattering," *Comput. Phys. Commun.*, vol. 105, pp. 42–61, 1997.

[31] G. Ingelman, J. Rathsman, and G. A. Schuler, "AROMA 2.2 - A Monte Carlo Generator for Heavy Flavour Events in *ep* Collisions," *Comput. Phys. Commun.*, vol. 101, pp. 135–142, 1997.

[32] P. L. Frabetti *et al.*, "Charm - anti-charm asymmetries in high-energy photoproduction," *Phys. Lett.*, vol. B370, pp. 222–232, 1996.

[33] M. Iori, "Selex results on $D_s^{\pm}$, $D^{\pm}$, $D^{*\pm}$ and D^0 / $\overline{D^0}$ production," *Nucl. Phys. Proc. Suppl.*, vol. 115, pp. 103–106, 2003.

[34] M. Kaya *et al.*, "Production asymmetry of D_s from 600 GeV/c Σ^- and π^- beam," *Phys. Lett.*, vol. B558, pp. 34–40, 2003.

[35] M. Adamovich *et al.*, "Study of D^+ and D^- Feynman's x distributions in π^- nucleus interactions at the SPS," *Phys. Lett.*, vol. B305, pp. 402–406, 1993.

[36] G. A. Alves *et al.*, "Enhanced leading production of $D^{\pm}$ and $D^{*\pm}$ in 250 GeV $\pi^{\pm}$ - nucleon interactions," *Phys. Rev. Lett.*, vol. 72, pp. 812–815, 1994.

[37] E. M. Aitala *et al.*, "Asymmetries between the production of D_s^- and D_s^+ mesons from 500 Gev/c π^- nucleon interactions as functions of x_F and p_t^2," *Phys. Lett.*, vol. B411, pp. 230–236, 1997.

[38] M. I. Adamovich *et al.*, "Determination of the total $c\bar{c}$ production cross section in 340 GeV/c Σ^- nucleus interactions," *Eur. Phys. J.*, vol. C13, pp. 247–254, 2000.

[39] A. M. Halling, "Asymmetries in charm production in fixed target experiments," *Nuovo Cim.*, vol. A109, pp. 617–629, 1996.

[40] M. Arneodo *et al.*, "Measurement of the proton and the deuteron structure functions, F_2^p and F_2^d," *Phys. Lett.*, vol. B364, pp. 107–115, 1995.

List of Figures

List of Tables

Acknowledgment

My first contact with the group of Martin Faessler was *Reiner Geyer*, whom I would like to thank for giving me an opportunity to join the group.

Of course my special thanks go to my supervisor *Martin Faessler* - doing physics with him is a very enjoyable process. Numerous lunch-time discussions of physics with Martin and Reiner were very useful and always interesting through all these years. CERN is the best place in the world for a physicist working in the field of high energy physics, and for the possibility to stay and work at CERN I am very grateful to Martin and LMU.

I want to thank people of COMPASS collaboration - many results presented in the thesis would not be possible to obtain without union efforts of physicists working on hardware, software and, of course, physics.

Finally I would like to thank professor *Dorothee Schaile* and other referees for spending their time on reading my thesis. I hope the reading was not boring!